國立臺灣大學工學院土木工程學系

碩士論文

Department of Civil Engineering
College of Engineering
National Taiwan University

Master's Thesis

以多頻道表面波譜分析法建立台灣強震測站波速模型

Development of Velocity Models by MASW for Strong Ground Motion Stations in Taiwan

王顓沂

Chuan-I Wang

指導教授：郭安妮 博士

Advisor: Annie On-Lei Kwok, Ph.D.

中華民國 112 年 7 月

July, 2023

doi:10.6342/NTU202403310

摘要

剪力波速為土壤動態性質之重要參數，其於工程設計上的應用範圍甚廣，但傳統測定剪力波速的方法，例如跨孔式、下孔式或懸盪式井測法，因須鑽孔導致成本高昂，且其代表性受取樣數量限制。相形之下，多頻道表面波譜分析法（MASW）為一個相當具有潛力的替代方案；惟其可靠度仍待檢驗。

本研究經由數值模擬及現地試驗檢視該方法。數值模擬部分以多組假設地層之分析結果觀察不同情境下頻散曲線的行為。而現地試驗則透過於台灣強地動觀測網（TSMIP）中有現地調查資料的測站中實測表面波，並與以懸盪式井測法所得之結果比對。除了用於比對之測站，本研究以多頻道表面波譜分析法為六個未調查測站建立剪力波速資料。

分析結果顯示，由多頻道表面波譜分析法所得之頻散曲線穩定且可重現。而即便表面波譜法所估計之$v_{s,30}$較懸盪式井測法之估計值低，其地盤分類的結果與懸盪式井測法之結果大致相同。另一方面，於探測深度內若剪力波速有驟增之情形將造成反算之剪力波速精準度下降。而波速若有隨深度降低的情況，會依其發生深度對頻散曲線的不同頻段產生影響，造成反算時頻散曲線的有效範圍受到限制，導致反算所得之剪力波速精度下降。

關鍵字：多頻道表面波譜分析法、頻散曲線、剪力波速、台灣強地動觀測網、$v_{s,30}$

doi:10.6342/NTU202403310

ABSTRACT

Conventionally, geological surveys for the shear wave velocity, such as down-hole, cross-hole, or suspension P-S logging, etc., are expensive, labor-intensive, and must leave a lasting mark in the field. Therefore, there is always a demand for a cost-effective and non-destructive way to conduct the survey. The multichannel analysis of surface waves (MASW) solves this scenario with the developed data-processing techniques. However, concerns regarding the reliability of this method are still under discussion.

This study consists of two parts. Firstly, numerical analysis using FLAC is conducted based on hypothetical profiles and the well-investigated Lotung LSST site to observe the behavior of the dispersion curves and evaluate the applicability of MASW. Secondly, it verifies the reliability of MASW by applying the technique to sites within the Taiwan Strong Motion Instrumentation Program (TSMIP) network and comparing the results with information obtained from PS-logging. The shear wave velocity profiles are also constructed in six non-investigated sites with MASW.

The findings reveal that MASW generates stable and consistent results in experimental dispersion curves, and the uncertainty in shear wave velocity profiles mainly arises from the inversion analysis or mistaking the fundamental mode. From the perspective of site classification, the MASW performs well, although it appears to underestimate the $v_{s,30}$ compared with PS-logging. On the other hand, the potential problems that might interfere with the continuity of fundamental dispersion curves or decrease the accuracy of the shear wave velocity profile are also discussed and displayed.

Keywords: MASW, dispersion curve, shear wave velocity, TSMIP, $v_{s,30}$

doi:10.6342/NTU202403310

CONTENTS

doi:10.6342/NTU202403310

doi:10.6342/NTU202403310

doi:10.6342/NTU202403310

LIST OF FIGURES

doi:10.6342/NTU202403310

doi:10.6342/NTU202403310

doi:10.6342/NTU202403310

doi:10.6342/NTU202403310

doi:10.6342/NTU202403310

doi:10.6342/NTU202403310

doi:10.6342/NTU202403310

doi:10.6342/NTU202403310

doi:10.6342/NTU202403310

LIST OF TABLES

doi:10.6342/NTU202403310

Chapter 1 Introduction

1.1 Background

Taiwan, an island formed by a continental collision, boasts magnificent natural scenery but also faces the threat of destructive natural disasters. Earthquakes have claimed numerous lives on this island, and their occurrence remains unpredictable. However, it is sure that earthquakes will strike again. In order to minimize the impact of future earthquakes, it is crucial to take appropriate measures. Scientific understanding is the fundamental and indispensable first step in tackling these challenges.

Previous research has demonstrated that local site conditions significantly influence ground motions during earthquakes. The characteristics of ground surface motion and the behavior of response spectra are affected by the local site conditions. Notably, different types of soil profiles exhibit distinct trends in the amplification behavior of peak acceleration (Seed et al., 1976). Therefore, it is vital to investigate the shallow subsurface structure in order to comprehend motion characteristics and develop effective countermeasures.

1.2 Motivation

Conventional invasive methods used to determine dynamic soil properties suffer from drawbacks such as high costs, labor-intensive procedures, and permanent field markings. Furthermore, the representativeness of results obtained through these invasive approaches is

doi:10.6342/NTU202403310

questionable due to limitations in sample size. In contrast, the multi-channel analysis of surface waves (MASW) emerges as a promising alternative method. MASW is a seismic survey technique that enables the determination of the shear wave velocity profile of near-surface soil, providing valuable information for evaluating soil stiffness and conducting ground response analysis. This method offers advantages in terms of cost-effectiveness and efficient data collection.

Additionally, multi-channel recording allows for effectively identifying and isolating noise based on distinctive coherency patterns in arrival time and amplitude (Park et al., 1999). However, despite its advantages, the reliability of MASW results still poses challenges due to concerns regarding the uniqueness of solutions and equivalence problems associated with solving the inverse problem in surface wave tests (Foti et al., 2009). Fortunately, abundant open-source data provides an opportunity to address these concerns.

1.3 Objective

In 1991, the Taiwan Central Weather Bureau (CWB) initiated the Taiwan Strong Motion Instrumentation Program (TSMIP), which involved the establishment of over 680 free-field strong-motion stations across the nation. The primary objective of the TSMIP was to gain a comprehensive understanding of ground motion characteristics in Taiwan. As part of this project, site investigations were conducted to gather general information, including soil profiles, SPT-N values, shear wave velocities, and primary wave velocities of the strata. To date, site investigations have been completed at 483 stations.

doi:10.6342/NTU202403310

The objective of this study consists of two parts. Firstly, it aims to verify the reliability of MASW by applying this technique to the sites within the TSMIP network and comparing the results with the available information obtained from previous site investigations. This will provide an opportunity to assess the consistency and accuracy of MASW in estimating shear wave velocities and evaluating soil properties. Secondly, numerical analysis based on the hypothetical profiles and well-investigated Lotung LSST site are conducted using FLAC. By taking advantage of open-source data and conducting numerical analysis, the study seeks to further evaluate the applicability of MASW. Ultimately, MASW will be employed to explore the shear wave velocity profiles at sites within the TSMIP network that have not been previously investigated.

doi:10.6342/NTU202403310

Chapter 2 Literature Review

This chapter will go through the wave propagation theory, methods for measuring dynamic soil properties, and Taiwan's pre-existing subsurface velocity profiles. The wave propagation theory states that material stiffness is directly related to the shear wave velocity. Therefore, several techniques were developed to measure the speeds of seismic waves for exploring natural resources or geological surveys. In 1885, Lord Rayleigh predicted the existence of the surface wave and derived the equation of motion for the Rayleigh wave. The solutions to the equation revealed that the Rayleigh wave is dispersive in the layered structure. With this nature of the Rayleigh wave, the underground shear wave velocity profile could be discovered by measuring and analyzing the Rayleigh wave caused by earthquakes or other artificial seismic sources. Surface wave analysis has been developed for decades, and several techniques have been proposed to improve the accuracy of inverting shear wave velocity profiles. With advanced computational techniques, surface wave methods have become a competitive alternative for seismic surveys, and the pre-existing data can be used to examine the ability of surface wave methods.

2.1 Wave Propagation

Waves are a phenomenon of the propagation of disturbances. In the case of earthquakes or other seismic events, the waves travel through the Earth's interior as body waves or along the surface as surface waves. Body waves include P-waves and S-waves (Figure 2.1), which stand for the motion of the medium parallel or perpendicular to the direction of the wave.

doi:10.6342/NTU202403310

Surface waves, which travel along the Earth's surface, propagate slower than the body waves and could be divided into Love waves and Rayleigh waves (Figure 2.2), depending on their motion. This section will review the basic properties of seismic waves and their relation with the material properties.

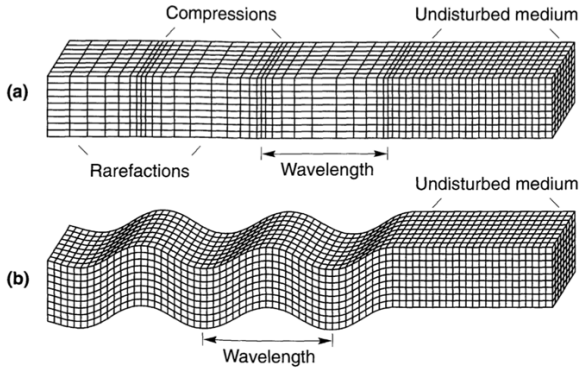

Figure 2.1 Deformation produced by body waves (a) P-wave (b) S-wave. (Bolt, 1993)

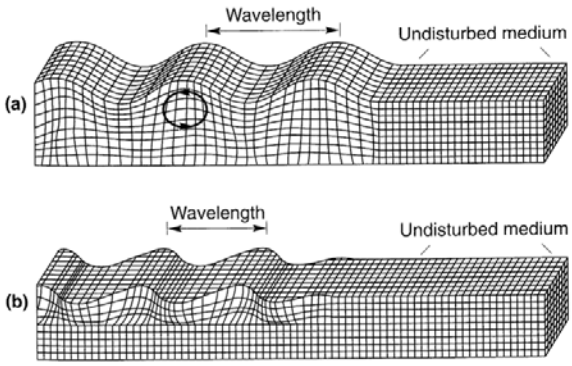

Figure 2.2 Deformation produced by surface waves (a) Rayleigh wave (b) Love wave. (Bolt, 1993)

The particle motion in a wave field could be described by the wave equation, a partial differential equation.

$$\frac{\partial^2 u}{\partial t^2} = v^2 \frac{\partial^2 u}{\partial x^2} \qquad (2\text{-}1)$$

where u is a function of time t and space x, and v is wave-propagation velocity.

doi:10.6342/NTU202403310

2.1.1 Body Waves

Considering an infinite, homogeneous, isotropic, elastic medium, two types of waves can be found to satisfy the wave equation. One is the dilatational wave derived from the normal strain of a small element (see Eq. 2-2), and the other is the distortional wave derived from the rotation of the axis (see Eq. 2-3). They are also referred to compression wave (P-wave) and shear wave (S-wave), respectively.

$$\rho \frac{\partial^2 \bar{\epsilon}}{\partial t^2} = (\lambda + 2G)\nabla^2 \bar{\epsilon} \quad (2\text{-}2)$$

$$\rho \frac{\partial^2 \omega}{\partial t^2} = G\nabla^2 \omega \quad (2\text{-}3)$$

where $\bar{\epsilon}$ is the volumetric strain, ω represents the rotation about each axis, ρ is mass density, λ is a Lamé's constant, G is the shear modulus, and ∇^2 is the Laplacian operator in Cartesian coordinate (see Eq. 2-4).

$$\nabla^2 = \frac{\partial^2}{\partial x^2} + \frac{\partial^2}{\partial y^2} + \frac{\partial^2}{\partial z^2} \quad (2\text{-}4)$$

From Eq. (2-2) and (2-3), Eq. (2-5) and (2-6) could be obtained which indicate those two wave velocities are related to the material stiffness. Eq. (2-6) also shows measuring the shear wave velocity v_s could be an effective way to estimate the shear modulus G.

$$v_p = \sqrt{\frac{\lambda+2G}{\rho}} \quad (2\text{-}5)$$

$$v_s = \sqrt{\frac{G}{\rho}} \quad (2\text{-}6)$$

where v_p is compression wave velocity and v_s is shear wave velocity.

doi:10.6342/NTU202403310

2.1.2 Rayleigh wave

In 1885, Lord Rayleigh found another type of wave satisfying the wave equation in the elastic half-space, and this kind of wave was consequently named Rayleigh wave (R-wave). It only exists near the surface of the half-space and decays rapidly with depth (Figure 2.4). Rayleigh wave is caused by the interaction of compression wave and vertical shear wave nearby the surface, and therefore, the particle within the Rayleigh wave field possesses both vertical and horizontal motion. For the wave field excited by the vertical oscillation at the surface of the half-space, the Rayleigh wave carries the most energy, about 67% of total energy, followed by the shear wave, about 26%, and the compression wave, about 7% (Kramer, 1996).

Rayleigh wave is nondispersive in an isotropic, homogeneous medium, and it travels with a constant velocity depending on material's body wave velocity and Poisson's ration (Figure 2.5). However, in an elastic medium consisting of layered structure overlying on a half-space, the Rayleigh wave becomes dispersive. The phase velocity of Rayleigh wave varies with the frequency; the high frequency (or long wavelength) components travel faster than the low frequency (or short wavelength) components.

$$\lambda(f) = \frac{v_R(f)}{f} \qquad (2\text{-}7)$$

where f is frequency, λ is wavelength and v_R is Rayleigh wave velocity as a function of frequency.

Figure 2.4 also indicates that the short wavelength components decay faster than the long wavelength components. In other words, the long wavelength components could excite the motion of the deeper layer. As a result, in the measured Rayleigh wave motion, the low

doi:10.6342/NTU202403310

frequency components carry more information about the deeper layers within the influence range, and the high frequency components represent the information about the shallow layers.

The dispersive characteristic of the Rayleigh wave field could be depicted using the dispersion curve, which displays the relation between the phase velocity and frequency (Figure 2.3). Theoretically, several phase velocities could be found for a specified frequency, composing a multi-mode dispersion curve. The dispersion curve with the lowest phase velocity is the fundamental mode dispersion curve (M_0), and the curve of first following higher phase velocity is the first mode dispersion curve (M_1) (Figure 2.3).

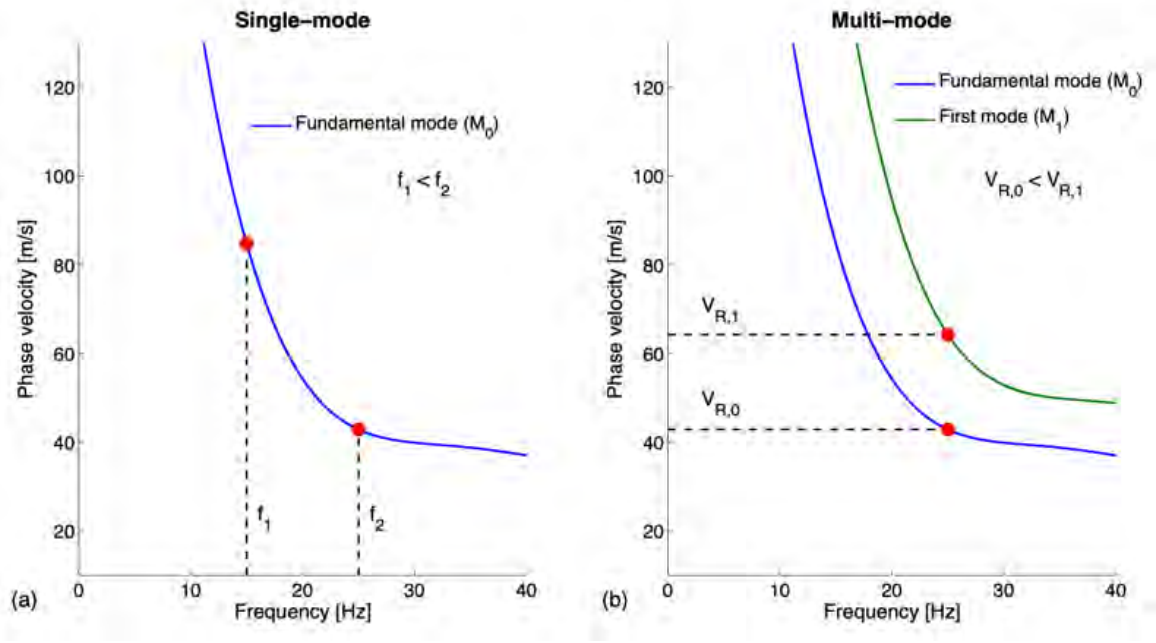

Figure 2.3 Single-mode dispersion curve and multi-mode dispersion curves. (Olafsdottir, 2014)

doi:10.6342/NTU202403310

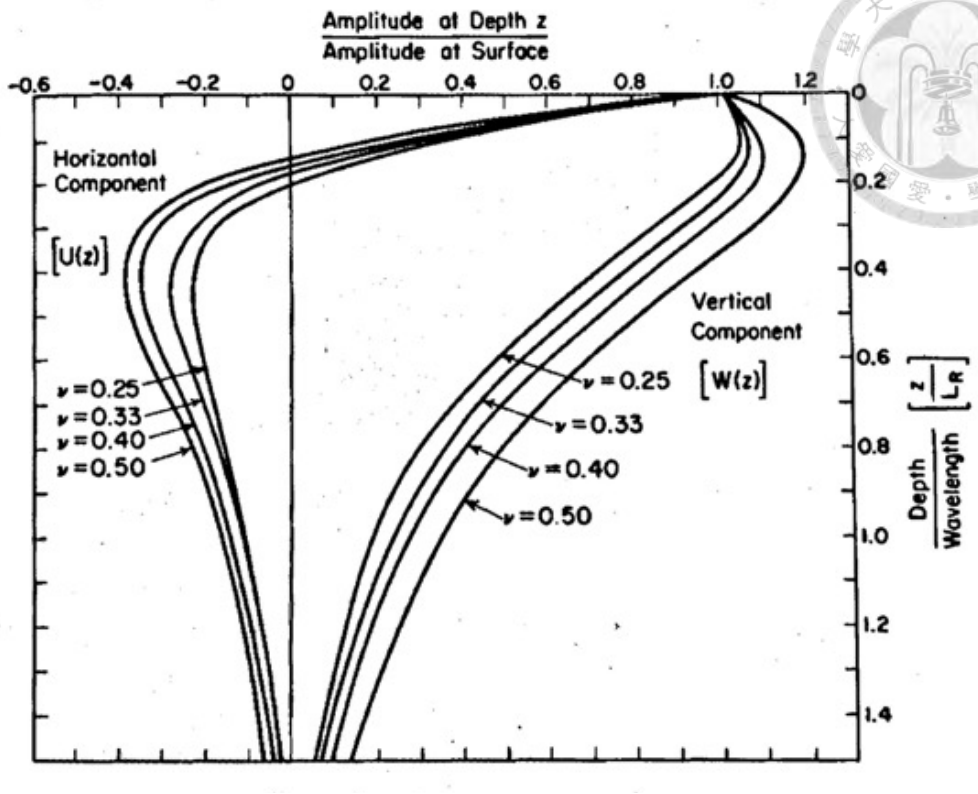

Figure 2.4 Amplitude ratio vs. dimensionless depth for Rayleigh wave. (Richart et al., 1970)

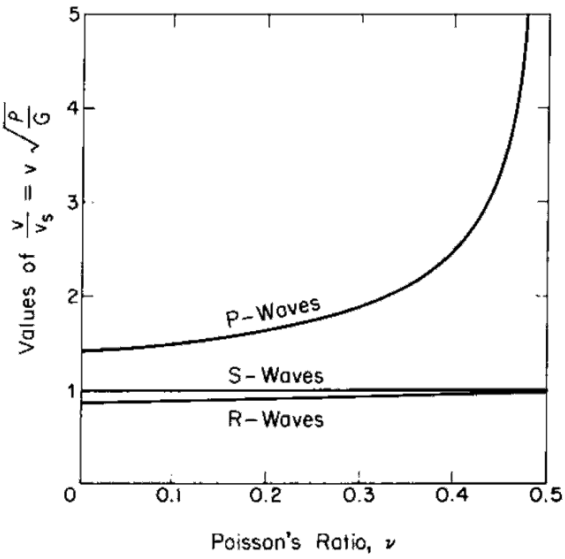

Figure 2.5 Relation between Poisson's ratio and velocity of propagation of body waves in a semi-infinite elastic medium. (Richart et al., 1970)

doi:10.6342/NTU202403310

2.2 Seismic velocity measurements

Various techniques are available for measuring dynamic soil properties, each with advantages and limitations. The five techniques described below are commonly used to measure the velocity profile in the field. The performance of each method will be summarized and compared at the end of this section.

2.2.1 Invasive methods

The invasive methods in seismic velocity measurement have been prevalent for a long time, while some were initially developed to explore natural resources. Three invasive methods, cross-hole, down-hole (up-hole) and suspension logging test are briefly described in the following paragraph.

2.2.1.1 Cross-hole test

Cross-hole measurement involves drilling two or more boreholes and placing sensors at different depths in each hole, as shown in Figure 2.6. A seismic wave is then generated in one borehole, and the sensors in the other boreholes record the arrival time of the wave. By measuring the wave's travel time between sensors, it is possible to calculate the velocity of the wave. The cross-hole method has several advantages over other geophysical techniques. It can determine velocities over small depth intervals, which makes it helpful in evaluating anisotropy. It can also measure SH- and SV-wave velocities and horizontal propagate compression waves. Additionally, it provides a good approach for determining material damping.

doi:10.6342/NTU202403310

However, there are some disadvantages to using cross-hole measurement. Two or three boreholes must be drilled, which can increase costs significantly. Accurate borehole deviation surveys must be conducted if hole depths exceed a few tens of meters. Data interpretation may also be more difficult where thinly bedded materials occur, or near layer boundaries with strong velocity contrasts (Kramer, 1996).

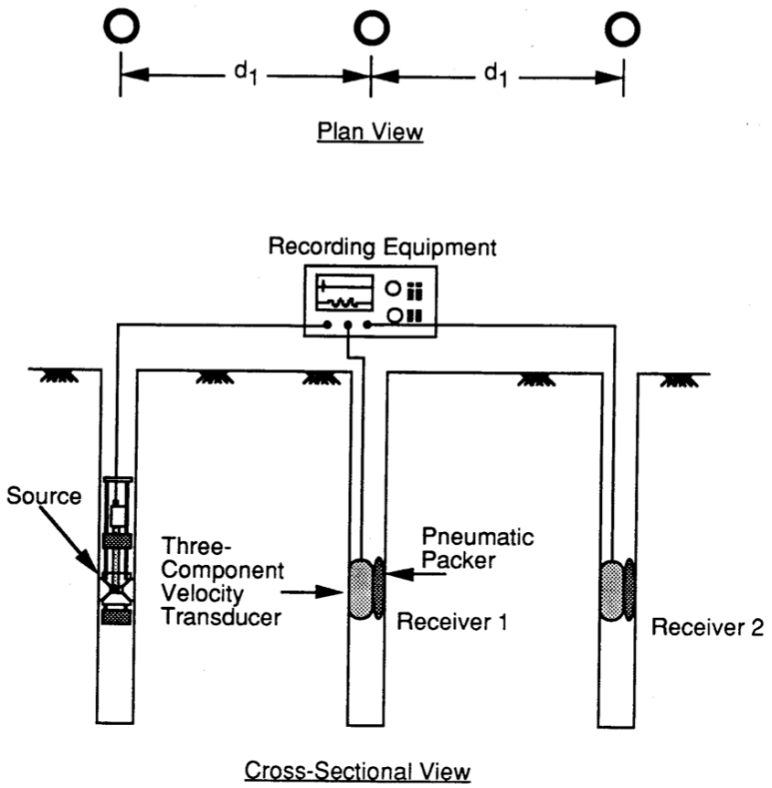

Figure 2.6 Cross-hole measurement configuration. (EPRI, 1993)

2.2.1.2 Down-hole (Up-hole) test

The down-hole (up-hole) measurement involves using an impulse energy source at the surface near the top of a cased borehole to generate waves that propagate radially. As shown in Figure. 2.7, one or more receivers are fixed at different depths in the borehole to measure

doi:10.6342/NTU202403310

the ground motion generated by the source. High-resolution digital seismographs are used to record the signals. The travel times of compression and shear waves from the source to the receivers are measured to construct travel time versus depth curves. The slope of these curves represents the wave velocity at each depth. This method provides the flexibility to generate both overall average velocity-depth profiles and detailed profiles using interval measurements.

However, there are limitations, such as signal attenuation at greater depths and difficulty in identifying velocities in low-velocity zones or thin layers, particularly with manually-applied hammer sources. Identifying P-wave velocities in soil sites with casing can also be challenging.

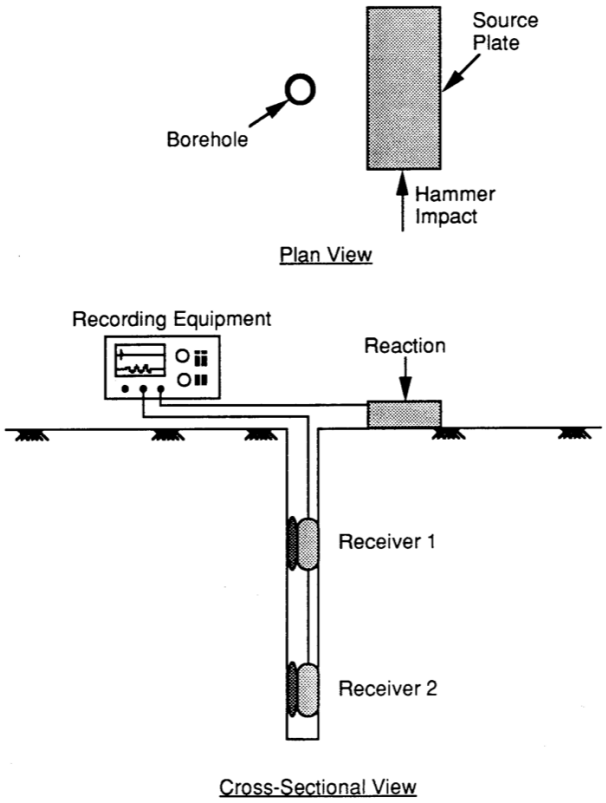

Figure 2.7 Down-hole measurement configuration. (EPRI, 1993)

doi:10.6342/NTU202403310

2.2.1.3 Suspension logging test

Suspension logging is a geotechnical method used to measure compression and shear wave velocities in an uncased borehole filled with drilling mud. As shown in Figure. 2.8, the technique involves using a horizontal solenoid as an energy source, which produces an impulsive pressure wave in the borehole fluid. Two biaxial receivers are positioned near the top of the borehole to record signals from these waves, which are then used to calculate velocities between them.

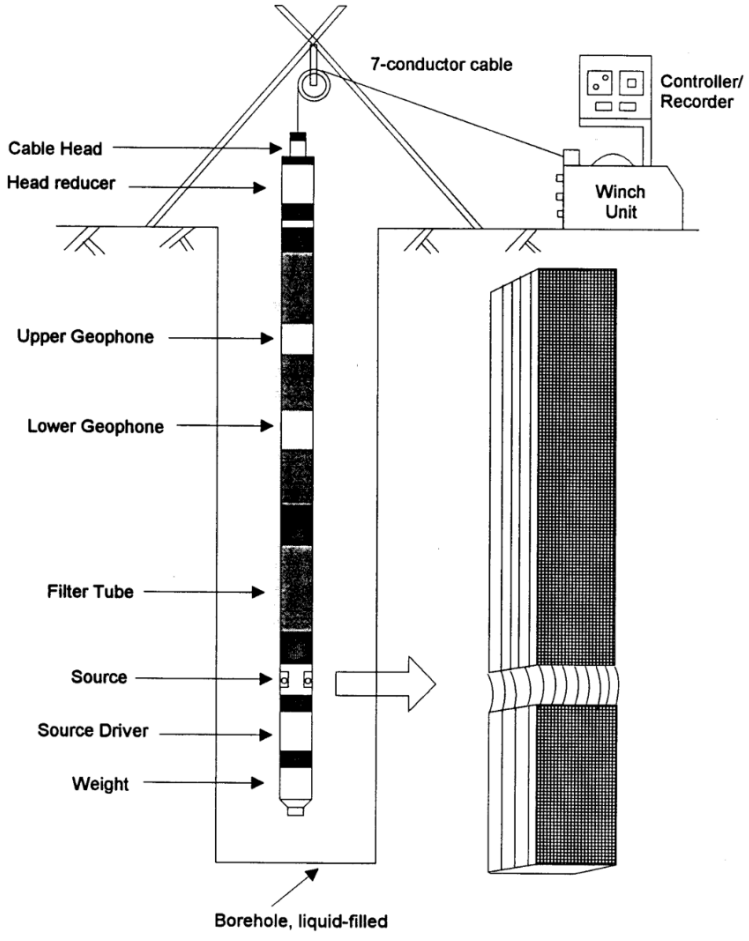

Figure 2.8 Suspension logging measurement configuration. (EPRI, 1993)

doi:10.6342/NTU202403310

The suspension logging method has several advantages, including not requiring coupling with the borehole and providing interval measurements of velocities with minimum interpretation from a single borehole. It can be used to measure both compression and shear wave velocities simultaneously, making it useful for obtaining detailed information about soil or rock properties at specific depths.

2.2.2 Surface waves methods

Generally, getting a shear wave velocity profile from surface waves analysis involves three main steps: data acquisition, dispersion analysis, and inversion analysis. The following paragraph briefly describes two methods, spectra analysis of surface waves and multi-channel analysis of surface waves. These two methods differ mainly in the data acquisition and dispersion analysis stages.

2.2.2.1 SASW

Spectra analysis of surface waves (SASW) was developed in the mid-20th century, and the concept of identifying shear wave velocity profile through the iterative matching of a theoretical dispersion curve to the experimental one was also developed in this period. SASW relies on the measurement and analysis of surface waves to obtain information on subsurface layers and their shear wave velocities (Heisey et al., 1982). The SASW test uses two receivers to record the surface waves generated by impulsive or random noise in line with the receivers (Figure 2.9).

doi:10.6342/NTU202403310

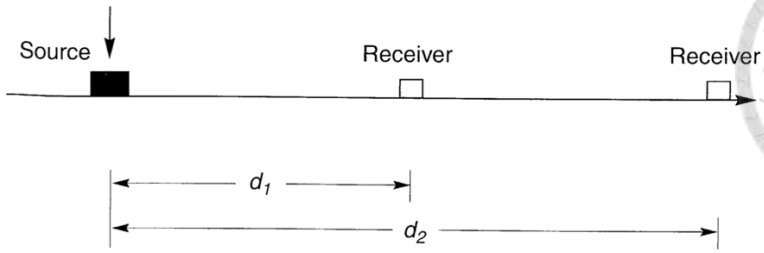

Figure 2.9 Typical configuration of source and receivers in a SASW test. (Kramer, 1996)

From Eq. 2-8, the travel time of each frequency component between the receiver pairs can be calculated by the phase difference, $\phi(f)$, obtained from the frequency domain of the two records.

$$\Delta t(f) = \frac{\phi(f)}{2\pi f} \quad (2\text{-}8)$$

With the distance between two receivers, $\Delta d = d_2 - d_1$, and the travel time of each frequency component, the Rayleigh wave phase velocity can be calculated (see Eq. 2-9) and generate the experimental dispersion curve.

$$v_R(f) = \frac{\Delta d}{\Delta t(f)} \quad (2\text{-}9)$$

Typically, the receiver spacing must be changed to detect various wavelengths within the necessary wavelength range corresponding to the desired investigation depth. After the data acquisition, several bands of dispersion curves calculated from different receiver spacing must be attached to form a single dispersion curve. Those steps lead to a certain level of complexity and require particular expertise to operate.

doi:10.6342/NTU202403310

2.2.2.2 MASW

Multi-channel analysis of surface wave (MASW) is an advanced surface wave method for exploring the dynamic properties of subsurface layers. Different from SASW, MASW adopts multi-channel to record the waveform of surface waves generated by an impulsive in line with the receiver array (Figure. 2.10). In 1999, Park et al. introduced a data process technique that could transform the waveform of surface waves recorded by a linear array of receivers into dispersion images. This development made the surface waves method more convenient since enough amount of data could be collected with just a single shot (Park et al., 1999).

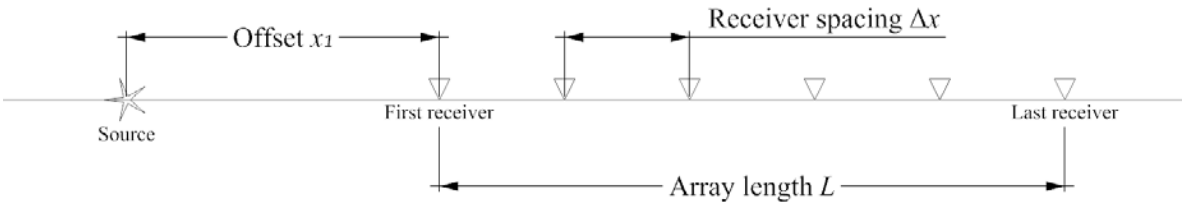

Figure 2.10 Configuration of source and receivers in a MASW test.

The multi-channel records are transformed into a 2D image with the phase shift method, and the dispersion curve can be extracted from the image. (Park et al., 1998). The phase shift method involves a frequency-domain approach of multi-channel coherency measure, which is also valid for impulsive data (Park et al., 1999). The image's resolution generated by the phase shift method is proven to be superior to that obtained from pre-existing transformation method (Park et al., 1999). With the advanced data processing algorithms, MASW is an environmentally friendly, low-cost, quick approach to measuring the shear wave velocity profiles within the first 30 m below the ground surface (Xia et al., 2002).

doi:10.6342/NTU202403310

2.2.2.3 Uncertainty in surface wave methods

The solution non-uniqueness is one great pitfall in the inversion analysis of the surface waves method. Since the shear wave velocity profile could be taken as the solution as long as its theoretical dispersion curve is close enough to the experimental one, several candidates can be generated for a single site. On the other hand, the current practice of surface wave analysis methods primarily focuses on the fundamental mode of surface waves; however, the fundamental mode may not always dominate in the propagation of surface waves.

Foti et al. (2009) applied the Monte Carlo method to the inversion analysis in the surface wave test and obtained quite different shear wave velocity profiles from the same experimental dispersion curve. However, the uncertainty became trivial when applying those velocity profiles to one-dimensional ground response analysis, which confirmed the shear wave velocity profile's effectiveness in ground response analysis (Foti et al., 2009). Regarding seismic site classification, Comina et al. (2011) also applied the Monte Carlo method to obtain a series of equivalent shear wave velocity profiles and calculate the $v_{s,30}$ of each profile. The results showed that the difference between $v_{s,30}$ evaluated by the equivalent shear wave velocity profiles is also limited (Comina et al., 2011). In addition, the $v_{s,30}$ evaluated from the surface waves method agreed with those evaluated from the invasive method in the eight test sites considered in the study.

Lin et al. (2021) inspected the behavior of the dispersion curve with four types of shear wave velocity profiles. The study indicated that when there is an embedded softer layer, the dominant mode transitions to higher modes at wavelengths beyond the depth of the soft layer.

doi:10.6342/NTU202403310

As the soft layer moves deeper, the information contained in fundamental-mode inversion decreases. It also revealed that the dispersion images and patterns of dominant higher modes vary significantly in response to different velocity profiles (Lin et al., 2021).

2.2.3 Comparison

Invasive and surface wave methods are two distinct approaches in seismic measurements to determine soil shear wave velocity. Invasive methods involve drilling boreholes to measure shear wave velocity at specific depths directly. These methods provide detailed local information about shear wave velocity distribution, including layer thicknesses, interfaces, and variations. However, they have limited spatial coverage due to the need for drilling at specific locations. Invasive methods can also cause disturbance to the soil layers during drilling, potentially affecting the accuracy of measured shear wave velocity values, particularly in loose or sensitive soils. Additionally, they tend to be more expensive and time-consuming than surface methods, requiring specialized equipment and skilled personnel.

Surface wave methods, such as MASW and SASW, offer an alternative to invasive techniques. These methods utilize surface wave data recorded at the ground level to determine the experimental dispersion curve, which relates wave propagation speed to frequency. The shear wave velocity profile can be derived by inverting the dispersion curve. Surface wave methods do not require drilling or ground probing, making them non-invasive and non-destructive. They provide broader spatial coverage, enabling the assessment of larger areas without extensive drilling. Therefore, surface wave methods are more cost-effective and efficient for larger-scale surveys and initial site assessments, as they offer

doi:10.6342/NTU202403310

broader coverage without physical disruption to the soil. However, surface methods offer averaged characteristics of the subsurface and may not provide the same level of detail as invasive methods for local variations or thin layers.

In 2022, Wang et al. selected thirteen alluvium sites in Taipei Basin and planned the simultaneous measurement of velocity profiles using the five most common seismic methods: cross-hole, down-hole, SCPT, suspension logging, and MASW. The study focused on evaluating the measurement uncertainty among the shear wave velocities obtained from different field seismic methods. They also sorted out each method's measurement principles and corresponding characteristics, which are listed in Table 2.1.

In the selected thirteen sites, the SCPT and MASW methods were found to overestimate shear wave velocity compared to the cross-hole method, which is considered more reliable. On the other hand, the suspension logging and down-hole methods showed better consistency with the cross-hole method (Wang et al., 2022).

Table 2.1 Comparison of different surveys for shear wave velocity profile. (Wang et al., 2022)

Measurement method	Cross- hole	Down- hole		Suspension P–S logging	MASW
		Boring	Seismic Cone Penetrometer		
Reliability	Good	Good	Good	Good	Good to fair
Resolution	Good; constant with depth	Good to fair; decreases with depth	Good to fair; decreases with depth	Good at depth; poor very close to the surface	Fair; decreases with depth and depends on arrangement of receivers
Preparation of holes	Boring, casing, and backfilling	Boring, casing, and backfilling	Simultaneously with CPT	Boring, casing, and backfilling	Free
Number of holes	2	1	1	1	0
Major component of particle motion	SV	SH	SH	SH	Surface waves (particularly Rayleigh waves)
Applicable Depth	Tens of meters	Tens of meters	Tens of meters	Up to 300 m	20–30 m
Strength	High reliability	Able to be a reference for V_{s30}	Short preparation time before seismic tests; able to be a reference for V_{s30}	Capable of investigating V_s in deep deposits	Capable of investigating the average V_s of deposits
Limitation	Possible refraction problems; senses stiffer material at test depth; most expensive test method	Possible refraction problems with shallow layers	Challenging for stiff deposits; possible refraction problems with shallow layers	Fluid-filled hole required; should avoid percussion drilling for preparation of holes	Complex interpretation technique; usually needs subjective judgements

doi:10.6342/NTU202403310

2.3 Available velocity profiles

The existing data on shear wave velocity in Taiwan are usually measured for studying the earthquake response or other seismic-related topics. The large-scale seismic tests in Lotung and Hualien thoroughly investigated the seismic properties of test sites, and Taiwan Strong Motion Instrumentation Program provides general information, including the shear wave velocity of the station sites around Taiwan (Figure. 2.11).

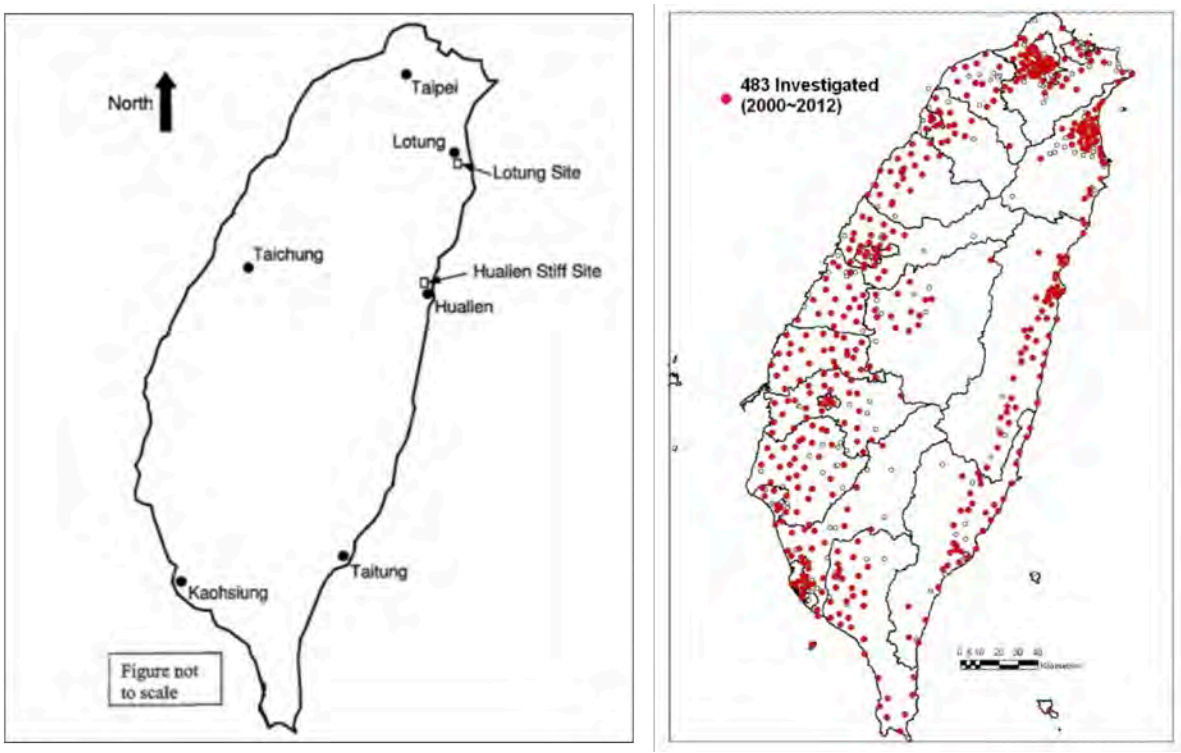

Figure 2.11 Location of Hualien and Lotung large-scale testing sites, left. (Tang et al., 1991) The investigated sites distribution from 2000 to 2012, right. (NCREE, 2009)

2.3.1 Large-scale seismic test sites

The Large-Scale Seismic Tests (LSST) in Lotung and Hualien were launched by the Electric Power Research Institute (EPRI), the Taiwan Power Company and other institutes. The test

doi:10.6342/NTU202403310

aimed to collect data on forced vibration and earthquake response to evaluate seismic soil-structure interaction (SSI) methods. The earthquake database from these tests is used to validate seismic analysis methods and modeling techniques.

Lotung LSST

Several geotechnical exploration programs were conducted at the Lotung site, including four drilling and sampling programs and one cone penetration testing program. Two seismic surveys were also carried out, including an up-hole and cross-hole program and a shear wave refraction program.

The drilling and sampling programs revealed that the site's upper 100 to 120 feet consist of interbedded silty sand and sandy silt, with occasional gravel deposits encountered at depths of 60 to 70 feet. Below this upper layer is a thick, finer-grained soil ranging from silty clay to clayey silt, extending to depths exceeding 1000 feet. The bedrock is located at depths greater than 1300 feet (EPRI, 1993).

Cross-hole tests were carried out with travel distances between the seismic source and receiver holes ranging from 30 ft to almost 70 ft. The maximum depth achieved during the cross-hole testing was approximately 200 ft. Up-hole tests were conducted to depths reaching 500 ft. The seismic testing program used PVC casing to line the boreholes (EPRI, 1993). Figure 2.12 displays the measured shear and compression wave velocities from cross-hole tests.

doi:10.6342/NTU202403310

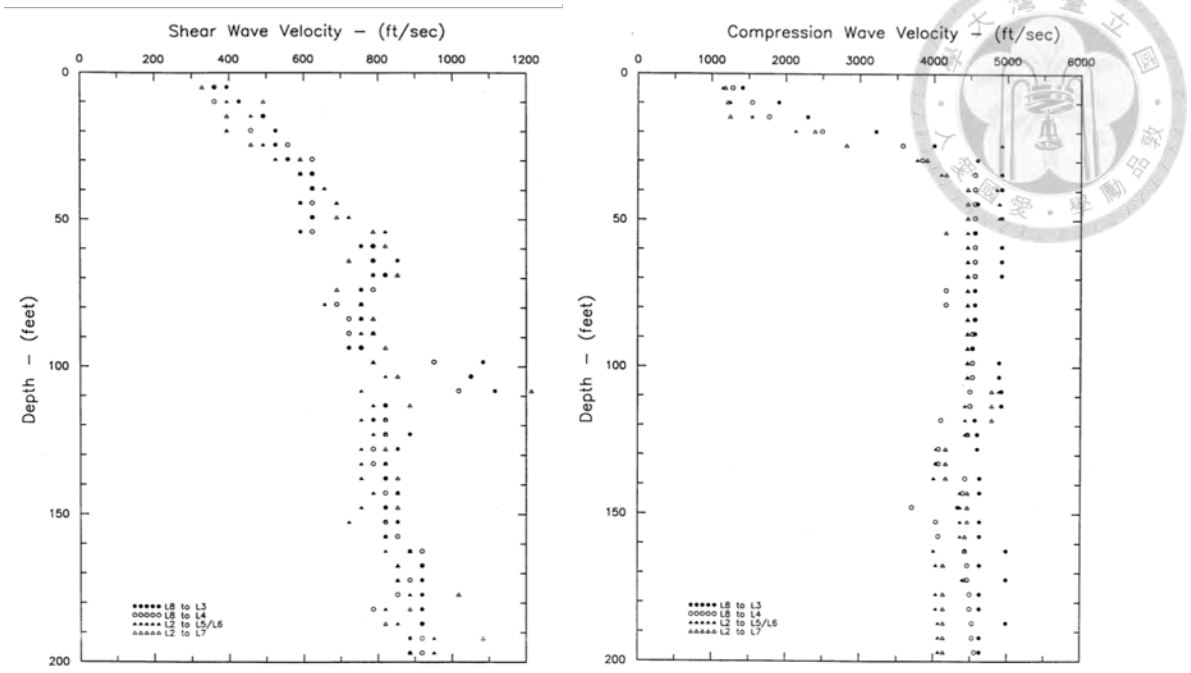

Figure 2.12 Shear and compression wave velocities at Lotung LSST. (EPRI, 1993)

Hualien LSST

The Large-Scale Seismic Tests (LSST) in Hualien aimed to obtain seismic soil-structure interaction data for stiff soil site conditions that may resemble those encountered at nuclear power plant sites (Tang et al., 1990).

The site's soils include a backfill material from 0 to 0.85 m depth, silty sand with little gravel from 0.85 m to about 5.40 m depth, and gravel with medium to coarse-grained sand from about 5.40 to about 50.0 m. The top 5 m below ground level consists of loose to medium silty sand, and the layer below consists of dense to very dense gravelly soils with gravel-size particles ranging from 3 cm to 7 cm (Miller et al., 2001).

Seismic surveys in Hualien LSST, including up-hole and cross-hole and shear wave

doi:10.6342/NTU202403310

refraction tests, were conducted in different project phases. Figure 2.13 displays the velocity profiles measured before excavation, in which the shear wave velocities were measured by cross-hole and down-hole tests, and down-hole tests measured the compression wave velocities.

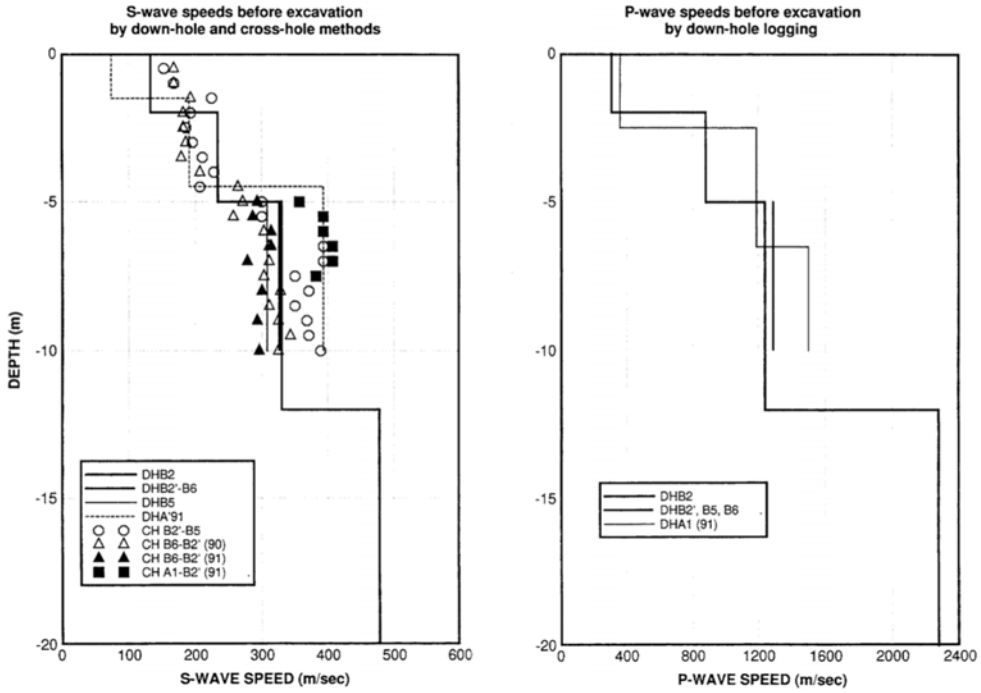

Figure 2.13 Shear and compression wave velocities before excavation at Hualien LSST. (Miller et al., 2001)

2.3.2 Taiwan Strong Motion Instrumentation Program sites

In 1991, the Taiwan Strong Motion Instrumentation Program (TSMIP) was launched by the Central Weather Bureau (CWB) to monitor ground movements at more than 680 free-field stations across Taiwan. Later in 2000, Central Weather Bureau (CWB) and National Center for Research on Earthquake Engineering (NCREE) established a project to collect and disseminate subsurface data from seismograph station sites. The results of these

doi:10.6342/NTU202403310

investigations, including general information, soil profiles, SPT-N values, shear wave velocities, and primary wave velocities of the strata, have been compiled and made available on the EGDT website, enabling access to crucial data for research and engineering purposes (NCREE, 2009). An example of subsurface data from seismograph station sites is displayed in Figure 2.14.

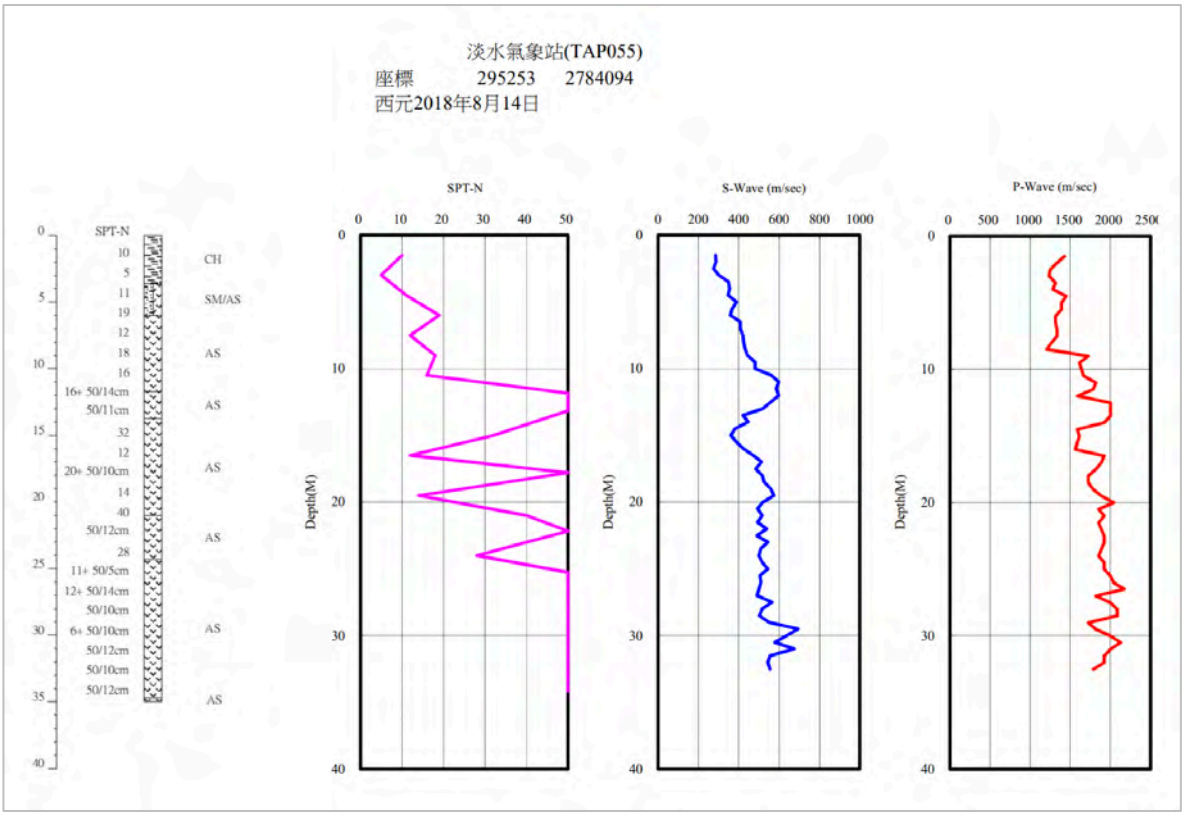

Figure 2.14 An example of subsurface data from seismograph station sites. (NCREE, 2009)

doi:10.6342/NTU202403310

Chapter 3 Methodology

This study includes numerical analysis and field tests, and this chapter will go through the technical details of those two parts and the data process methods. The same approach to generating 1D shear wave velocity profiles is applied to data from numerical analysis and field tests.

3.1 Numerical analysis

FLAC, Fast Lagrangian Analysis of Continua, is used in this study to conduct the numerical analysis. This numerical analysis consists of two stages: initializing with gravity and loading dynamic forces. In the first stage, the testing profiles' material properties, such as bulk modulus, shear modulus, and density, will be set and calculate the initial stress state. In the second stage, a time history of impact force will be applied on the top surface of the model, and a series of monitoring points will record the waveform generated by the impact force to simulate the MASW test in the field.

3.1.1 Boundary condition

Four types of boundary conditions are used in the numerical analysis: free surface, fixed boundary, quiet boundary and free-field boundary. The fixed boundary is used in stage one to reach the gravitational equilibrium, and the absorbing boundaries are used in stage two to minimize the influence of reflected waves.

doi:10.6342/NTU202403310

The fixed boundary restricts the velocity change in the x- or y-direction (Itasca, 2011). By applying the fixed boundary in the beginning, the displacement change can also be prevented. In the first stage, the grid points on the left and right sides of the model are fixed in the x-direction to crate the lateral pressure and reach a uniform horizontally layered stress state within the model. The grid points at the bottom are fixed in both the x- and y-direction to balance the gravitational forces and reach a static stress state.

The quiet boundary, also known as the absorbing boundary, is a technique used in numerical analysis to minimize wave reflections at the boundaries. It aims to simulate an unbounded medium surrounding the region of interest. The quiet boundary employs the concept of viscous dashpots attached independently to the boundary in the normal and shear directions. These dashpots generate viscous tractions (see Eq. 3-1 and 3-2) that absorb energy from approaching waves, effectively reducing wave reflections. Its implementation helps to achieve more accurate and reliable analyses by preventing the reflection of outward propagating waves and allowing for the necessary energy radiation (Itasca, 2011).

$$t_n = -\rho C_p v_n \quad (3\text{-}1)$$

$$t_s = -\rho C_s v_s \quad (3\text{-}2)$$

where v_n and v_s are the normal and shear components of the velocity at the boundary, ρ is the mass density, C_p and C_s are the compression and shear wave velocities.

The free-field boundary aims to enforce the conditions of the extended medium in the absence of a structure. It simulates free-field motion and ensures that outward waves

doi:10.6342/NTU202403310

originating from the structure are properly absorbed. To apply the free-field boundary, a one-dimensional "column" of unit width is created, representing the behavior of the extended medium (Figure 3.1). It is discretized into elements corresponding to the zones along the lateral boundaries of the main grid. The displacement field is assumed to have a linear variation within each element. Besides the attached columns, the free-field boundary is implemented by performing a one-dimensional free-field calculation parallel to the main-grid analysis. The behavior of the free field is computed separately but simultaneously with the analysis of the main grid (Itasca, 2011).

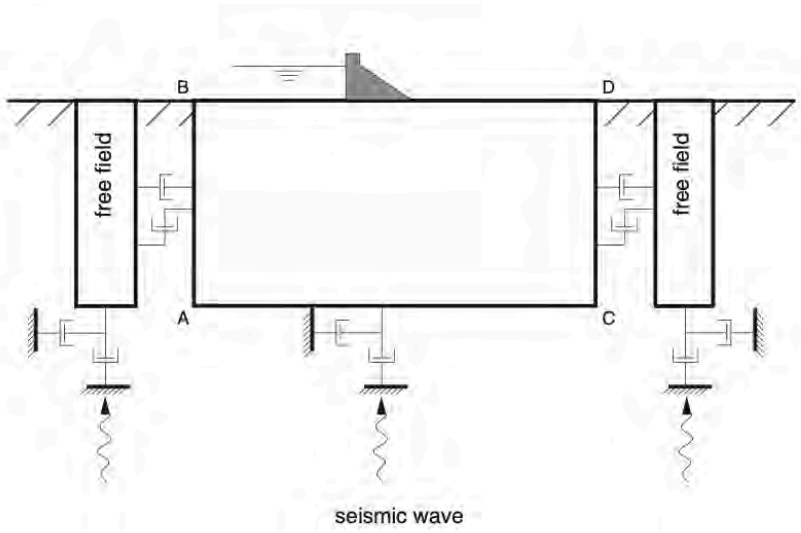

Figure 3.1 Configuration of free-field boundary. (Itasca, 2011)

Although applying the quiet boundary on the lateral sides and at the bottom is adequate to the requirements in this numerical analysis, the free-field boundary is applied to the lateral boundaries in the second stage to pursue a more realistic circumstance.

doi:10.6342/NTU202403310

3.1.2 Model geometry

The model geometry depends on the requirement of stage two. The first requirement is to be large enough to accommodate the scale of the test field and the influenced range of surface waves. The second requirement is to minimize the influence of reflected waves from the boundary. Therefore, the ultimate size of the model may heavily depend on the boundary conditions.

Generally, building the model as large as possible in the dynamic analysis will always be better to minimize the waves reflected back into the model. If a model is large enough, the energy of the waves will be absorbed by the material damping. However, a large model can lead to time-consuming and inefficient problems in the computational aspect. Using absorbing boundaries is one alternative for saving the burden in computing; still, there is an issue that requires attention. According to Lysmer and Kuhlemeyer (1969), the viscous boundary, placing dashpots at the boundary of the model in both normal and shear directions, absorbs body waves approaching boundary perfectly when the incident angle is greater than 30°. The incident angle in their research was defined as the angle between the surface and propagating wave direction (Figure 3.2). Figure 3.3 displays the energy ratio incident waves to reflected waves in compression and shear wave, and indicates the absorbing boundary performs well with both compression and shear wave in a certain range of incident angle.

doi:10.6342/NTU202403310

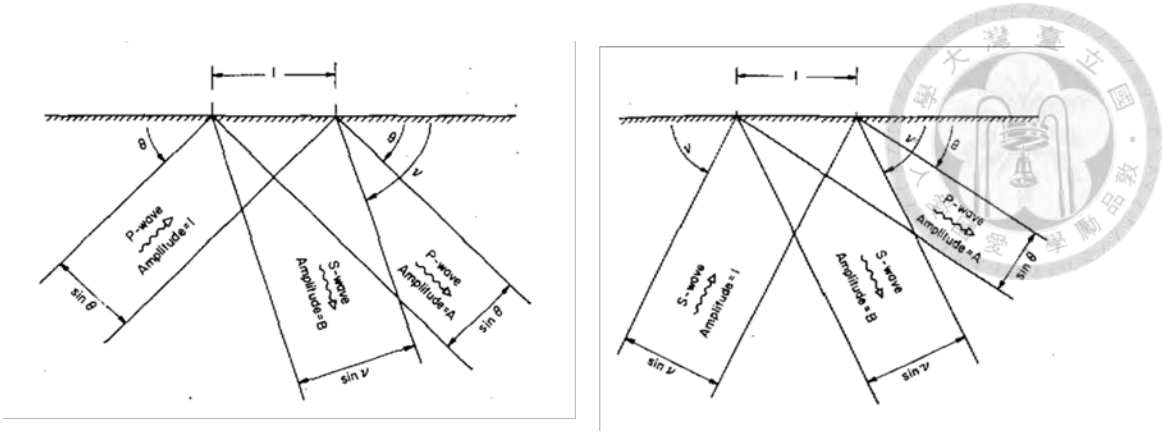

Figure 3.2 Incident P-wave (left) and S-wave (right). (Lysmer & Kuhlemeyer, 1969)

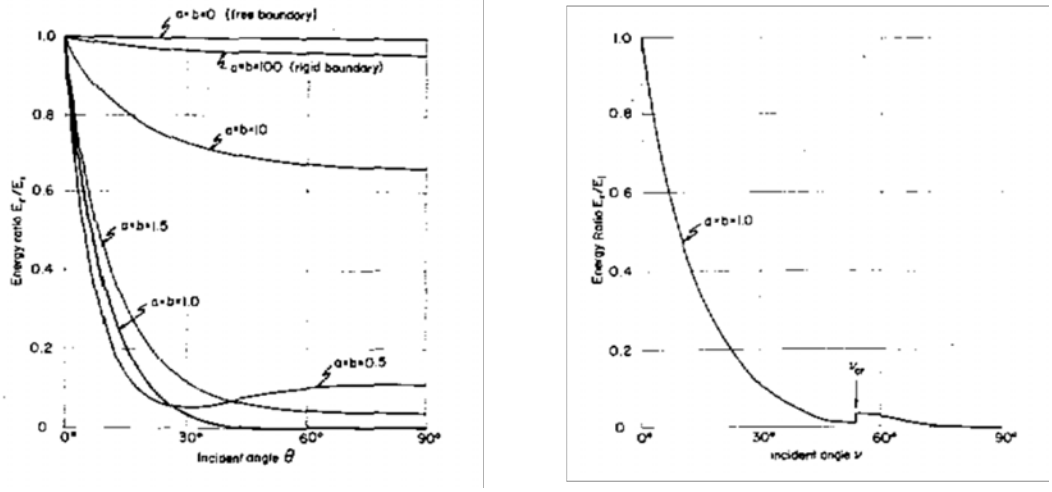

Figure 3.3 Energy ratio for incident P-wave (left) and S-wave (right). (Lysmer & Kuhlemeyer, 1969)

Regarding to the performance of the absorbing boundary described in the previous paragraph, if the depth of the model is decided, the minimum length that can make sure the absorbing boundary will perform well can be calculated. As shown in Figure 3.4, the length of the model can be divided into two sides by the source, and the receiver array can be placed on either side. The side with the receiver array should be at least $2htan60°$ long, and the other should be at least $htan30°$ long. As long as the length of the model is greater than this minimum length, the influence of the reflected waves can be trivial.

doi:10.6342/NTU202403310

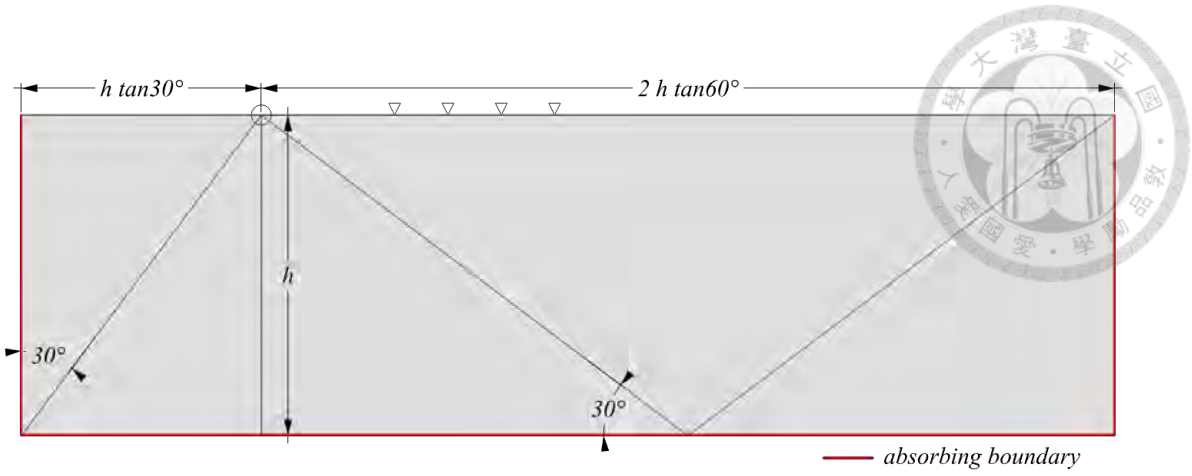

Figure 3.4 The minimum length of the model for a given depth h.

The size of models used in the following numerical analysis will stick to the minimum size shown in Figure 3.4. In addition to the absorbing boundary and model geometry, the material damping can further diminish the influence of the reflected waves. The effectiveness of this setting can also be confirmed by the recorded waveform displayed in Chapter 4.

3.1.3 Grid size

In order to ensure an accurate depiction of wave transmission through a model, Kuhlemeyer and Lysmer (1973) suggested that the spatial element size, Δl, should be finer than roughly one-tenth to one-eighth of the wavelength, λ, corresponding to the highest frequency component of the input wave (see Eq. 3-3).

$$\Delta l \leq \frac{\lambda}{10} \qquad (3\text{-}3)$$

Figure 3.5 displays the accurate range for the dispersion curve concerning the spatial element size. The area above the lines is the area with reliable information. Therefore, the grid size depends on the desired frequency band and the material properties of the shallow layers. In

doi:10.6342/NTU202403310

the cases that the shallow layers are very soft, a fine grid size should be considered to preserve the information carried by high-frequency components.

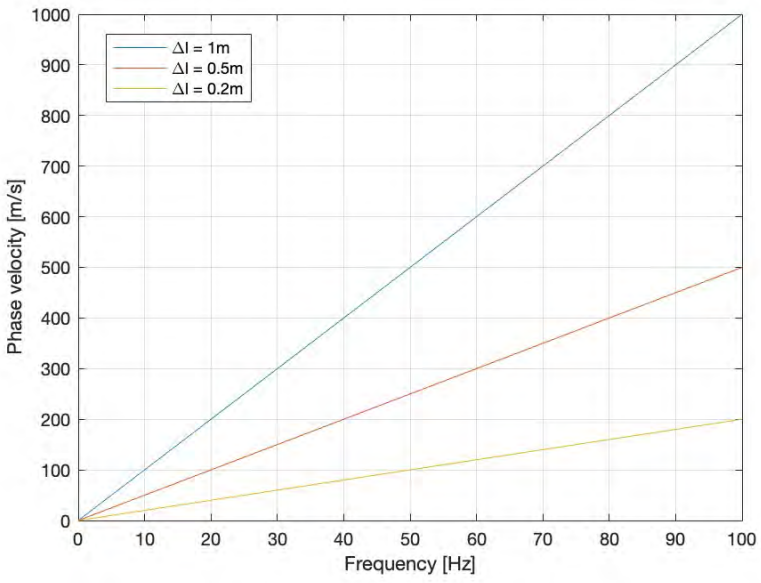

Figure 3.5 The Accurate range of frequency depends on different grid sizes and phase velocities.

3.1.4 Input motion

Three types of input motions (Figure 3.6) were considered in the beginning: a rectangular impulse force history, a triangular impulse force history, and a real record from the field test as a velocity history of the grid point. The differences were tested by applying those three types of input motions to the same model and comparing the dispersion curves. The model is 30 meters deep with four layers: 5m ($v_s = 300m/s$), 5m ($v_s = 350m/s$), 5m ($v_s = 400m/s$), and 15m ($v_s = 450m/s$). Each layer has a Poisson's ratio of 0.33 and a density of 1850 kg/m³.

doi:10.6342/NTU202403310

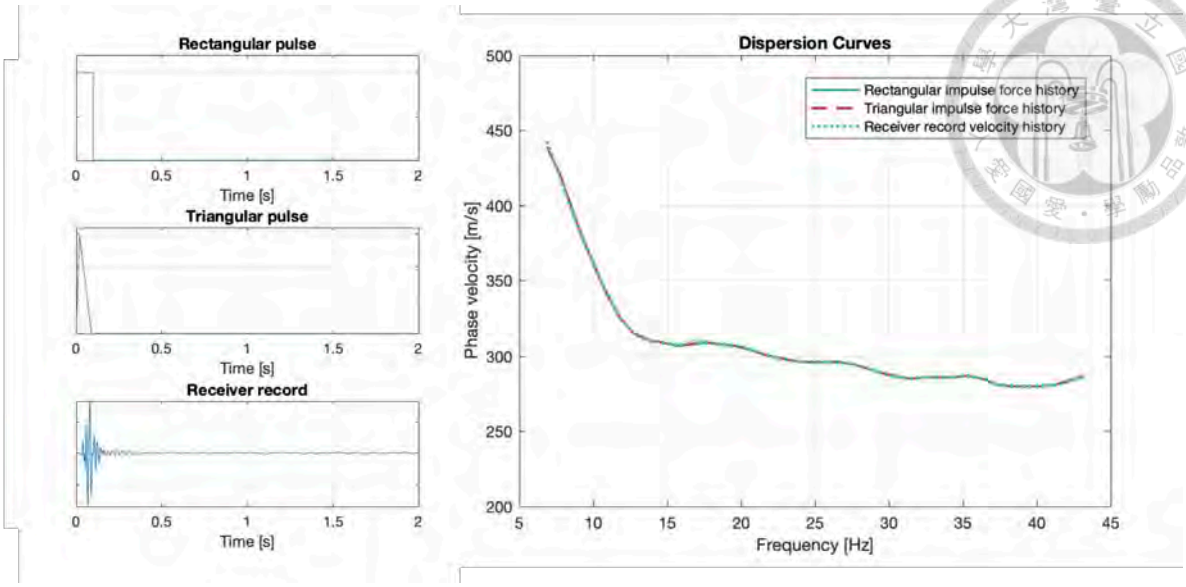

Figure 3.6 comparison of the dispersion curves calculated form three different input motions.

As shown in figure 3.6, the dispersion curves extracted from each case are almost identical. This result is not surprising since each type of input motions can provide the frequency band covering the desired frequency band. For the consistency, the rectangular impulse force history will be adopted in the numerical analysis. To validate the use of rectangular impulse force history as input motion, a comparison was made between the frequency spectrum of actually recorded signals and monitoring signals in FLAC. The data from the MASW test conducted at Lotung LSST was utilized. The frequency spectrum of records obtained from receivers 15 meters away from the source was compared with the spectrum from a monitoring point 14 meters away from the source in the numerical model. In Figure 3.7, the comparison between the frequency spectra is depicted. The peak frequency of the signal in FLAC is slightly lower than that of the actual signals, but the overall trend shows agreement between them two. This suggests that using rectangular impulse force history can yield reasonable results in the numerical analysis.

doi:10.6342/NTU202403310

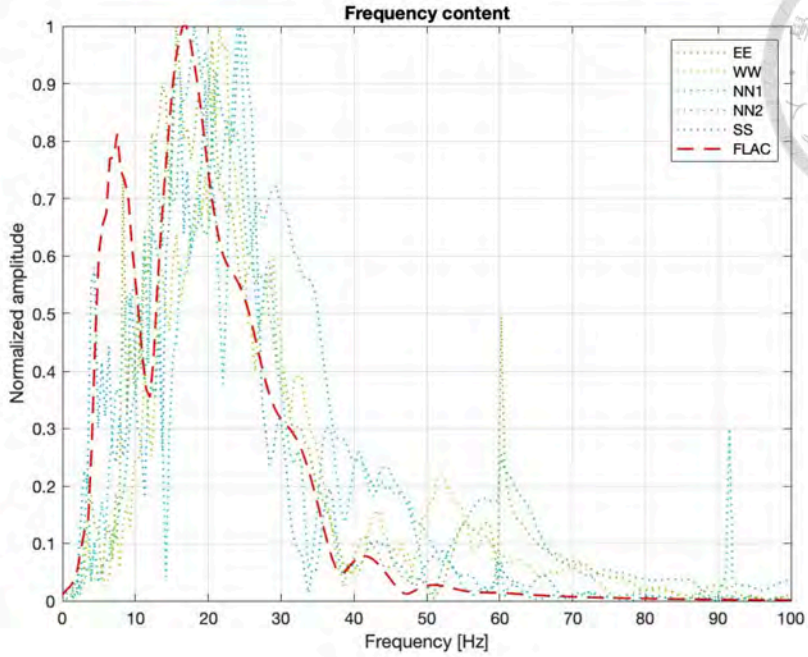

Figure 3.7 Comparison of frequency content between actual signals and signals in FLAC

doi:10.6342/NTU202403310

3.2 Field test

The equipment used in the field test comprises a seismic source, receivers, and a seismograph. Figure 3.8 displays the connection of all hardware components. Three types of surveys are conducted in the field test with the equipment: 1D MASW data acquisition, microtremor survey, and 2D MASW data acquisition. In the following sections, general information on the hardware components will be given, and the processes of each type of survey will be narrated.

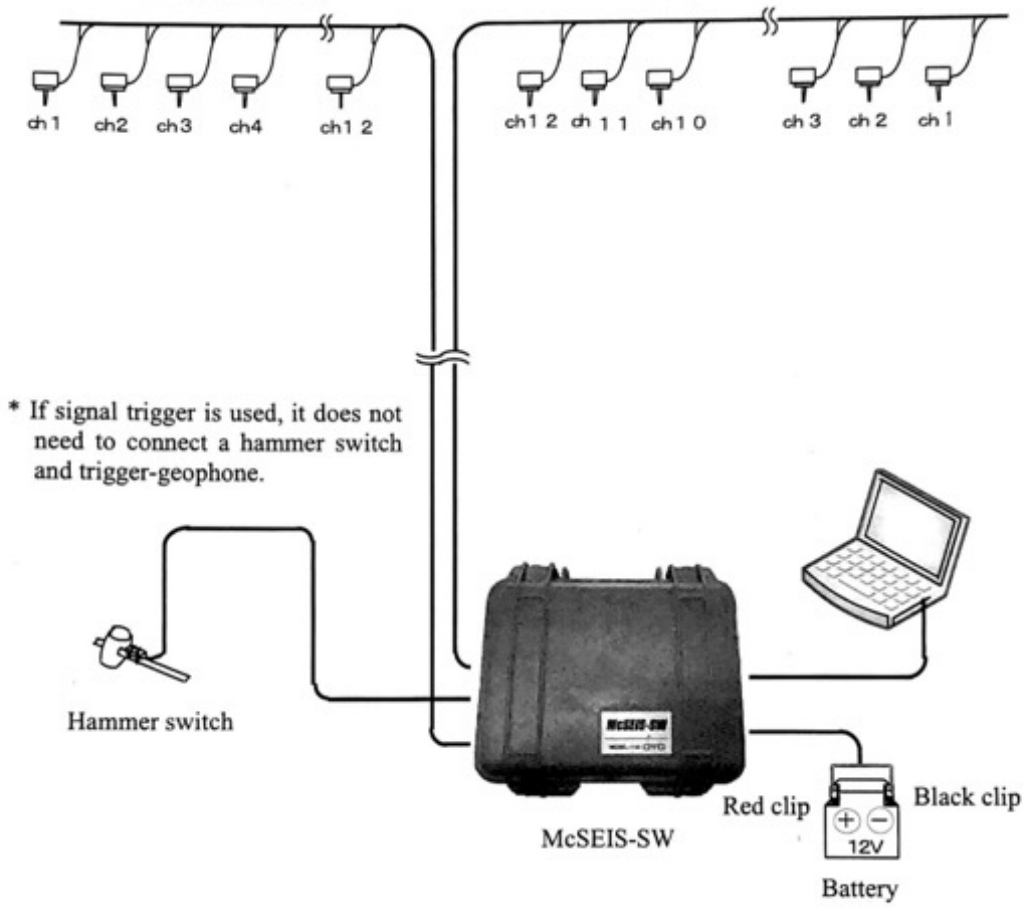

Figure 3.8 Connection of hardware components. (OYO, 2016)

doi:10.6342/NTU202403310

3.2.1 Seismograph

The seismograph, McSEIS-SW (MODEL-1109), used in this study is produced by OYO corporation. It is a specialized 24-channel seismic survey instrument designed for surface wave and seismic refraction surveys (OYO, 2016). Controlling the device and performing measurement and analysis for the surface wave method is facilitated through the accompanying software in the connected PC. Figure 3.9 shows the appearance of the device, and Table 3.1 gives the specification of McSEIS-SW.

Table 3.1 Specification of McSEIS-SW (MODEL-1109). (OYO, 2016)

Numbers of channels	24ch (fixed)
Frequency band	1.75Hz to 8KHz
Dynamic range	144 dB
Sampling rates	0.0625, 0.125, 0.25, 0.5, 1.0, and 2.0 msec
Data length	1024, 2048, 4096, 8192, and 16384 words
Data format	SEG2

Figure 3.9 Appearance of McSEIS-SW (MODEL-1109). (OYO, 2016)

doi:10.6342/NTU202403310

3.2.2 Source and receivers

To generate the active seismic source, a 12-pound sledgehammer is dropped freely from approximately 3 m onto a rectangular steel plate about 5 cm thick. It is worth mentioning that the sledgehammers have limited energy in the lower frequency range, typically below 8 to 10 Hz. Consequently, this limitation restricts the effective investigation depth to approximately 30 meters, and the effective investigation depth in soft sites may be further limited to around 15 to 20 meters (Foti et al., 2018).

The array of receivers senses the vibration and transforms it into an electric current, and the signals are processed in McSEIS-SW and stored in the PC as a SEG2 file. The receivers used in the field tests have a cutoff frequency of 4.5Hz vertical receiver. Generally, it is adequate for investigation depth within 30 meters (Foti et al., 2018).

doi:10.6342/NTU202403310

3.2.3 Data acquisitions

The same layout of receivers is adopted in the field test for the 1D and 2D MASW data acquisition and microtremor survey. The receiver array is 46 m long with 2 m receiver spacing. This configuration is compatible with most TSMIP sites, and it is also the most versatile and practical choice.

3.2.3.1 1D gather

Three fundamental parameters should be determined for setting up a 1D data acquisition layout: source offset, x_1, receiver spacing, Δx, and the array length, L, (Figure 2.10). Foti et al. (2018) indicated that there is an appropriate range for each parameter, which is listed in Table 3.2.

Table 3.2 Suggested parameters for MASW surveys. (Foti et al., 2018)

Parameter	Notation	Suggested value
Offset	x_1	5-20m
Receiver spacing	Δx	1-4m
Array length	L	23-96m

The source offset, x_1, is the distance between the seismic source and the first receiver in the array. Due to the near-field and far-field effects, a range of 5 to 20 meters for the offset is suggested. The near-field effect describes that the Rayleigh wave cannot be taken as a plane wave within a certain distance from the source (Richart et al., 1970). In other words, some undesirable signals may interfere with the data since the offset is not long enough. On the other hand, the far-field effect narrated the high frequency (short wavelength) components

doi:10.6342/NTU202403310

of the surface waves attenuate at speed with increasing distance from the source (Bullen et al., 1985). Overall, reducing the undesirable signals in the first receiver and conserving enough high frequency components in the last receiver are two main concerns for the offset. Also, separating the near- and far-offset traces for phase-velocity calculations allows a more comprehensive data analysis; this approach considers both near-offset and far-offset effects, resulting in a more reliable and realistic dispersion curve (Park et al., 1999).

It is common to use receivers that are spaced at a constant interval in active gather. For a given number of receivers, increasing the spacing between receivers can result in reduced resolution for shallow depths, while extending the array length can enhance the investigation depth at the cost of lower resolution. Regarding those issues, a range of 1 to 4 meters of the receiver spacing and a range of 23 to 96 meters for the array length are suggested (Foti et al., 2018).

During field tests, a 10m offset 1D data gathering is conducted in sites performing a 10m offset shot is feasible. Alternatively, the 1D data can be extracted from the first and last shots of the 2D data. In this case, the first two receivers closest to the source are removed, resulting in a survey line with 22 receivers and a 5m offset. This approach allows for collecting 1D data using either a dedicated 10m offset setup or extracting it from the 2D data, providing data acquisition and analysis flexibility.

doi:10.6342/NTU202403310

3.2.3.2 2D gather

The 1D MASW method focuses on obtaining a vertical shear wave velocity profile, representing the average shear wave velocity corresponding to the depth along the survey line. In the 2D MASW method, multiple shots are taken at incrementing locations along the linear spread of receivers (Figure 3.10). These shots capture a broader coverage of the subsurface. The recorded data from each shot are then processed with the common mid-point cross-correlation (Geometrics, 2006; Hayashi & Suzuki, 2004).

Figure 3.10 2D MASW acquisition receiver spread configuration.

The common mid-point cross-correlation involves calculating the midpoint between the source and each geophone in a shot record. The traces that have the same mid-point are gathered together, forming the CMP gather. This gathering represents the response of the subsurface at that particular mid-point. By cross-correlating the traces within the CMP gather and stacking them, the signal-to-noise ratio and the lateral resolution can be improved. This process helps to mitigate noise and improve the accuracy of the resulting cross-sectional image of shear wave velocity (Hayashi & Suzuki, 2004).

doi:10.6342/NTU202403310

3.2.3.3 Microtremor surveying

The passive source survey, or microtremor survey method (MSM), is adopted in this study to provide the low-frequency band of the dispersion curve and extend the investigation depth. Acquiring extensive long-wavelength data holds significant importance in enhancing investigation depth and accuracy (Rix, 1995). During a passive source survey, the seismograph captures vibrations caused by various sources such as cultural noise, traffic, factories, wind, and wave motion. Unlike active surveys, there is no specific timing device to trigger the seismograph in passive surveys.

The ideal vibration sources are steady and constant for accurate analysis using the spatial autocorrelation (SPAC) method (Aki, 1957). The method assumes that the signal wavefront is planar, stable, and isotropic, meaning it comes from all directions and is independent of source locations (Okada & Suto, 2003).

Twenty records with a recording of 32 seconds are gathered in every field test to minimize the influence of intermittent noise (such as nearby passing cars). Longer records contribute to smoother frequency domain conversion, while multiple records provide a statistically robust representation of the noise (Geometrics, 2006).

doi:10.6342/NTU202403310

3.3 Surface wave analysis

The 1D data collected from numerical analysis and field tests will go through the same process, calculating the experimental dispersion curves and inverting the shear wave velocity profile. In the dispersion analysis of MASW, the records will be transformed into a 2D image where the dispersion curve can be extracted. On the flip side, a theoretical dispersion curve is calculated based on an assumed profile, and the solution is determined by matching the theoretical dispersion curve to the experimental one. This iterative process of comparing and adjusting the theoretical and experimental curves is a general approach in surface wave analysis.

3.3.1 Dispersion analysis

Dispersion is a phenomenon in which waves of different frequencies travel at varying speeds through a medium. The dispersion analysis of surface wave aims for revealing the relationship between the frequency and phase velocity of the wave. In this research, an open-source MATLAB code, MASWaves (Olafsdottir et al., 2018), was modified to process the multi-channel surface wave records of active test using the phase shift method.

The phase shift method was first developed by Park et al. (1998). It is a wave field transformation method for depicting the dispersion image in the MASW. This method can provide better-quality dispersion images than the previous method and require a relatively small number of traces (Park et al., 1998).

doi:10.6342/NTU202403310

The general process of the phase-shift method involves testing a series of given sets of frequency and phase velocity to find the most probable dispersion curve. To start with, for isolating each frequency component, the multi-channel records $u(x,t)$ are transformed from time domain into the frequency domain by applying the Fourier transform. As the actual waveform data is discrete, the fast Fourier transform (FFT) is adopted to perform the discrete Fourier transform.

$$U(x,\omega) = \int u(x,t)e^{i\omega t}dt \qquad (3\text{-}4)$$

where x is the distance between the seismic source and the receiver, t is time, and ω is angular frequency.

The $P(x,\omega)$ can be further separate into the multiplication of phase and amplitude spectrum, denoted by $P(x,\omega)$ and $A(x,\omega)$, respectively. In this expression, the dispersion properties are solely carried by the phase spectrum $P(x,\omega)$, in which the information regarding the arrival time of each frequency component is preserved. The amplitude spectrum $A(x,\omega)$, on the other hand, carries the information relating to the energy dissipation.

$$U(x,\omega) = P(x,\omega)A(x,\omega) \qquad (3\text{-}5)$$

Since the phase and the amplitude are separated and the amplitude term is real and positive, the phase term $P(x,\omega)$ could be considered a normalized $A(x,\omega)$. For simplicity, the phase term will be expressed using the exponential form:

$$P(x,\omega) = \frac{U(x,\omega)}{|U(x,\omega)|} = e^{-i\Phi(\omega)\mathrm{x}} \qquad (3\text{-}6)$$

where $\Phi(\omega) = \omega/\mathrm{c}_\omega$, ω is angular frequency, and c_ω is phase velocity corresponding to ω.

doi:10.6342/NTU202403310

The actual phase velocity c for frequency ω is contained in the term Φ(ω); however, it is impossible to determine because several candidates could satisfy this equation. As a result, the traveling distance x is utilized to find the most probable one. By giving testing phase velocity and frequency, a series of testing phase shifts corresponding to the traveling distance could be calculated. Those testing phase shifts are used to compensate for the time delay for the specific traveling distance in the wave field. Applying those testing phase shifts to the phase term in Eq. 3-6, the integration over traveling distance will reach a maximum value if the testing phase velocity equals the actual phase velocity. In other words, the actual phase velocity could be determined by finding at which phase velocity the function $A(x, \omega)$, integration over traveling distance, would reach a peak value (Park et al., 1998).

$$A(\phi, \omega) = \int e^{-i(\Phi - \phi)x} dx \qquad (3\text{-}7)$$

where $\phi = \omega / c$, c is an assumed phase velocity.

In the field test, the surface wave generated by an active seismic source is recorded by a linear array of receivers. The integration, therefore, becomes a discrete summing of a finite number of receivers, and the summation is normalized with respect to the receiver number N to eliminate the influence on peak value.

$$A(x, \omega) = \frac{1}{N} \sum_{j=1}^{N} e^{-i(\Phi - \phi)x_j} \qquad (3\text{-}8)$$

By plotting the amplitude at the corresponding location of frequency and phase velocity, the dispersion curve can be extracted from the peak of the image (Figure 3.11). Generally, the sharpness of the peak increases with the number of receiver N, and therefore, the resolution of the image can be improved by using more trace (Park et al., 1998).

doi:10.6342/NTU202403310

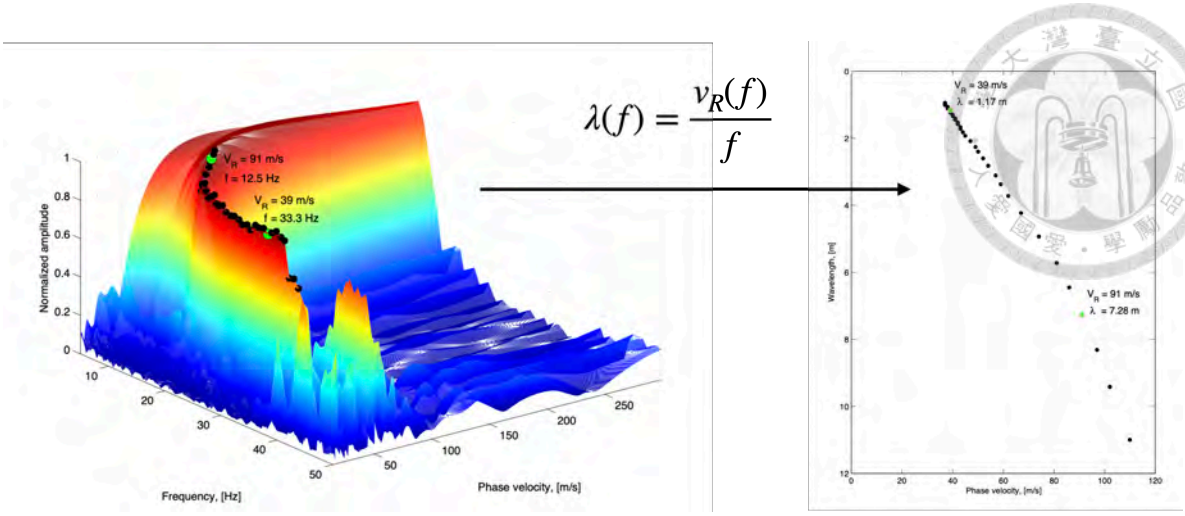

Figure 3.11 Extract dispersion curve. (Olafsdottir et al., 2018)

The dispersion curve obtained from the active test can further combine with the curve generated from passive test (Figure 3.12). By merging the passive and active data sets, a broader frequency range can be examined, allowing for a more comprehensive understanding of subsurface properties. Additionally, combining the images helps to determine the dispersion trends of the fundamental mode (Park et al., 2007).

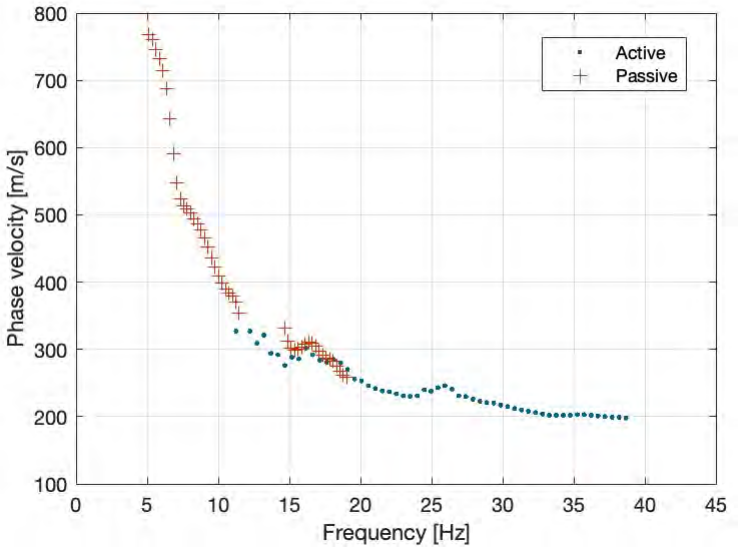

Figure 3.12 Combination of active and passive data.

doi:10.6342/NTU202403310

After the dynamic analysis, the records will be drawn out of FLAC to calculate the dispersion curve. The dispersion curve will be calculated and extracted by MATLAB functions MASWaves_dispersion_imaging and MASWaves_extract_dispersion_curve in MASWaves.

3.3.2 Inversion analysis

The dispersion curves sourcing from the field cannot calculate the shear wave velocity directly because their relationship is complex. It requires inverse analysis to obtain the most probable shear wave velocity profile. This algorithm starts by assuming a shear wave velocity profile and then calculating its theoretical dispersion curve. If the theoretical dispersion curve is close enough to the experimental one, the assumed shear wave velocity profile will be considered an adequate solution.

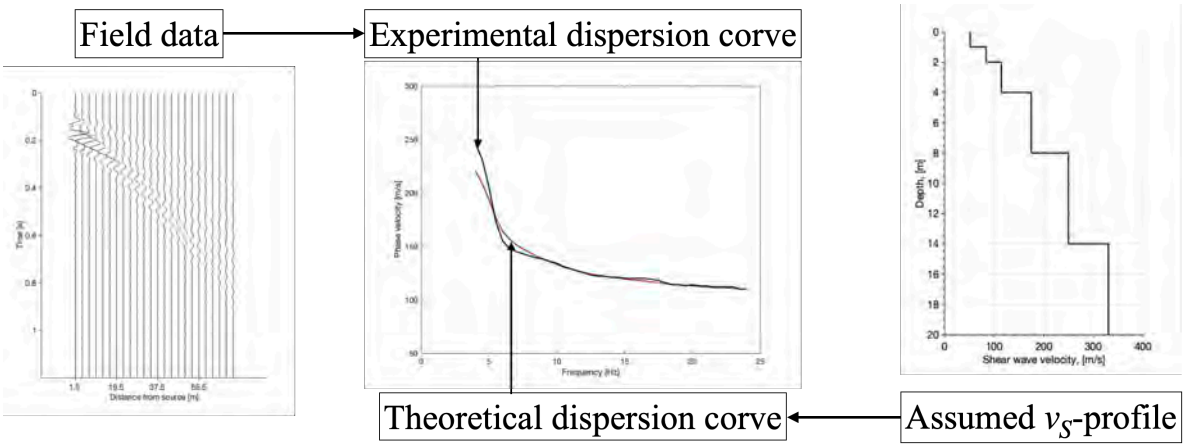

Figure 3.13 Illustration of inversion analysis.

Several methods have been developed for solving the boundary value problem of waves traveling through the soil layers overlying the half-space, and the solution to the free surface could further determine the dispersion curve. The matrix method is widely adopted to obtain

doi:10.6342/NTU202403310

the theoretical dispersion curve; it was initially introduced by Thomson (1950) and corrected by Haskell (1953) (Beaty et al., 2002). After that, numerous approaches were proposed for improving numerical stability, the ability to handle high frequencies, and also calculating speed and accuracy. The versions proposed by Menke (1979) and Kausel and Roësset (1981) will be mentioned in chapter 4.2, illustrating that the fundamental mode and first two higher mode dispersion curves generated by those two approaches are almost identical in the desired range (Figure 4.4).

Menke's approach is a refined version of the method proposed by Abo-Zena (1979). In Menke's approach, Abo-Zena's method was reformulated to achieve faster computational speed (Menke, 1979). This method could identify the dispersion function from a vector, which has been propagated to the surface with a propagator matrix (Menke, 1979). Then, the roots of the dispersion function are the Rayleigh wave dispersion curves.

The stiffness matrix method proposed by Kausel and Roësset (1981) is another popular way to calculate the Rayleigh wave dispersion curves. This approach is also an improved version of Thomson's (1950) algorithm with more efficient for numerical implementation (Kausel & Roësset, 1981). In this approach, the layer stiffness matrix will first be constructed (see Eq. 3-9) using six parameters which are shear wave velocity, compression wave velocity, thickness of the layer, mass density, wave number, and Rayleigh wave phase velocity. And then, assemble the layer stiffness matrix into the system stiffness matrix (see Eq. 3-10). The natural modes of Rayleigh wave dispersion curve could be found when there is no external load (see Eq. 3-11).

doi:10.6342/NTU202403310

$$P_j = K_j U_j \quad j = 1, \ldots, (n+1) \tag{3-9}$$

$$P = KU \tag{3-10}$$

$$D(c,k) = \det(K) = 0 \tag{3-11}$$

where K_j is stiffness matrix of the layer, K is system stiffness matrix, P is external load vector, U is displacement vector, n is the number of layers, c is Rayleigh wave phase velocity, and k is wave number.

Several approaches can be utilized to quantify the difference between the experimental and theoretical dispersion curves. In this study, the mean absolute percentage error and root mean square error were used (see Eq. 3-12, 3-13). Mean absolute percentage deviation (MAPD) measures the average percentage difference between points on experimental and theoretical curves, providing a relative measure of error:

$$\varepsilon = \frac{1}{N}\sum_{i=1}^{N} \frac{\sqrt{(c_{e,i}-c_{t,i})^2}}{c_{e,i}} \times 100\% \tag{3-12}$$

Root mean square deviation (RMSD) calculates the square root of the average of the squared differences between points on experimental and theoretical values, providing a measure of the deviation:

$$RMS = \sqrt{\frac{\sum_{i=1}^{n}(c_{e,i}-c_{t,i})^2}{n}} \tag{3-13}$$

In addition to the iterative approach, a simplified inversion method (SIM) was proposed by Pelekis and Athanasopoulos (2012). This approach converts the dispersion curve directly into the shear wave velocity profile, and it generally involves three steps, depth conversion,

doi:10.6342/NTU202403310

layering, and shear wave velocity conversion. In the first step, the wavelength values in the dispersion curve are converted to equivalent depths, D, with a depth conversion factor, α_z (see Eq. 3-14). The choice of αz depends on factors such as Poisson's ratio, ν, and ranges from 0.3 to 0.85.

$$D = \alpha_z \lambda_R \quad (3\text{-}14)$$

After the depth conversion, the apparent phase velocity, v_R, versus depth, D, curve is approximated using a best fit multilinear curve, and the phase velocity for each layer is calculated using Eq. 3-15.

$$v_{R,n} = \frac{\bar{v}_{R,n} D_n - \bar{v}_{R,n-1} D_{n-1}}{D_n - D_{n-1}} \quad (3\text{-}15)$$

Lastly, the phase velocity can be further converted into the shear wave velocity with the relation shown in Eq. 3-16, where ν is Poisson's ratio. The shear wave velocity profile obtained from this approach is taken as the initial profile in the inversion analysis in this research.

$$v_s = \frac{1+\nu}{0.87+1.12\nu} v_R \quad (3\text{-}16)$$

doi:10.6342/NTU202403310

Chapter 4 Numerical analysis

The numerical analysis in this study aims to simulate the active test of MASW and confirm that the waveform recorded by the receiver can generate a reasonable dispersion curve or display the potential problem of this approach. This chapter will go through the parameters used in the numerical model, details in each stage of the simulation, a verification of the model response, and the simulation results. The model's response will first be verified by comparing the result of one-dimensional site response analysis using DEEPSOIL 7.0 and FLAC, and a profile mentioned in other research will be used to confirm the result in simulating the active MASW test. In addition, a comparison among the theoretical dispersion curves derived from Menke's (1979) version of the matrix propagator method and the stiffness matrix method from Kausel and Roësset (1981) will be displayed. After the verification, the numerical analysis will test the hypothetical profiles and profiles from the Lotung LSST site.

doi:10.6342/NTU202403310

4.1 Model configuration

The numerical analysis consists of two stages: stress state initialization and applying dynamic loading. All units in this numerical analysis will follow the international system of units (SI). In the first stage, model parameters and material properties will be set to initialize the stress state with static analysis. In order to achieve the uniform stress state in layered soil, the fixed boundary condition in the x-direction is set on the left and right sides of the model, and the fixed boundary condition in both x- and y-direction is set at the bottom of the model. Gravity is assumed $10\ m/s^2$ in this study. Figure 4.1 displays the initialized normal stress in the y-direction.

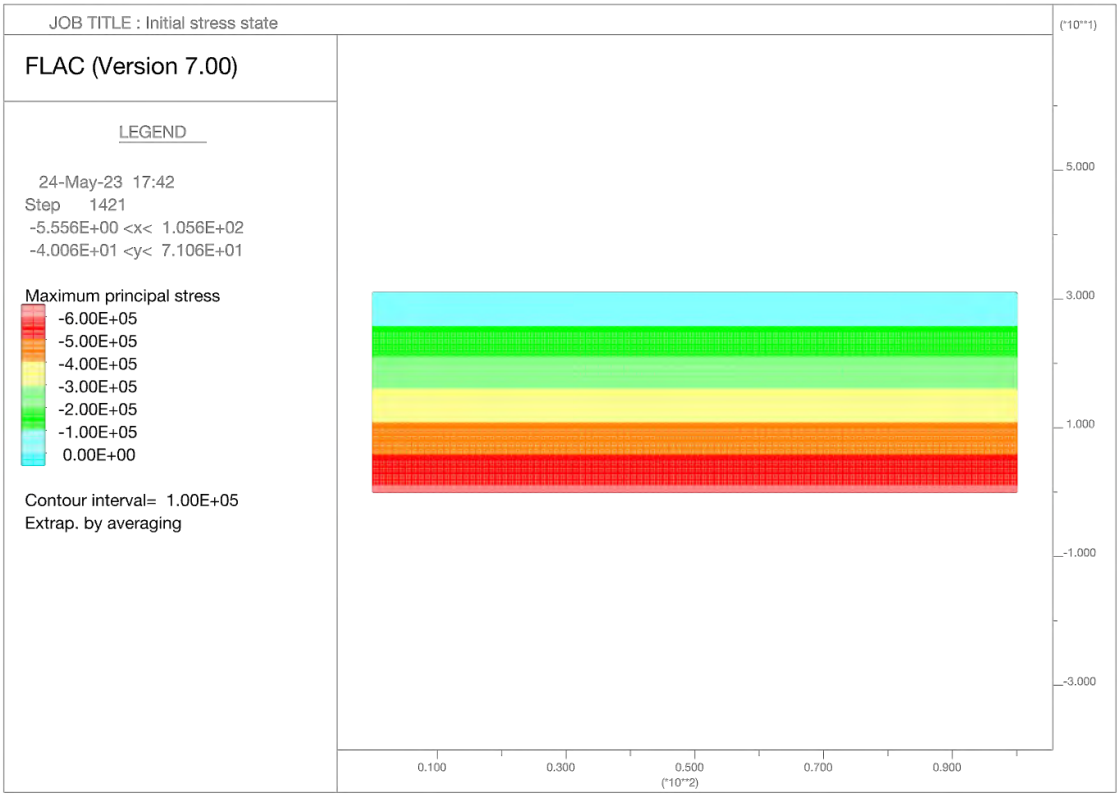

Figure 4.1 The initial stress state of the normal stress in y-direction.

doi:10.6342/NTU202403310

In the second stage, the displacement and velocity will be initialized to zero, and the absorbing boundaries will replace the fixed boundaries. The free field boundary will replace the fixed boundaries on the left and right sides, and the quiet boundary will replace the fixed boundary at the bottom. An impulse force history will be applied at the top surface and 10 meters away from the first monitoring point. During the dynamic analysis, the propagation of seismic waves will be recorded by the monitoring points as velocity history.

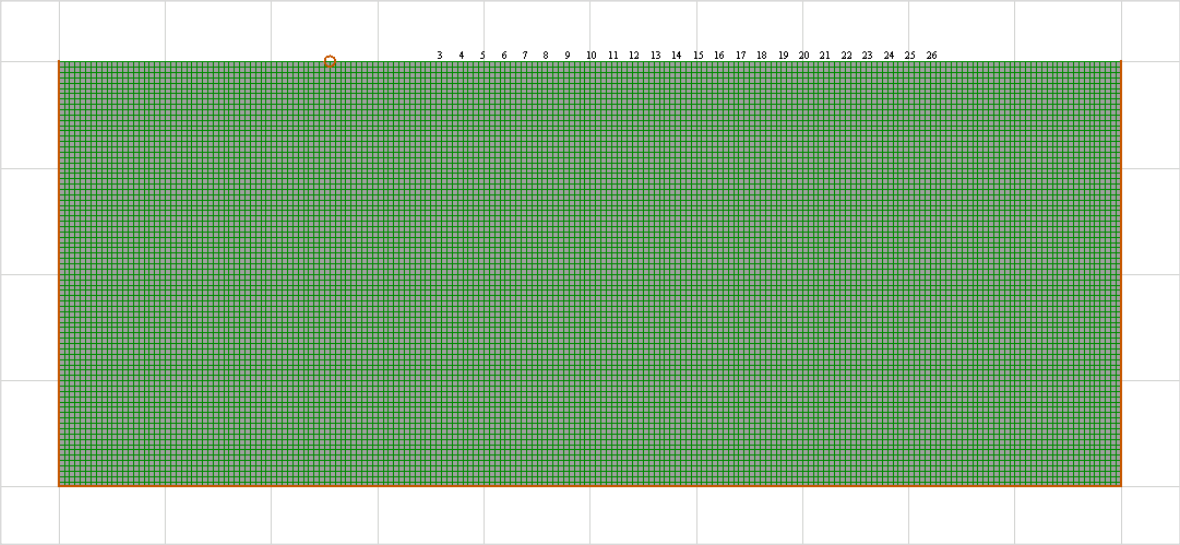

Figure 4.2 The location of source and receivers and boundary condition in stage two.

4.2 Model verification

In order to ensure that the parameter settings and model response in FLAC are accurate, a one-dimensional ground response analysis is conducted and compared with results obtained from DEEPSOIL. Input motion is applied at the bottom of the model in two different ways to demonstrate the behavior of the model in rigid and compliant base conditions.

doi:10.6342/NTU202403310

For the rigid base case, the model simulates how motion on the bedrock propagates into the soil layers. In FLAC, the rigid base condition is achieved by applying only an acceleration history of the Chi-Chi earthquake at the bottom of the mesh. That causes the downward propagating wave to reflect into the model, resulting in amplification as it travels through softer soil layers. To replicate this condition in DEEPSOIL, the rigid half-space option is selected. The details of the settings used in FLAC and DEEPSOIL are listed in Table 4.1.

Table 4.1 Rigid base settings.

FLAC	DEEPSOIL
– Rigid base – Free-field boundary – Depth $50m$ – Grid $1m \times 1m$	– Rigid half-space – Depth $50m$ – 1m thickness for each layer
– Density = $1850\ kg/m^3$ – Shear-wave velocity = $300\ m/s$ – Poisson's ratio = 0.33	– Unit weight = $18.14\ kN/m^3$ – Shear-wave velocity = $300\ m/s$ – Damping ratio = 5%
– Elastic model – Rayleigh damping: $\xi_{min} = 0.037, \omega_{min} = 3.354$	– Linear-time domain – Rayleigh damping: $f_1 = 1.5Hz, f_2 = 7.5Hz$

In the compliant base case, the input motion simulates the actual particle motion of the upward propagating wave. In FLAC, a quiet boundary and stress history of the Chi-Chi earthquake is applied at the bottom of the mesh to achieve the compliant base condition. The stress history is obtained by converting the velocity history using the Eq. 4-1. To replicate this condition in DEEPSOIL, the elastic half-space option is specified, and the bedrock properties are set to match the last layer to ensure that half of the input energy propagates downward.

$$\sigma_s = \rho C_s v_s \qquad (4\text{-}1)$$

Since the same motion (acceleration history) is used in FLAC and DEEPSOIL, the factor of two is removed from the velocity-stress translating formula mentioned in the FLAC manual

doi:10.6342/NTU202403310

for comparison purposes. The settings used in FLAC and DEEPSOIL are listed below for each case.

Table 4.2 Compliant base settings.

FLAC	DEEPSOIL
– Compliant base – Free-field boundary – Depth $50m$ – Grid $1m \times 1m$	– Elastic half-space – Depth $50m$ – 1m thickness for each layer
– Density = $1850\ kg/m^3$ – Shear-wave velocity = $300\ m/s$ – Poisson's ratio = 0.33	– Unit weight = $18.14\ kN/m^3$ – Shear-wave velocity = $300\ m/s$ – Damping ratio = 5%
– Elastic model – Rayleigh damping: $\xi_{min} = 0.037, \omega_{min} = 3.354$	– Linear-time domain – Rayleigh damping: $f_1 = 1.5Hz, f_2 = 7.5Hz$

Figure 4.3 displays the results of the ground response analysis. The response spectra of the ground motion obtained from DEEPSOIL and FLAC are visually identical in both cases, but upon closer inspection, the two lines in the same case have slight differences. The results illustrate the preliminary verification of the material properties and other settings.

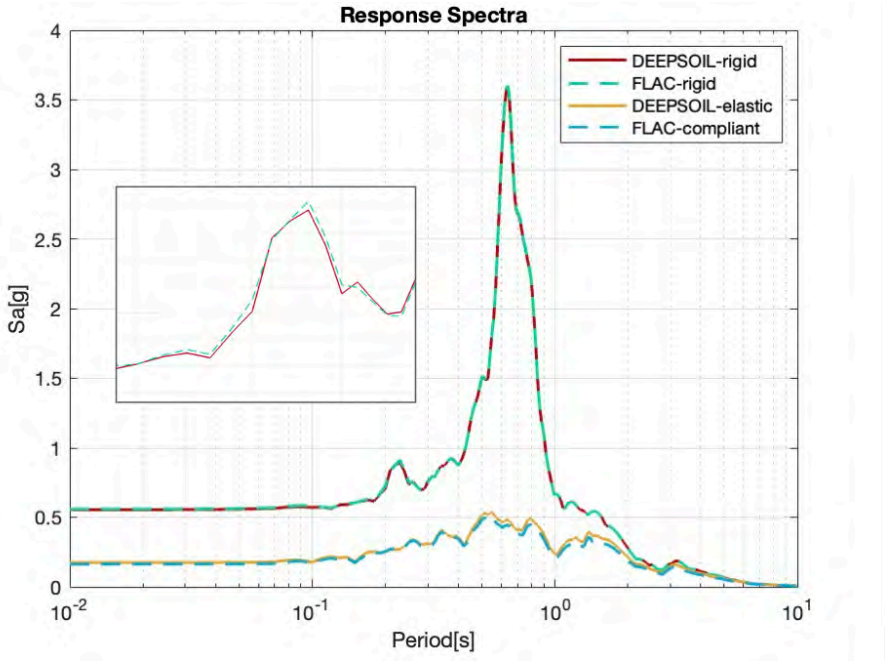

Figure 4.3 Response spectra obtained from FLAC and DEEPSOIL.

doi:10.6342/NTU202403310

To confirm the response in surface wave analysis, a profile from Beaty et al. (2002) was also used to construct the model. The theoretical dispersion curves of this profile, calculated by the stiffness matrix method and the matrix propagator method, were compared in this section, where the theoretical dispersion curves from the matrix propagator method are extracted directly from the publication of Beaty et al. (2002). The profile is displayed in Table 4.3, in which beta is shear wave velocity, alpha is compression wave velocity, and d is the thickness of each layer.

Table 4.3 Parameters used to calculate the dispersion curves shown in Figure 4.4. Beaty et al. (2002).

Layer	d (m)	α (m s^{-1})	β (m s^{-1})	ρ (g cm^{-3})
1	0.8	185	80	1.18
2	3.7	480	140	1.78
3	2.5	1650	140	1.78
4	∞	1650	1040	2.18

As shown in Figure 4.4, the dispersion curves of this profile calculated by the stiffness matrix method agree with those obtained from the matrix propagator method in the desired frequency band and the first three modes. The dispersion curve generated from numerical analysis matches the theoretical dispersion curves no matter the fundamental mode or higher mode. It jumps to the higher mode as the frequency is greater than 16Hz and jumps to the second order higher mode at around 31Hz. However, the rule of mode jump is still ambiguous. This result can merely reveal the response of the numerical model is theoretically correct, and the stability of those two approaches calculating the theoretical dispersion curves are equal in the displayed range.

doi:10.6342/NTU202403310

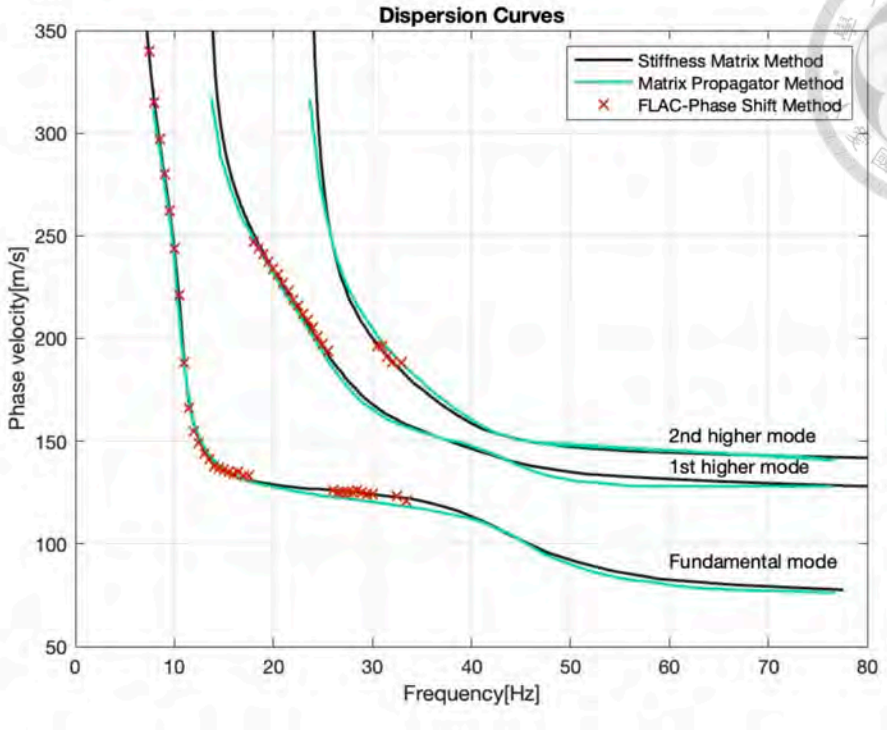

Figure 4.4 Theoretical dispersion curves from stiffness matrix method and matrix propagator method, and the experimental dispersion curve from FLAC.

4.3 Hypothetical profiles

A series of hypothetical profiles are tested, from a homogeneous profile to several layered profiles. The density is assumed to be $2000\ kg/m^3$, and Poisson's ratio is 0.4 for all cases. Theoretically, the surface waves on the homogeneous materials are non-dispersive; therefore, the phase velocities should be constant with respect to the frequency. First of all, three homogeneous profiles, $200\ m/s$, $300\ m/s$, and $400\ m/s$, are tested. Figure 4.5 displays the experimental dispersion curves and their theoretical dispersion curves of each profile. The $MAPD$ and $RMSD$ between experimental and theoretical dispersion curves are as follows: 3.39% and 7.17, 2.06% and 8.09 and 2.55% and 12.25, respectively.

doi:10.6342/NTU202403310

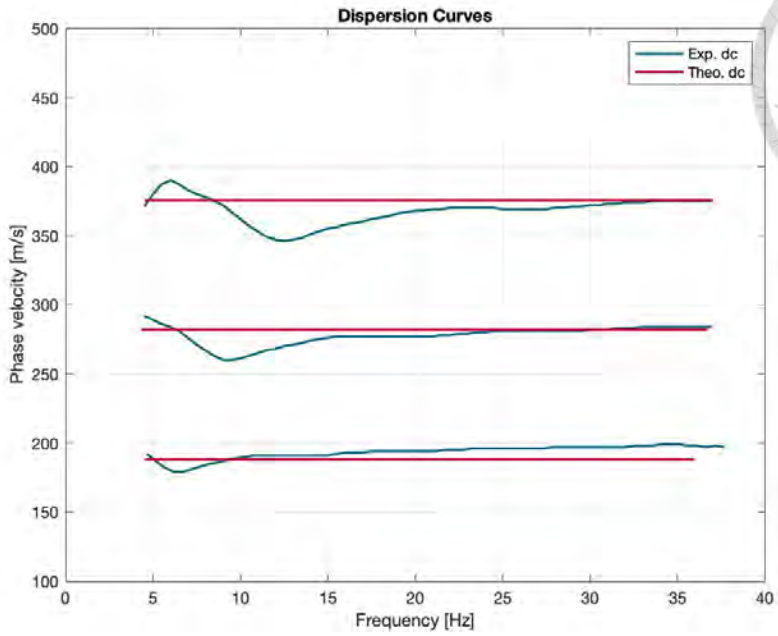

Figure 4.5 Dispersion curves of homogeneous profiles.

Following the homogeneous profiles, seven profiles with two layers are tested to examine MASW's ability to detect severe change. As shown in Figure 4.6, the interface is 10m below the surface, and the upper layer is $100\ m/s$ in shear wave velocity profile in each profile. The shear wave velocities in the second layer are $150,\ 200,\ 250,\ 300,\ 400,\ 500$, and $600\ m/s$ for profiles 1 to 7, respectively.

The experimental dispersion curves are shown in Figure 4.6, where the curves of the last three profiles are almost identical; however, the velocity deviation in the second layer can be up to 200m/s. Comparing the experimental dispersion curve of profile 7 with the theoretical dispersion curves of each profile, profiles 5 and 6 can generate even lower $MAPD$ than using its true profile (Figure 4.7). These results reveal that the accuracy will decrease as the impedance contrast increases.

doi:10.6342/NTU202403310

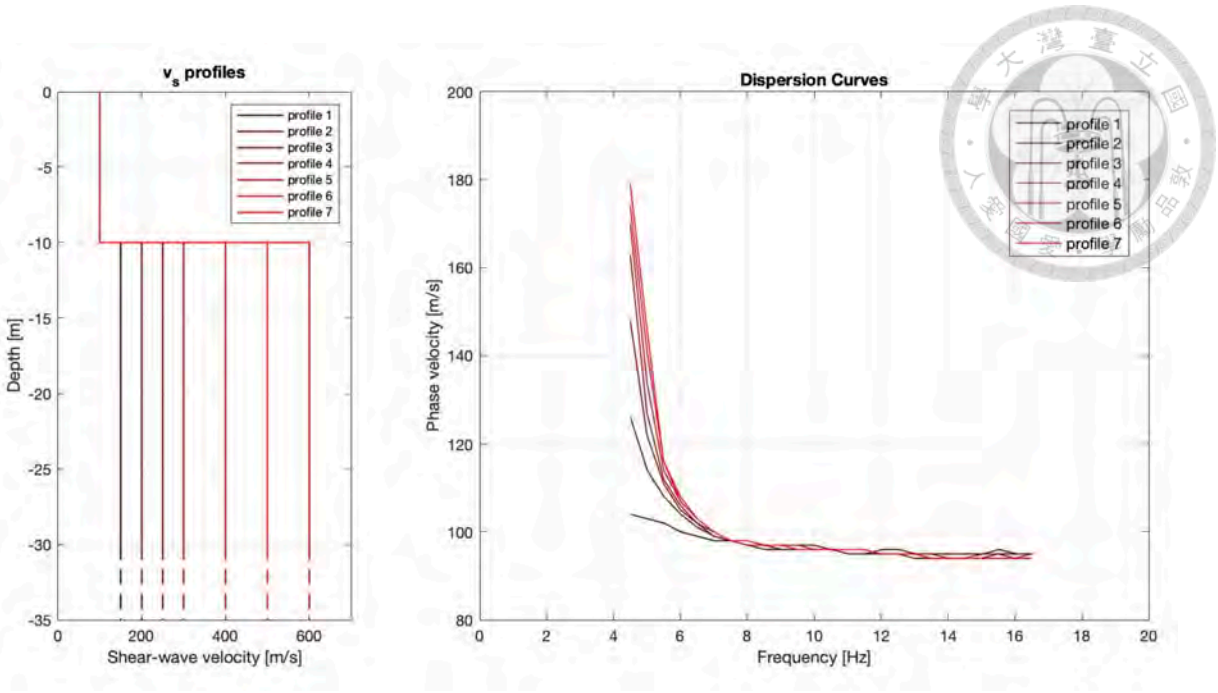

Figure 4.6 Shear wave velocity and dispersion curves of second layered profiles.

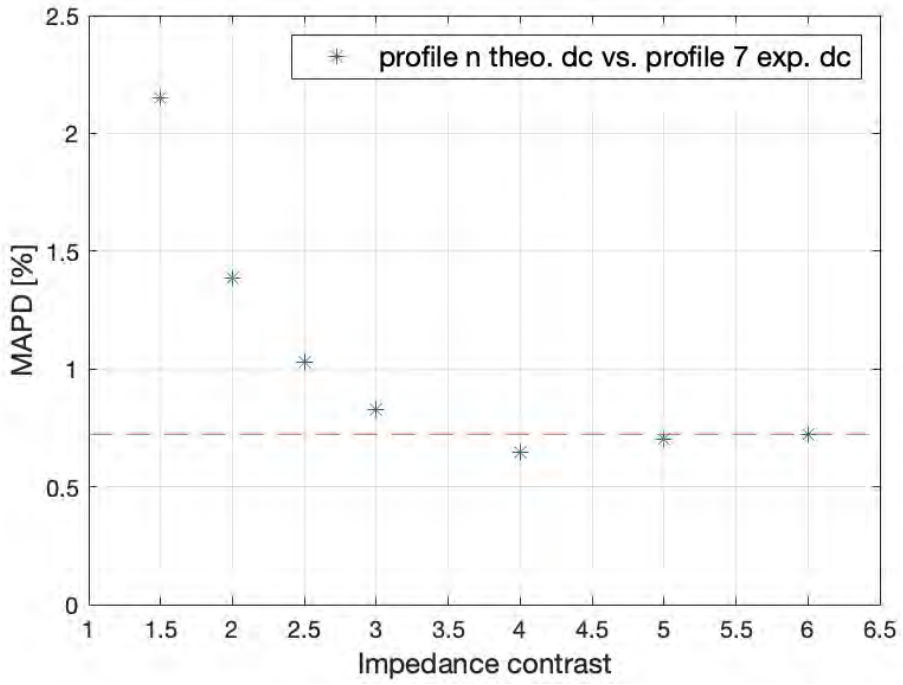

Figure 4.7 Deviation of profile n theoretical dispersion curve and profile 7 experimental. dispersion curve.

doi:10.6342/NTU202403310

Profiles with three layers are tested in three scenarios: velocity increases with depth, increasing profile with a soft layer, and increasing profile with a stiff layer. In the first scenario, each layer is 10 m thick, and the shear wave velocity is $100\ m/s$ faster than the upper layer. As shown in Figure 4.8, profile 8 starts from $100\ m/s$, and profile 9 starts from $200 m/s$.

Profiles with increasing velocity have deviation $MAPD$ and $RMSD$ of 0.50%, 0.67 for profile 8, 1.6994%, and 7.32 for profile 9 compared to the true profiles (Figure 4.10). The experimental dispersion curves of these two profiles follow the fundamental mode well, although the case with higher velocities shows a little unstable.

The second scenario aims to simulate the profiles where the velocity generally increases with depth but contains a soft layer. Figure 4.10 displays the shear wave velocity profiles under the second scenario, where the shear wave velocity increases from 200 m/s to 300 m/s. Profile 10 has a 10m thick soft layer from 10m to 20m below the surface, and profile 11 has a 5m thick soft layer from 10m to 15m below the surface. Each soft layer is 150 m/s in shear wave velocity. The experimental dispersion curves of these two cases jump to the higher mode in the high-frequency band, and the mode jumps at a higher frequency in profile 11 than in profile 10. However, there is no obvious pattern for accurately locating the soft layer from the experimental dispersion curve. In the case of inversion analysis using only fundamental mode, this mode jump can be easily detected and removed, and therefore the loss in the information of the shallow layer may be its tradeoff.

The last scenario is to simulate the profiles where the velocity generally increases with depth

doi:10.6342/NTU202403310

but inserts a stiff layer, displayed in profiles 12 and 13 (Figure 4.13). Profile 12 consists of three 10m thick layers and shear wave velocities of 200m/s, 350m/s, and 300m/s from top to bottom. The thickness of profile 13 from top to bottom are 10m, 5m, and 15m, and the shear wave velocity is 200m/s, 350m/s, and 250m/s from top to bottom. In contrast with the second scenario, the experimental dispersion curves follow the fundamental mode in the high-frequency band. As shown in Figures 4.14 and 4.15, the experimental dispersion curves become unstable in the low-frequency band; they do not jump to a certain mode. In this kind of case, some segments of the unstable band may be hard to distinguish and mistaken as the fundamental mode, increasing the inaccuracy in inversion analysis considering only the fundamental mode.

In conclusion, three main pitfalls of MASW, which may encounter in the field test, are spotted by the hypothetical profiles:

- The increase in impedance contrast may lead to inaccuracy in inversion analysis.
- Embedding a soft layer in profiles with shear wave velocity generally increasing with depth may lead to the mode jump in the high-frequency band of experimental dispersion curves.
- Inserting a stiff layer in profiles with shear wave velocity generally increasing with depth may disturb the low-frequency band of experimental dispersion curves.

Of the problems listed above, the first one can be solved by broadening low-frequency information, and the last two need further study revealing the fixed pattern in the behavior of the experimental dispersion curves.

doi:10.6342/NTU202403310

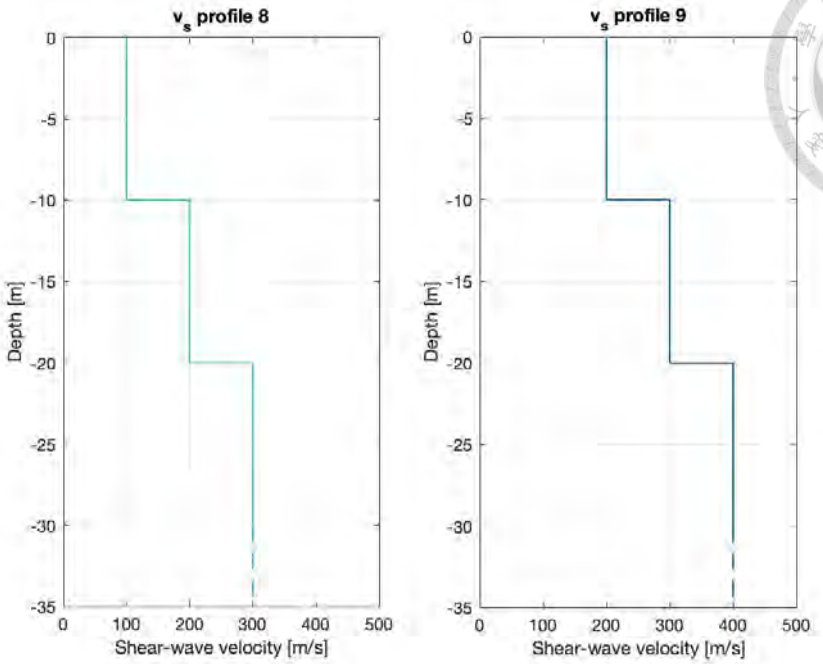

Figure 4.8 Profiles of shear wave velocity increase with depth.

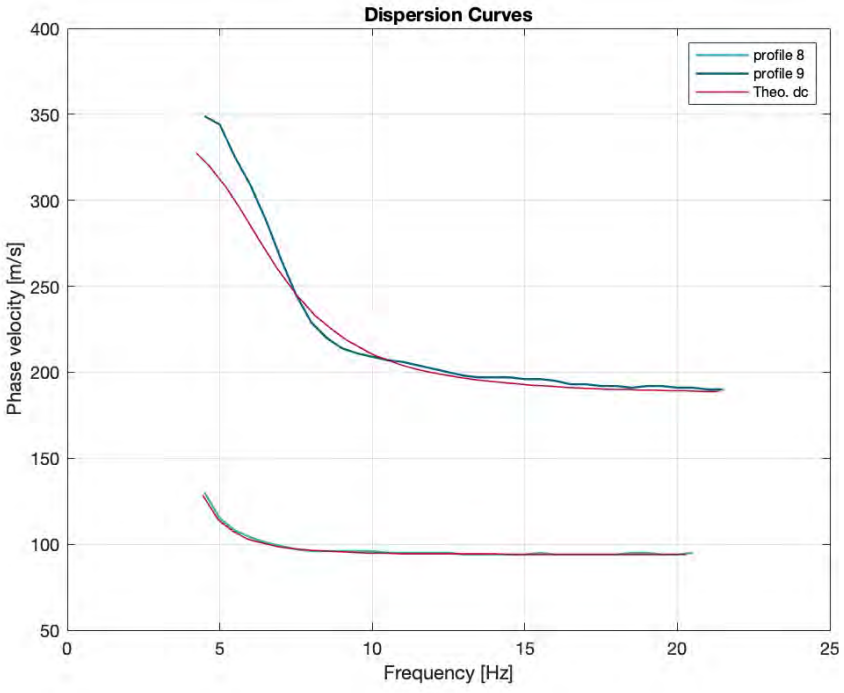

Figure 4.9 Dispersion curves for profile 8 and 9.

doi:10.6342/NTU202403310

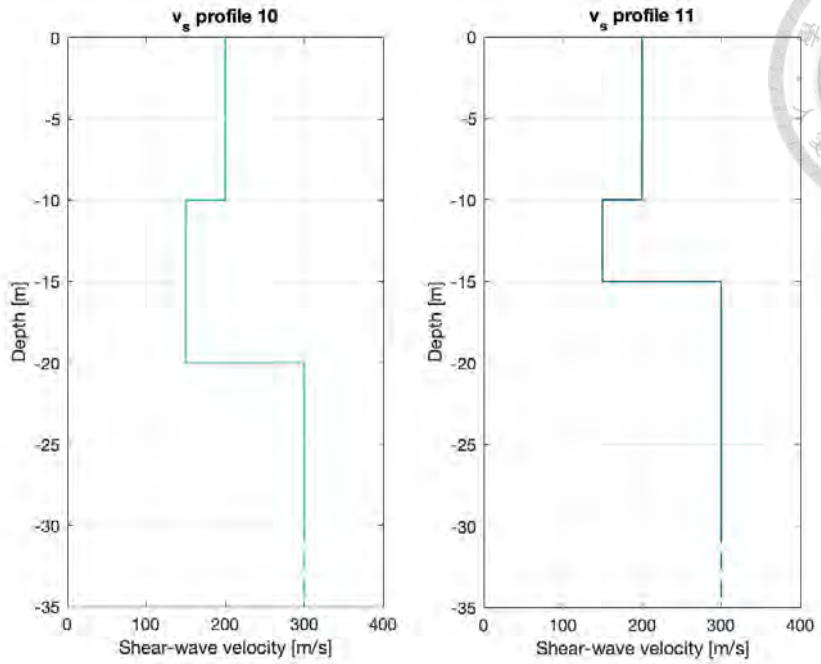

Figure 4.10 Profiles of shear wave velocity increase with depth but contain a soft layer.

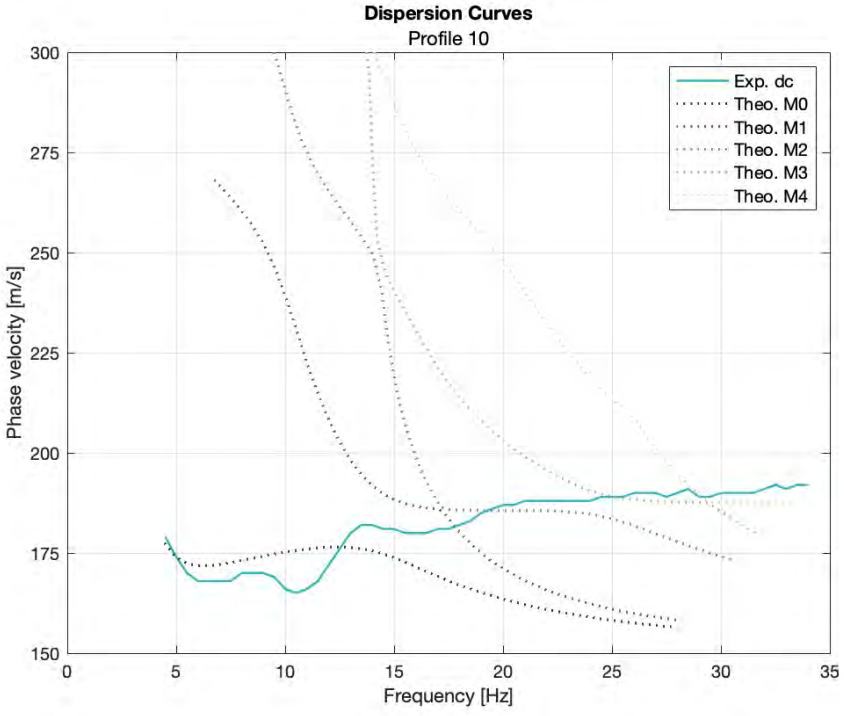

Figure 4.11 Experimental dispersion curve and theoretical dispersion curves from fundamental mode to 4th higher mode of profile 10.

doi:10.6342/NTU202403310

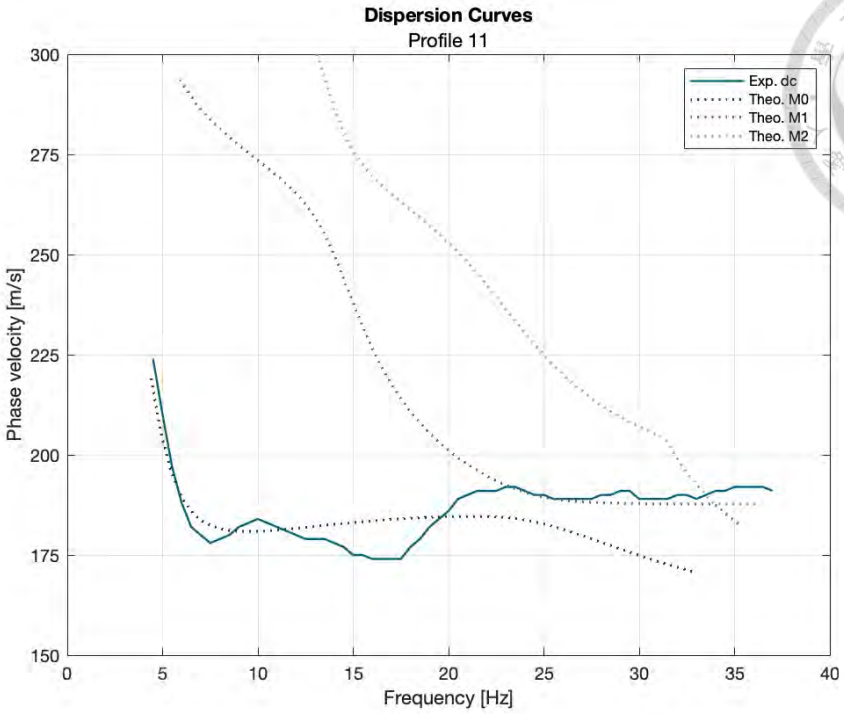

Figure 4.12 Experimental dispersion curve and theoretical dispersion curves from fundamental mode to 2nd higher mode of profile 11.

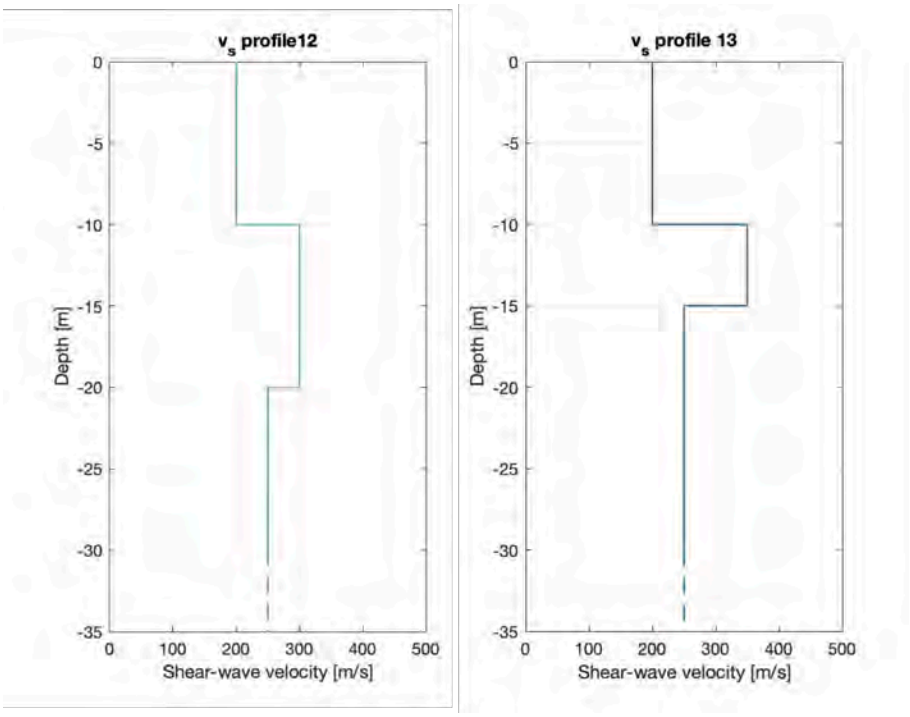

Figure 4.13 Profiles of shear wave velocity increase with depth but contain a stiff layer.

doi:10.6342/NTU202403310

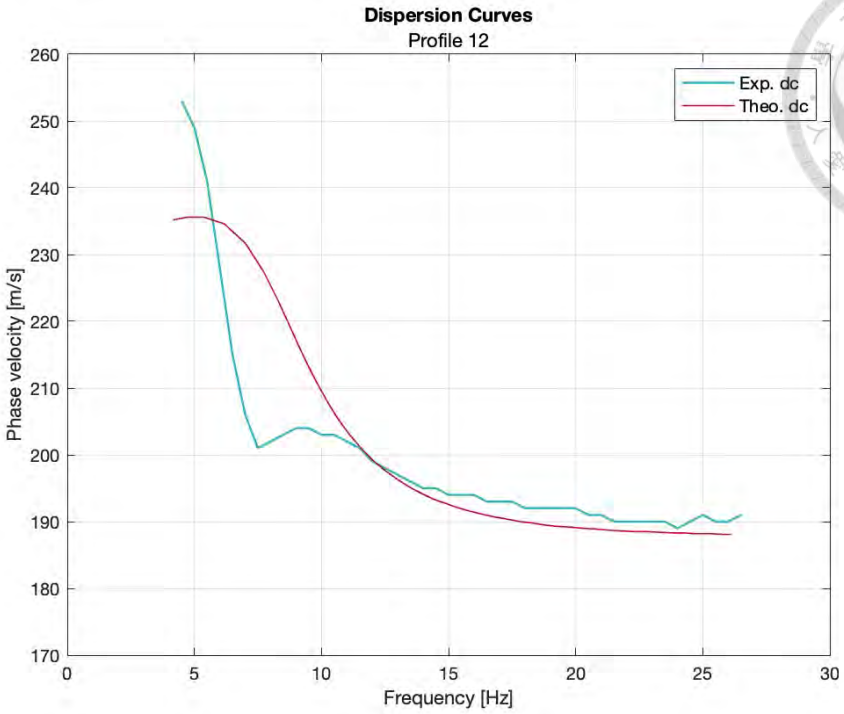

Figure 4.14 Experimental dispersion curve and theoretical dispersion curves of profile 12.

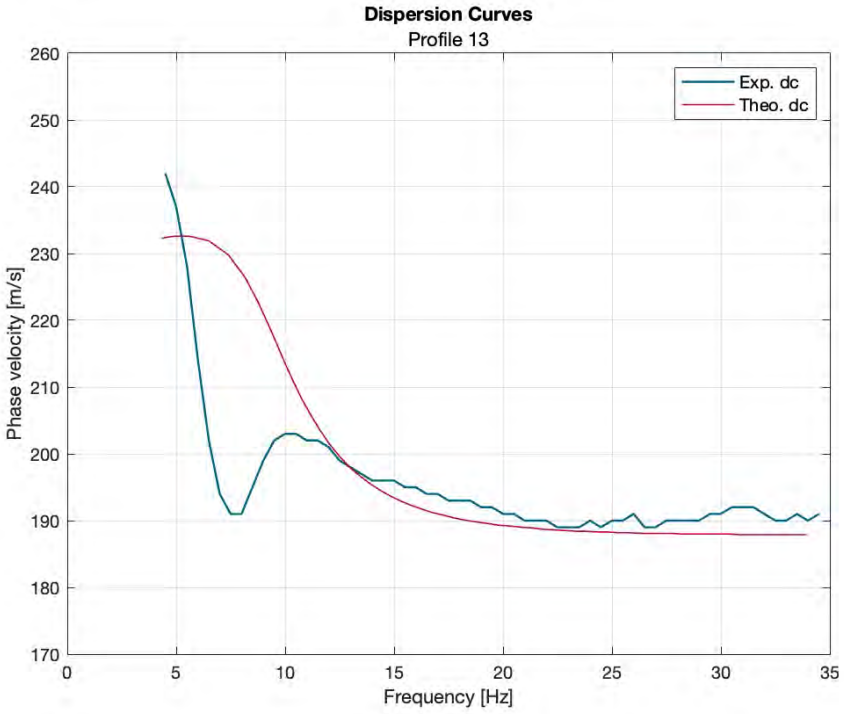

Figure 4.15 Experimental dispersion curve and theoretical dispersion curves of profile 13.

doi:10.6342/NTU202403310

4.4 Lotung LSST

The model of Lotung LSST is 100m in length and 40 m in depth with a 0.25m grid size, and the shear wave velocity profile is displayed in Figure 4.16, where the dots are the velocity measured by cross-hole tests in WECC program (1986). According to EPRI (1993), the Poisson's ratio is assumed to be 0.48, and density is assumed to be $2000\ kg/m^3$.

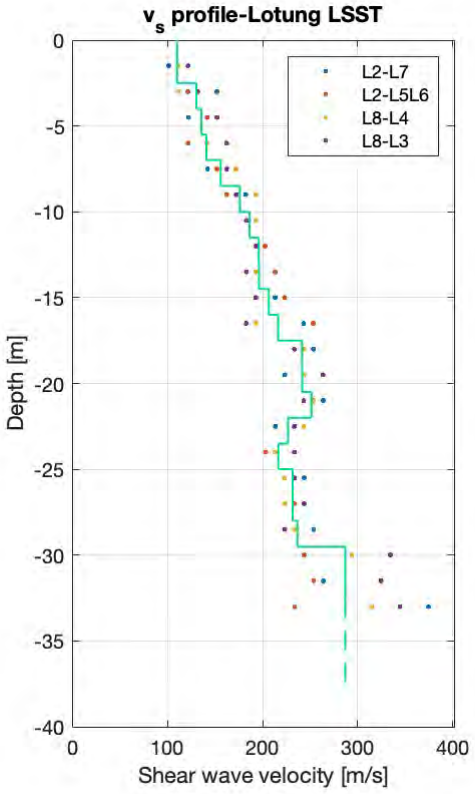

Figure 4.16 Shear wave velocity profile of the model of Lotung LSST.

Figure 4.17 shows the multi-channel record from the numerical analysis and its dispersion image. The dispersion curve is extracted from about 4Hz to 26Hz, which is within the scope concerning the grid size. Compared with the theoretical dispersion curve calculated from the true profile (figure 4.18), the deviation is 1.54% and 5.76 for $MAPD$ and $RMSD$, respectively. Two curves fit very well when the frequency is greater than 8Hz.

doi:10.6342/NTU202403310

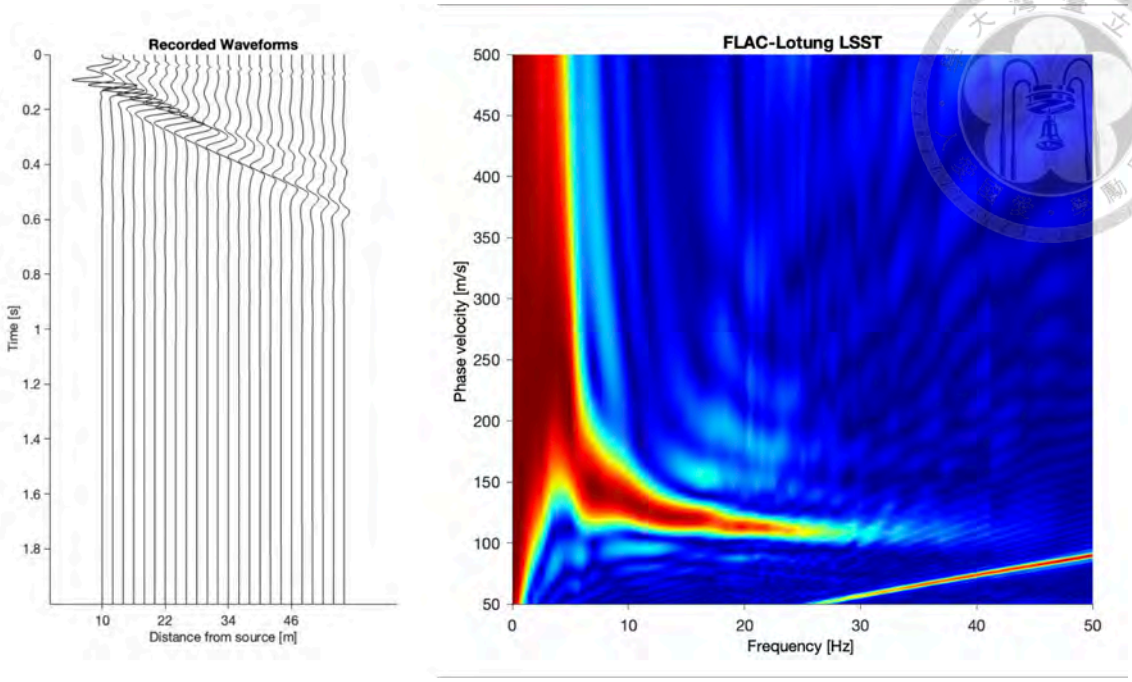

Figure 4.17 The multi-channel record (left) and its dispersion image (right).

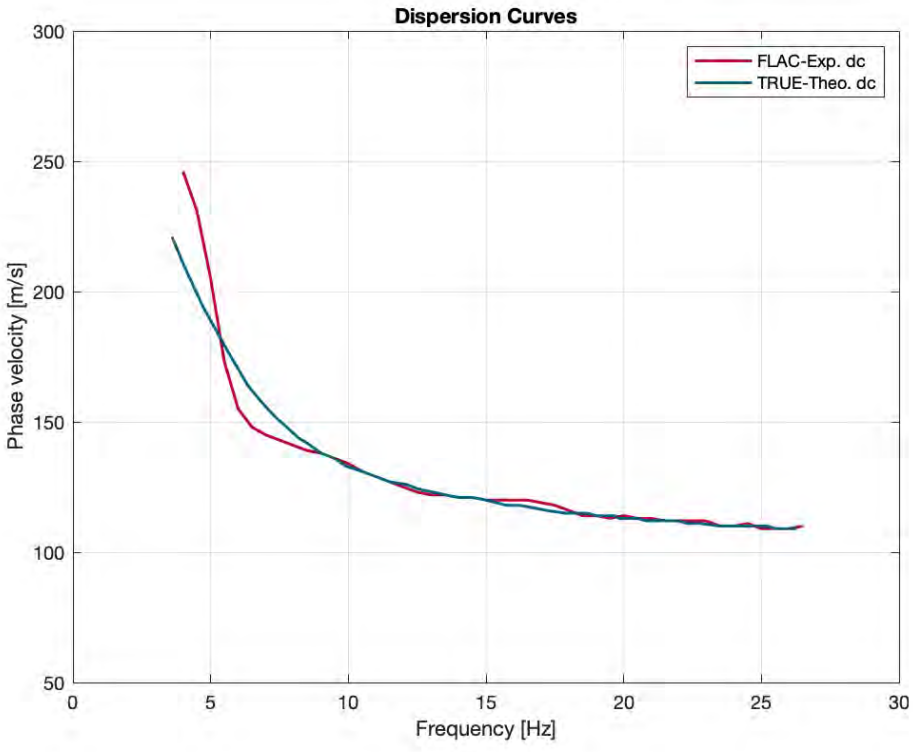

Figure 4.18 The extracted experimental dispersion curve and theoretical dispersion curve.

doi:10.6342/NTU202403310

4.4.1 Comparison of different layering approaches

To observe the qualitative difference between layering approaches, two approaches are compared. One uses the same layer as the actual profile, which is 1.5m for each layer, and the other uses the SIM concept to layer. Thirty profiles with $MAPD < 2.5\%$ and $RMSD < 7$ are selected and shown in Figure 4.19. Profiles with 1.5m layers show better accuracy within 10m below the surface, but the deviation becomes larger than the profiles layered with the SIM concept as the depth is deeper than -10m (Table 4.4). This result is due to the calculation process of $MAPD$ and $RMSD$ and the distribution of data points on the curves. The error may be higher in the low-frequency band, which has a lower density of data points, and the profiles with denser layers may aggravate the issue.

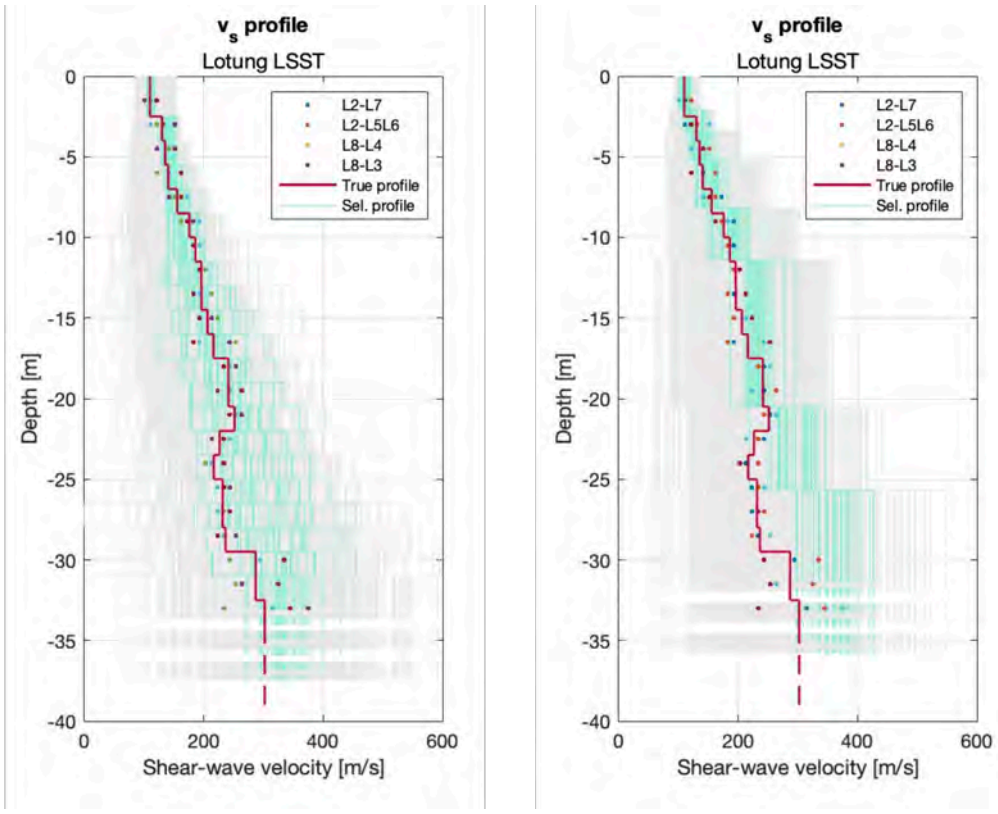

Figure 4.19 Selected profiles from two layering approaches.

doi:10.6342/NTU202403310

Table 4.4 The average and standard deviation of the selected profiles in each layer.

Depth [m]	True vs [m/s]	21 layers [m/s (σ)]	8 layers [m/s (σ)]
-2.5	109.85	111.23 (2.99)	112.04 (5.14)
-4	130.22	138.46 (8.25)	126.94 (11.19)
-5.5	135.39	142.51 (7.70)	137.48 (11.76)
-7	140.65	148.60 (9.70)	149.68 (13.44)
-8.5	155.65	155.63 (10.95)	
-10	175.96	164.21 (16.95)	185.99 (18.64)
-11.5	186.02	168.3 (17.47)	
-13	195.89	175.2 (24.09)	
-14.5	196.23	196.37 (27.04)	
-16	206.35	209.00 (33.84)	233.11 (20.06)
-17.5	216.29	215.23 (35.20)	
-19	241.29	230.70 (36.17)	
-20.5	241.45	241.72 (38.19)	
-22	251.44	256.65 (44.29)	
-23.5	226.45	276.14 (45.50)	295.81 (29.22)
-25	216.61	278.97 (49.92)	
-26.5	231.65	288.49 (51.63)	
-28	231.54	297.12 (61.66)	
-29.5	236.56	314.29 (53.36)	359.2 (32.38)
-31	287.03	324.66 (50.80)	
-32.5	286.9	336.64 (34.51)	

doi:10.6342/NTU202403310

4.4.2 Solution for the numerical analysis

Regarding the result in the previous section, the inversion analysis in the following sections will adopt the SIM concept to layer the profile. In this section, the whole process of inversion analysis will be conducted, and a final solution will be given, and this will be the same process adopted in processing the field test data. The iterative process of finding the solution to the experimental dispersion curve will start with assuming a profile to generate a theoretical dispersion curve. To assume a shear wave velocity profile, the velocity of the first layer is given as a random number nearby the velocity of the first layer in the SIM profile. The velocity of the next layer will be assumed by giving an increment or decrement to the velocity of the previous layer, in which the amount of change in velocity will increase with the depth, and the increment has a higher possibility. The maximum investigative depth is assumed to be half of the maximum wavelength of the dispersion curve.

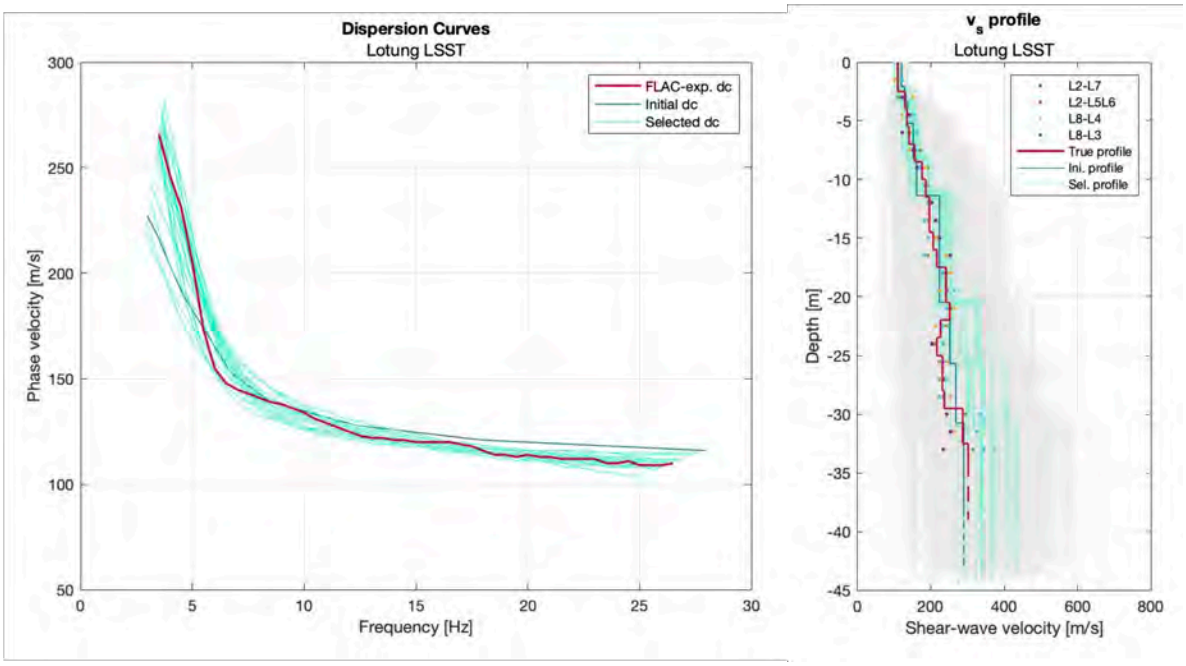

Figure 4.20 The selected profiles and their dispersion curves.

doi:10.6342/NTU202403310

Then, if the assumed profile can generate a theoretical dispersion curve that has $MAPD < 2.5\%$ and $RMSD < 7$ in comparison with the experimental dispersion curve, the profile will be taken as a candidate for the solution (Figure 4.20). Lastly, if all candidates seem reasonable, the profile with the lowest $MAPD$ will generally be the final solution. In this case, the final solution is displayed in Figure 4.20, and its $MAPD$ and $RMSD$ are 1.34% and 4.42, respectively.

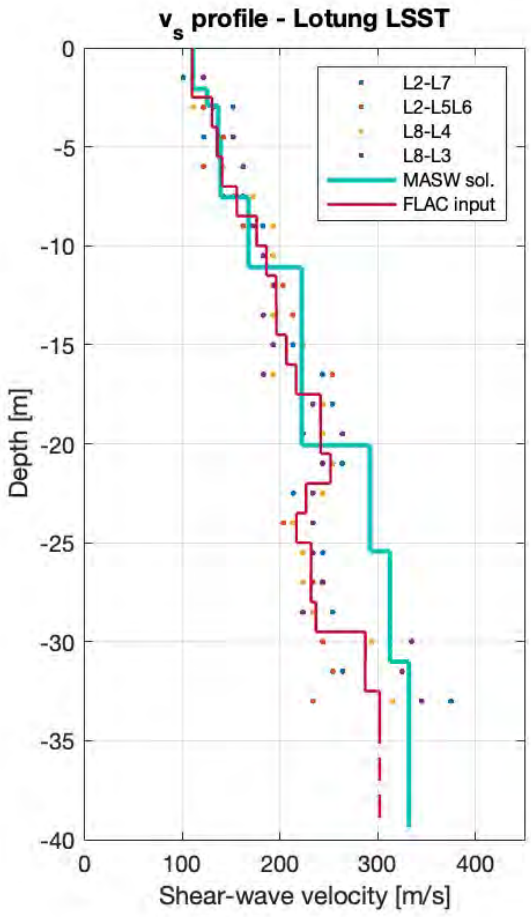

Figure 4.21 the final solution for the numerical analysis of Lotung LSST.

doi:10.6342/NTU202403310

4.4.3 Compared with field test data

In the field test of MASW at the Lotung LSST site, five survey lines were surveyed with 2D gather and microtremor test (Figure 4.24). Each survey line's first and last shot records are extracted to calculate the experimental dispersion curves. The survey lines NN1, NN2, and SS are 27.6m long with 1.2m receiver spacing, and the survey lines WW and EE are 46m long with 2m receiver spacing. The location of each borehole of the cross-hole tests is also displayed in Figure 4.24.

Figure 4.22 displays those dispersion curves compared with the dispersion curve generated from the numerical analysis. Those dispersion curves' trends are generally matched, and the average $MAPD$ between the dispersion curves from the field test and the dispersion curve from the numerical analysis is 5.66%. On the other hand, assuming the Lotung LSST site is horizontally layered, and the differences between the values of the four cross-hole tests are solely due to experimental errors, two theoretical dispersion curves corresponding to the maximum and minimum shear wave velocity profiles can be generated. Figure 4.23 shows that all field test dispersion curves fall within the range enclosed by those two theoretical dispersion curves. From the perspective of the dispersion curve, although those two theoretical dispersion curves may not correspond to the upper and lower bound of the dispersion curve, the result still illustrates that the MASW active test can give a consistent and reasonable result. Based on this assumption, as long as the inversion analysis process is rigorous enough, the shear wave velocity profile generated from MASW can also be reliable in principle.

doi:10.6342/NTU202403310

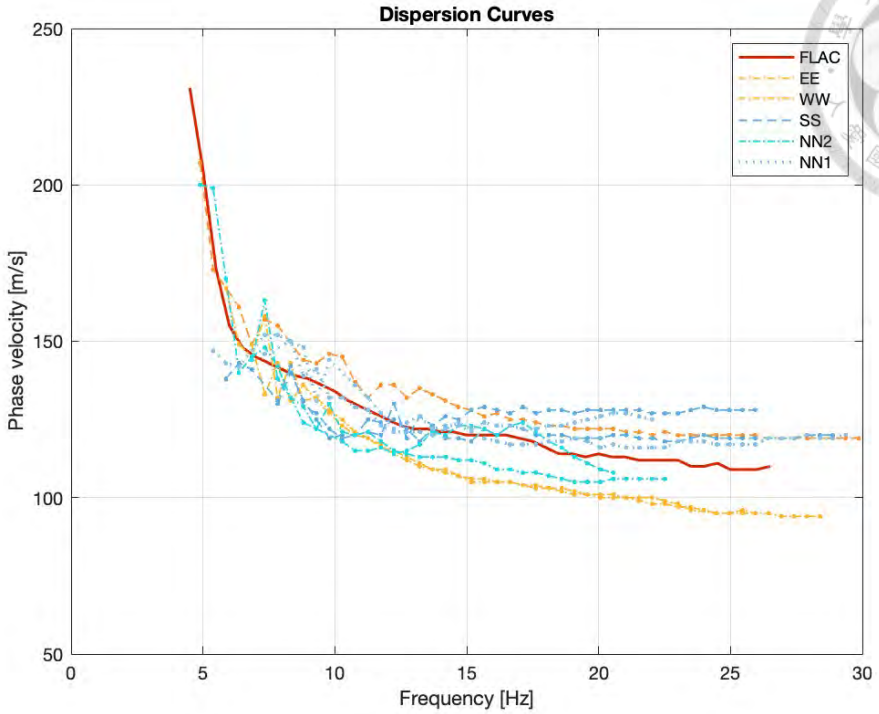

Figure 4.22 Comparison of the experimental dispersion curves from field test and numerical analysis.

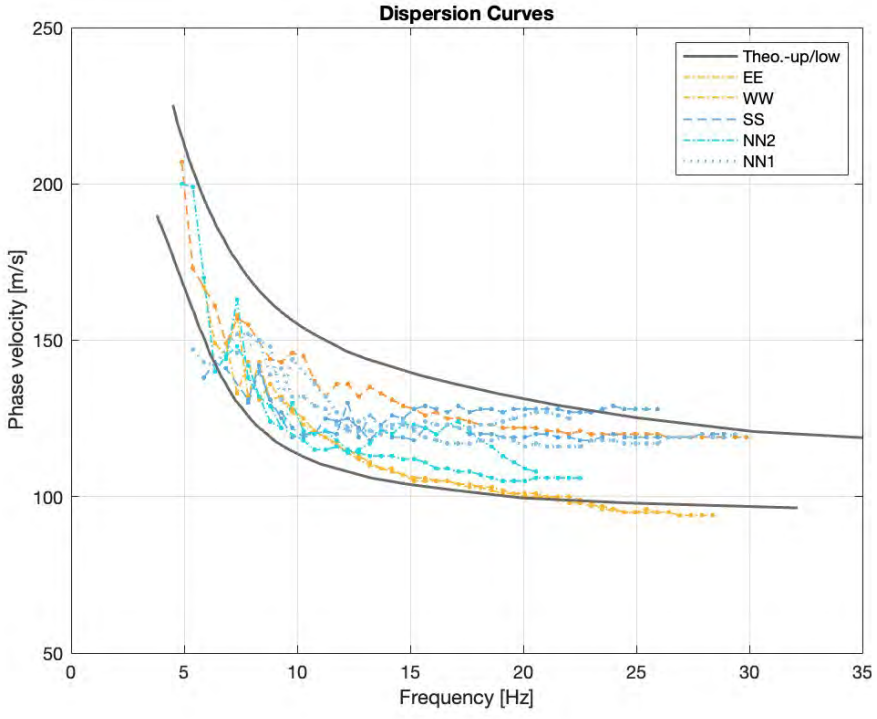

Figure 4.23 The theoretical dispersion curves from the maximum and minimum value of the cross-hole test and the experimental dispersion curves from field tests.

doi:10.6342/NTU202403310

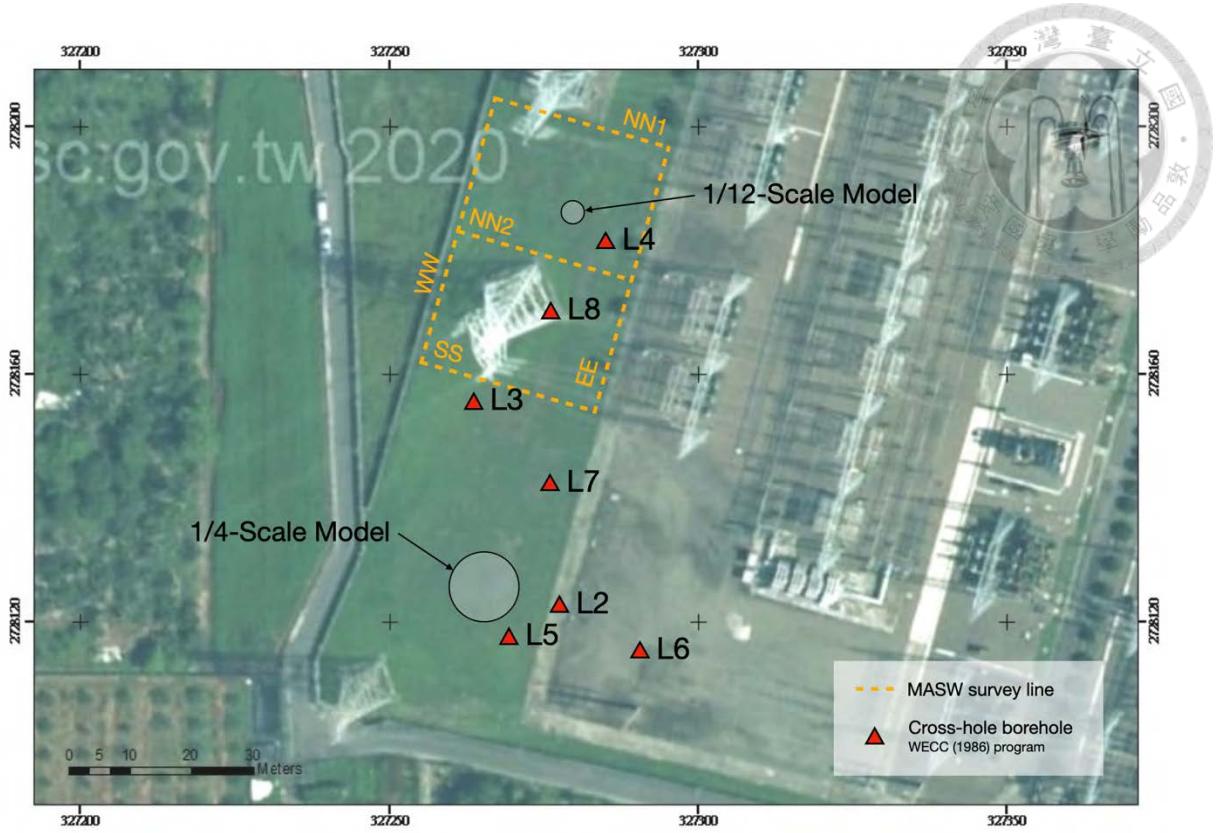

Figure 4.24 Position of the MASW survey lines and the location of the boreholes used in the cross-hole tests.

doi:10.6342/NTU202403310

Chapter 5 Field test

This section presents the results of the Multi-Channel Analysis of Surface Waves (MASW) field test conducted at TSMIP sites. Out of the 17 sites, 6 were not investigated previously and lacked velocity profiles. The final solution of the inversion analysis will be provided along with the suspension logging profiles for each site to compare the obtained results with the existing data. The corresponding $v_{s,30}$ values will also be compared. The behavior of the dispersion curve will be discussed, along with additional discussions for specific sites. The shear wave velocity profiles for the non-investigated sites will be presented, and the 2D profiles of the survey line for each site will be included in the appendix.

5.1 TSMIP sites

The selection of test sites takes into account the site condition and seismic site classification. The primary requirement for a site is to have sufficient space to accommodate the survey line. This criterion is easily fulfilled as most TSMIP stations are located within local elementary schools. Considering the variety of the selected sites, the sites with existing data have been chosen to cover as wide a range as possible, encompassing most bands of the class. On the other hand, the non-investigated sites have been randomly selected from functioning seismic stations. Figure 5.1 displays the selected sites in northern Taiwan, and Figure 5.2 depicts the rest. The other information on the test sites is listed in Table 5.1 and Table 5.2. In Table 5.2, the $v_{s,30}$ of the sites without existing velocity profiles are predicted by the model proposed by Kwok et al. (2018).

doi:10.6342/NTU202403310

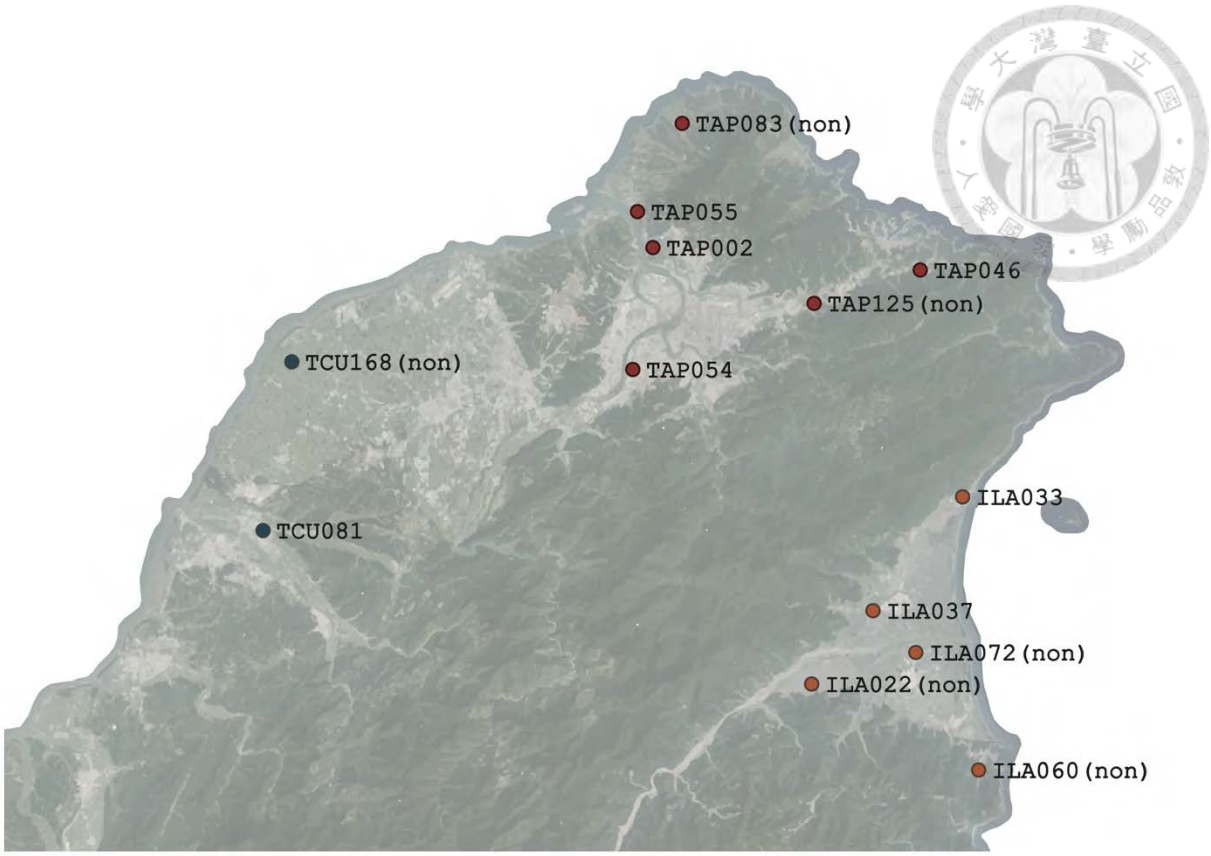

Figure 5.1 The selected sites in the northern part of Taiwan, including investigated and non-investigated sites.

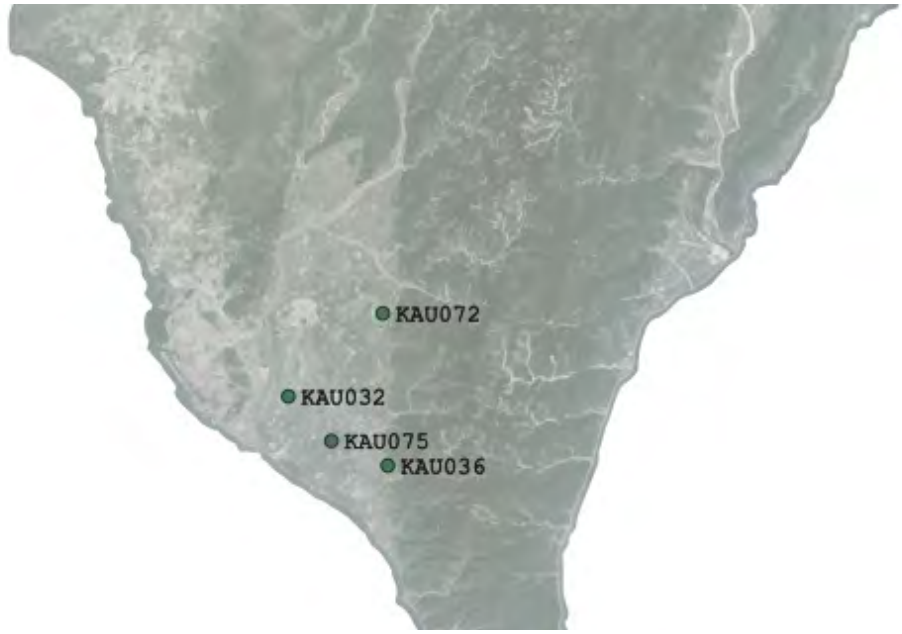

Figure 5.2 The selected sites with existing data in the southern part of Taiwan.

doi:10.6342/NTU202403310

Table 5.1 Selected TSMIP stations with existing velocity profiles.

Station code	Station name	Classification	$v_{s,30}$
TAP002	關渡國小	C	373.95
TAP046	瑞亭國小	B	822.03
TAP054	台北氣象站	D	309.74
TAP055	淡水氣象站	C	444.64
ILA033	頭城國小	D	253.57
ILA037	員山國小	D	212.93
TCU081	新竹氣象站	C	427.14
KAU032	仙吉國小	D	190.7
KAU036	新埤國小	D	234.59
KAU072	崇文國小	C	487.13
KAU075	南州國小	D	196.82

Table 5.2 Selected TSMIP stations without existing velocity profiles.

Station code	Station name	Classification	Recommended $v_{s,30}$
TAP083	三芝國小	-	497.80
TAP125	汐止國小	-	413.85
ILA022	三星國小	-	779.84
ILA060	永樂國小	-	678.12
ILA072	興中國中	-	-
TCU168	新屋氣象站	-	476.23

doi:10.6342/NTU202403310

5.2 Sites with existing data

This section will first review the findings in the experimental dispersion curves obtained from the field test and discuss some special cases. In the end, the final solutions of the surface wave analysis will be displayed and compared with the results from PS-logging.

First, the experimental dispersion curves generated by three setups, the 10m offset and 5m offset forward and backward shot, show the MASW active test can generate consistent results in terms of dispersion curve. In Figure 5.3 and other following figures of experimental dispersion curves, it is clear that the three experimental dispersion curves match well with each other. Besides, the 10m offset shot gather shows better continuity in the low-frequency band in some cases (Figure 5.3); however, there is no significant difference between the 5m and 10m offset shot gather in most cases. In addition to the experimental dispersion curve from the active test, the dispersion curve obtained from the passive test can append well to the curves of the active test in almost every case.

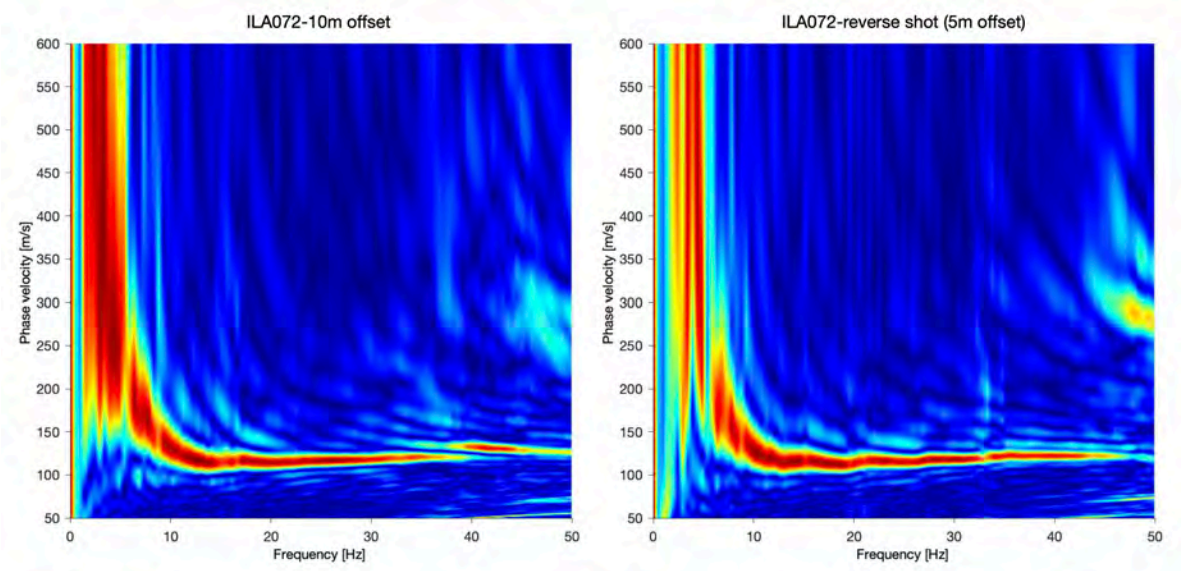

Figure 5.3 The example experimental curves from 5m and 10m offset shot in site ILA072.

doi:10.6342/NTU202403310

In site, TAP055, two survey lines were set and formed a T shape geometry, where the survey line L1 intersected with L2 at 16m of L2 (Figure 5.4). Figure 5.5 shows the experimental dispersion curves of survey lines L1 and L2. Initially, the dispersion curve of the L2 seems normal in curves from active and passive tests since they append well to each other and have no obvious inconsistency. Therefore, the whole curve is believed to be the fundamental mode. On the other hand, the dispersion curve of L1 is unstable in the curve from the passive test and is believed to be out of use. However, by overlaying the two curves, the whole curve of L2 seems to be dominated by the higher mode otherwise. Consequently, the fundamental mode is assumed as shown in Figure 5.5 and used in the preliminary inversion analysis.

Figure 5.4 The distribution of survey lines and borehole of TAP055.

doi:10.6342/NTU202403310

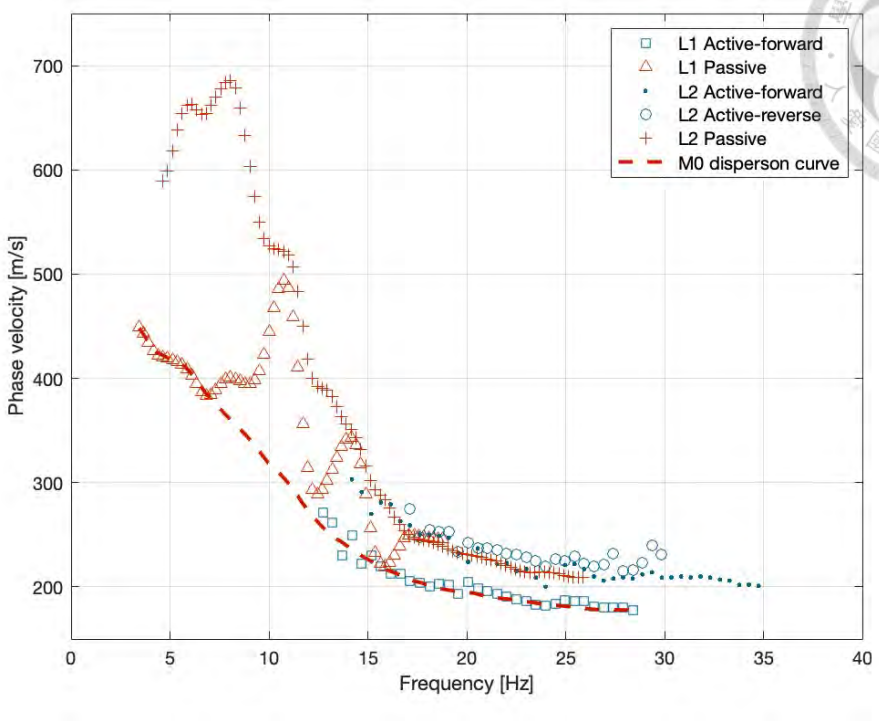

Figure 5.5 The experimental dispersion curves from active and passive test of L1 and L2, and the assumed fundamental mode dispersion curve used in inversion analysis.

In the left of Figure 5.6 and 5.7, the shear wave velocity profile is found by manually adjusting the layers and shear wave velocity to generate a theoretical dispersion curve that matches the assumed fundamental mode. The final solution for L1 shows a good agreement with the PS-logging profile, which may be evidence for the correction of the assumed fundamental mode. In the right of Figure 5.6, the fundamental and first higher mode theoretical dispersion curves are overlayed on the experimental dispersion curves of L1 and L2. From the first higher mode trend, the low-frequency band of the experimental dispersion curve of L2 is inferred that it is dominated by the higher mode dominates, and the fundamental mode may still dominate the high-frequency band.

doi:10.6342/NTU202403310

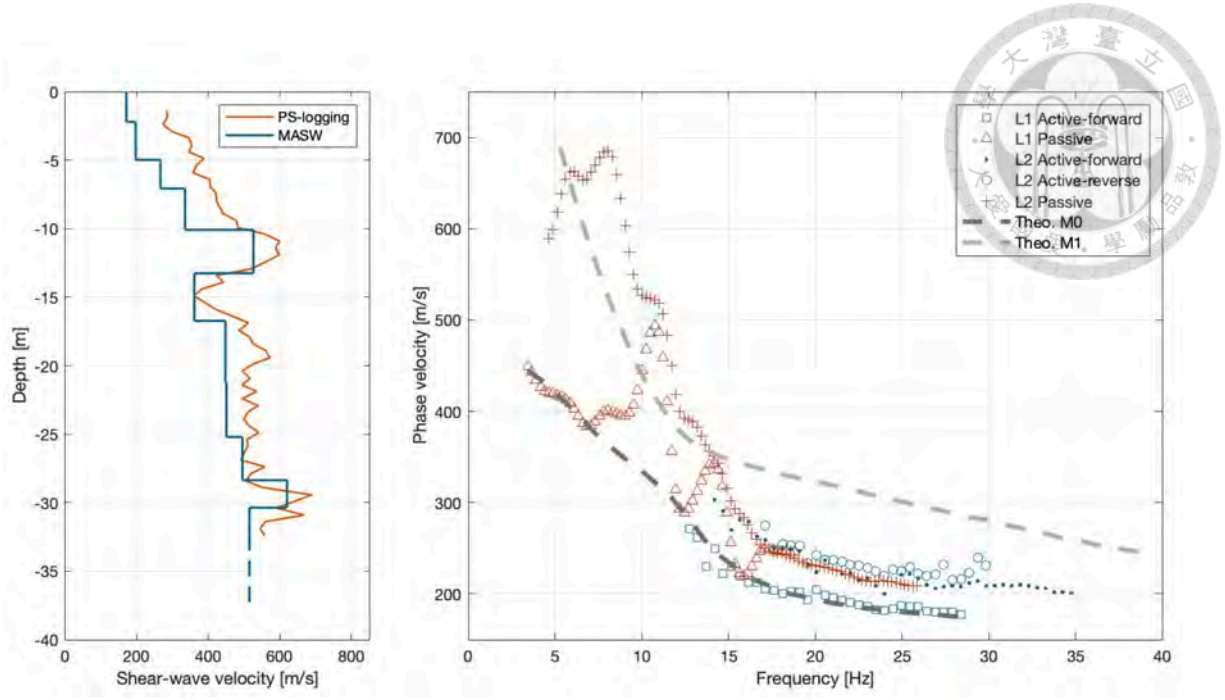

Figure 5.6 Comparison between the final solution of the inversion analysis using assumed fundamental mode experimental dispersion curve and the profile from PS-logging (left), and the fundamental and 1st higher mode theoretical dispersion curves of the final solution.

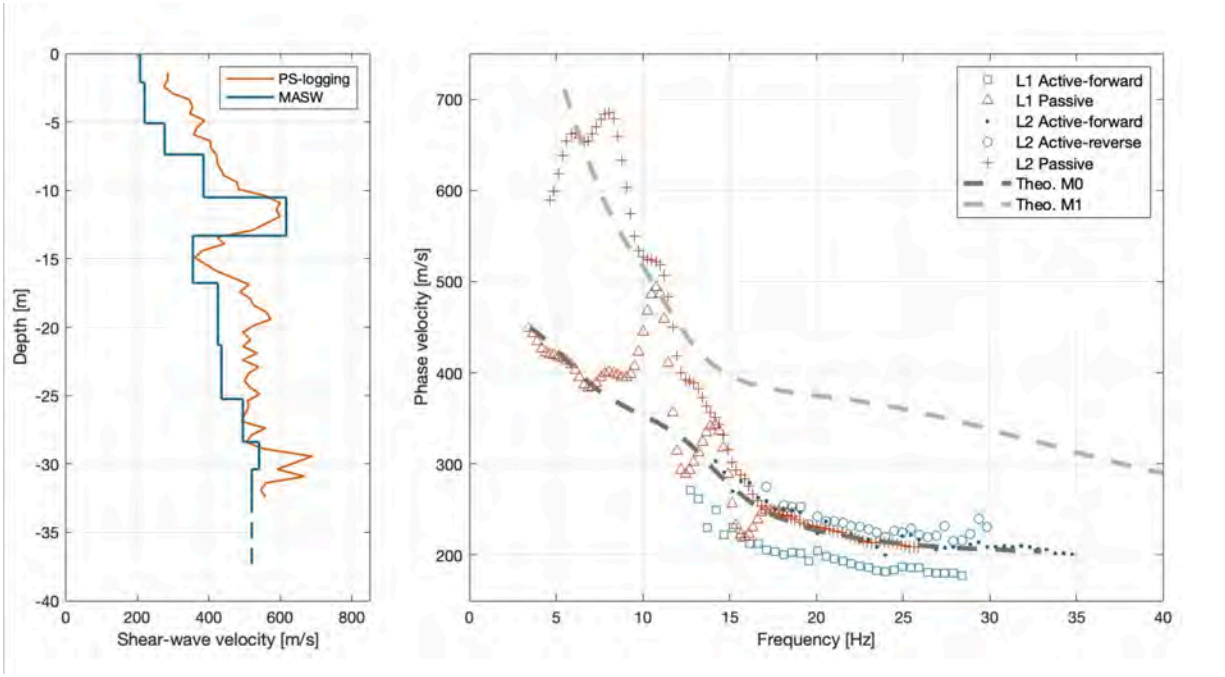

Figure 5.7 Comparison between the final solution of the inversion analysis using assumed fundamental mode experimental dispersion curve for L2 and the profile from PS-logging (left), and the fundamental and 1st higher mode theoretical dispersion curves of the final solution of L2.

doi:10.6342/NTU202403310

According to the results in Figure 5.6, the experimental dispersion curve of the active test in L2 is appended to the experimental dispersion curve of the passive test in L1 to find the shear wave velocity profile for L2. As shown in the left of Figure 5.7, the result for L2 is closer to the profile from PS-logging in the shallow layers; and in the right of Figure 5.7, it is more clear evidence that the higher mode dominates the low-frequency band of the experimental dispersion curve of L2.

Referring to the conclusion in chapter 4.3, the accuracy will lose when encountering a severe change within the depth of investigation. Figure 5.8 displays the profiles selected with $MAPD < 3\%$ in the cases of TAP002, TAP046, and ILA033. Although the trend seems similar to the PS-logging profile in each case, the specific velocity value in the deep layer is hard to determine. With the receiver's limitation and the survey line's length, the depth of investigation may be restricted to about 10 to 15m below the surface in such a scenario.

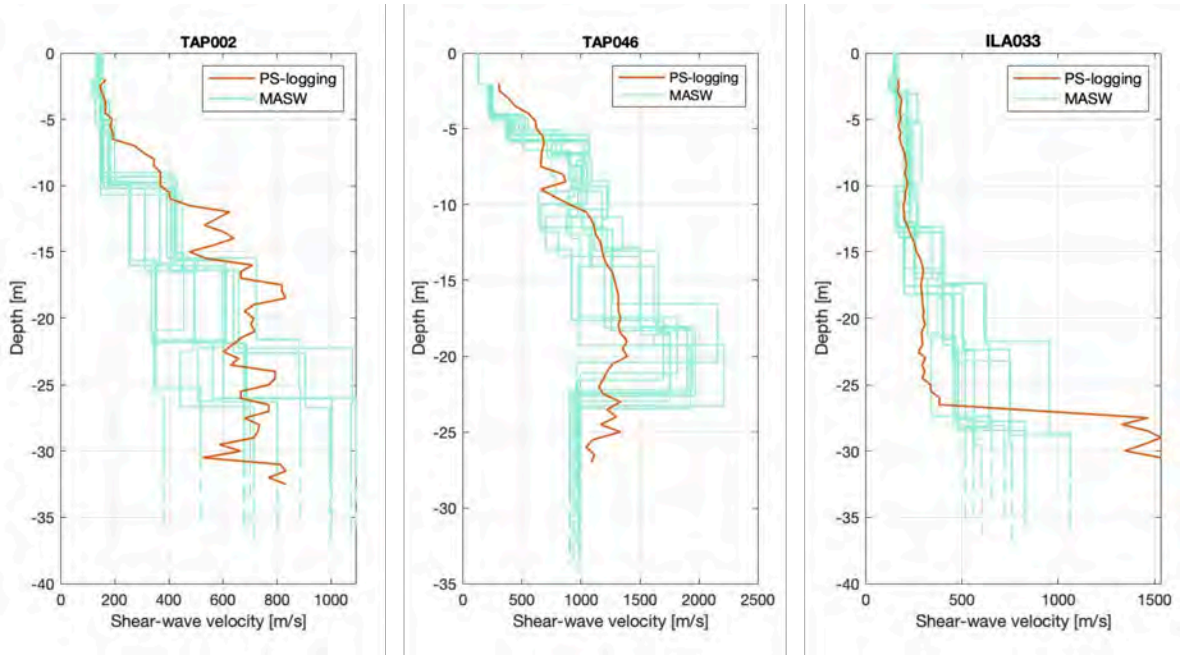

Figure 5.8 profiles selected with $MAPD < 3\%$ in the cases of TAP002, TAP046, and ILA033.

doi:10.6342/NTU202403310

In TAP046 and TAP054 (Figure 5.13 and 5.15), the experimental dispersion curves have similar behavior to the last scenario mentioned in Chapter 4.3. Therefore, it is inferred that the experimental dispersion curves may not always follow the fundamental mode. However, so far, there is no solid pattern to correct the dispersion curves, and the low-frequency components carry the information across the influenced range, making the specific information in the deep layer hard to be distinguished. As a consequence, if there is no obvious evidence of mode jump, the experimental dispersion curves in the following cases will be taken as the fundamental mode to conduct the inversion analysis.

The experimental dispersion curves displayed in the following are the data point within the reliable range corresponding to the receiver's ability and receiver spacing, and the drop segment in the low frequency and the discontinuous segment in high frequency will not be considered in the inversion analysis, as shown in Figure 5.9.

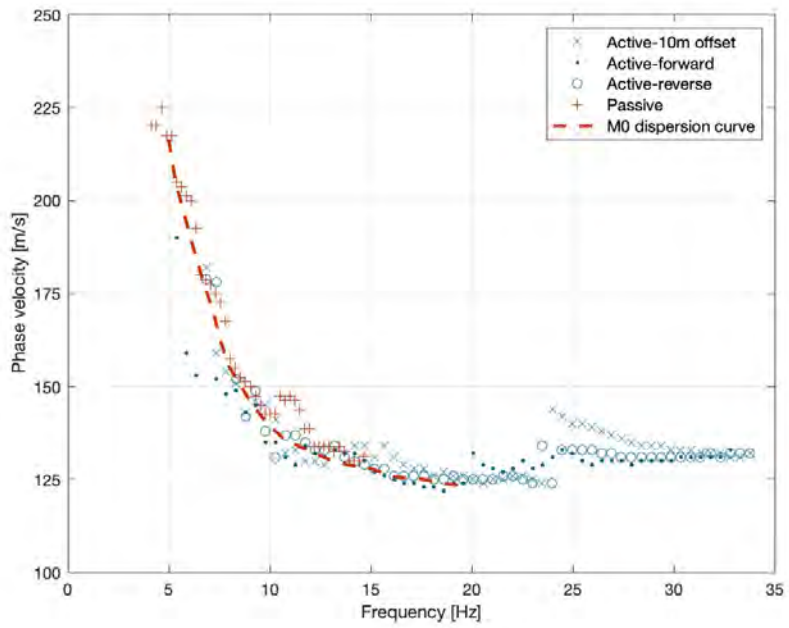

Figure 5.9 Illustration of the extracted experimental dispersion curve used in the inversion analysis.

doi:10.6342/NTU202403310

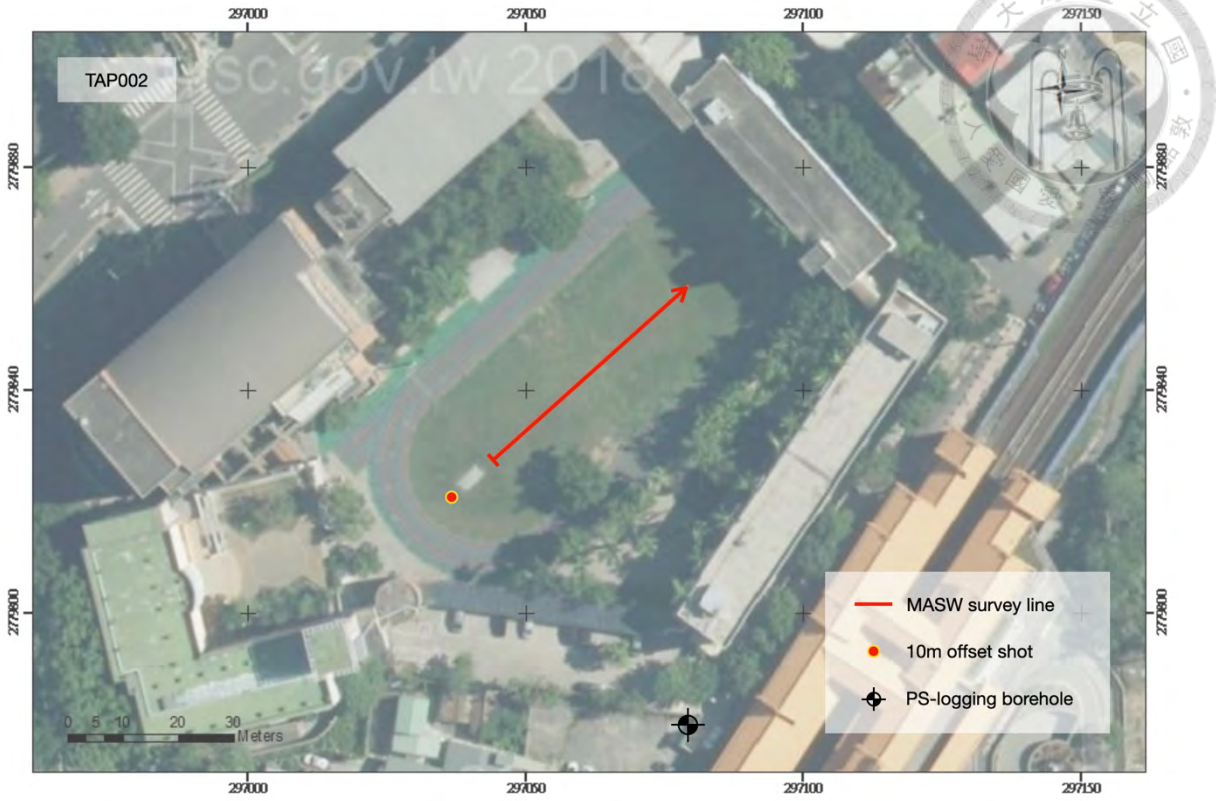

Figure 5.10 The distribution of survey lines and borehole of TAP002.

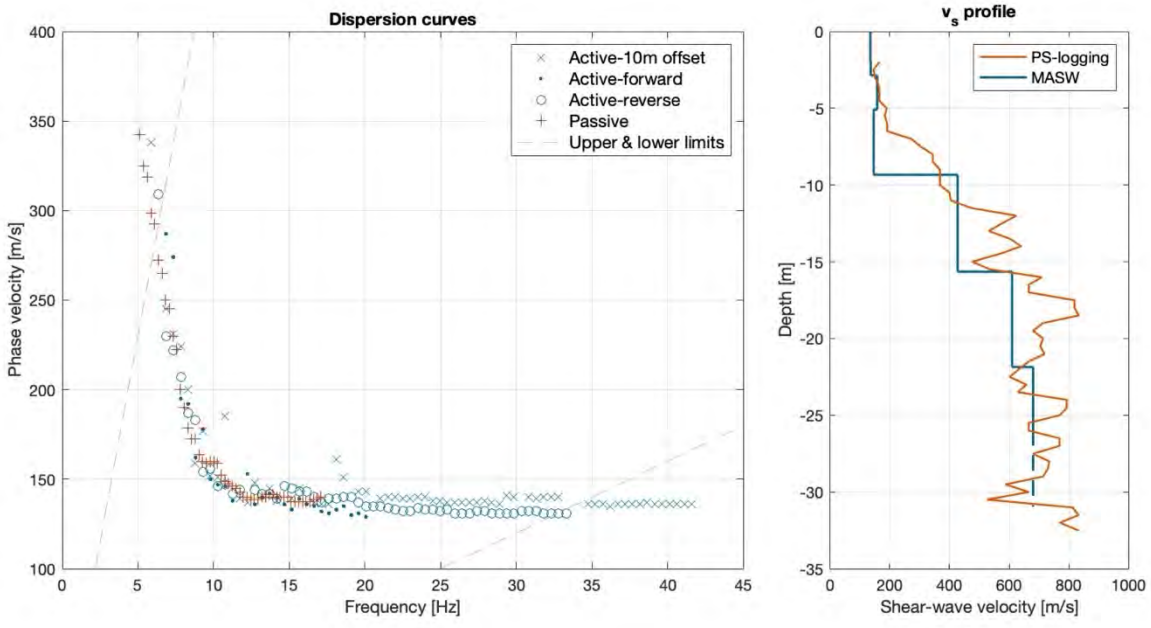

Figure 5.11 Dispersion curves and the final solution of MASW compared with the profile from PS-logging in TAP002, where the profile from MASW has $MAPD = 1.65\%$ and $RMSD = 4.72$ in inversion analysis.

doi:10.6342/NTU202403310

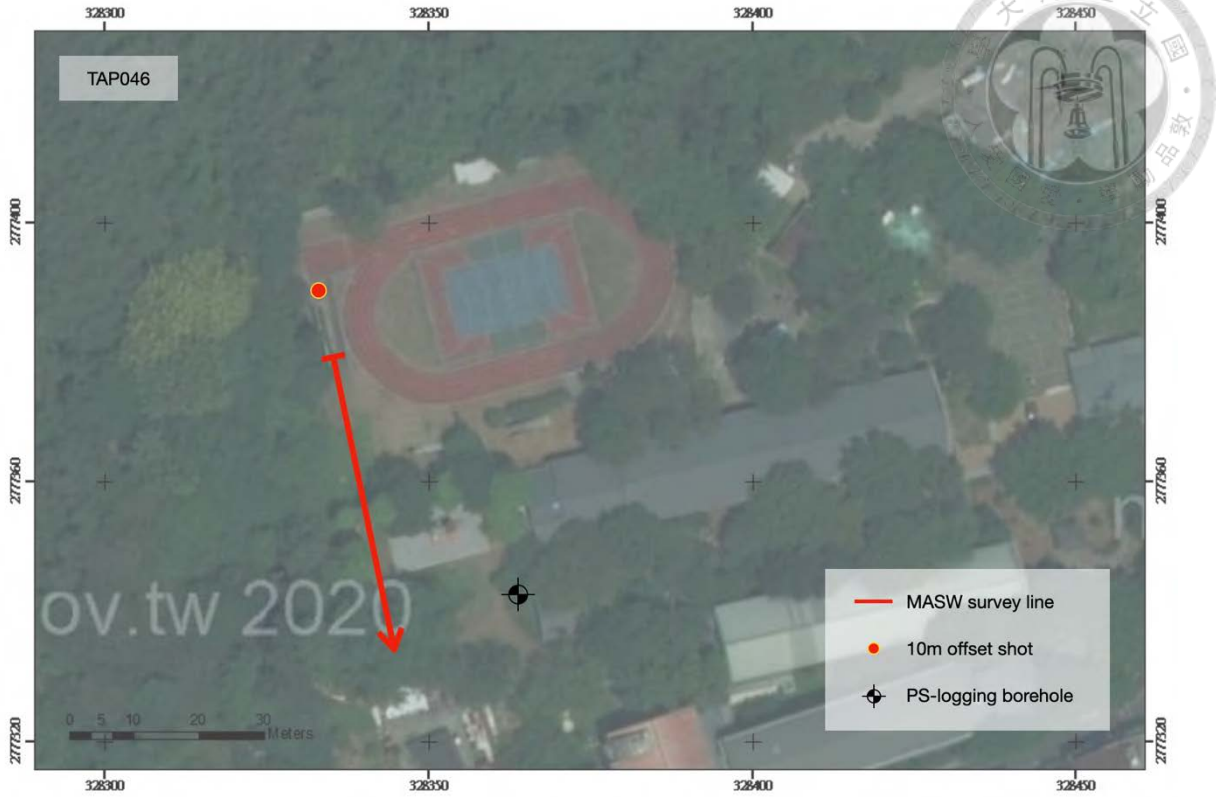

Figure 5.12 The distribution of survey lines and borehole of TAP046.

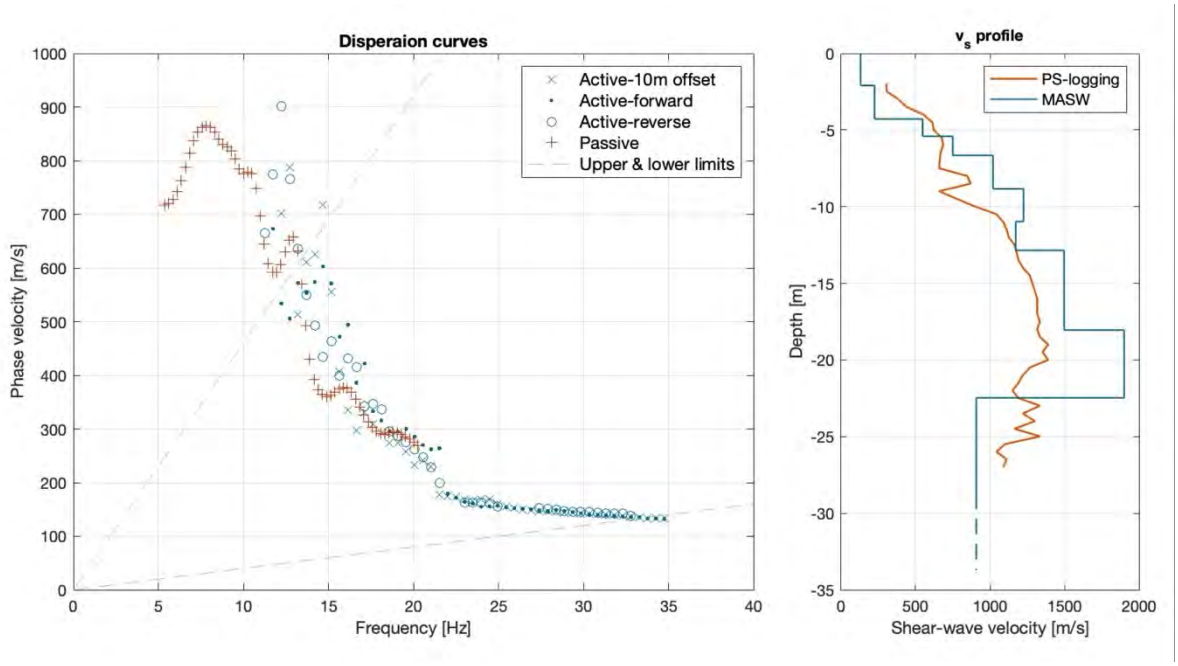

Figure 5.13 Dispersion curves and the final solution of MASW compared with the profile from PS-logging in TAP046, where the profile from MASW has $MAPD = 1.65\%$ and $RMSD = 4.72$ in inversion analysis.

doi:10.6342/NTU202403310

Figure 5.14 The distribution of survey lines and borehole of TAP054.

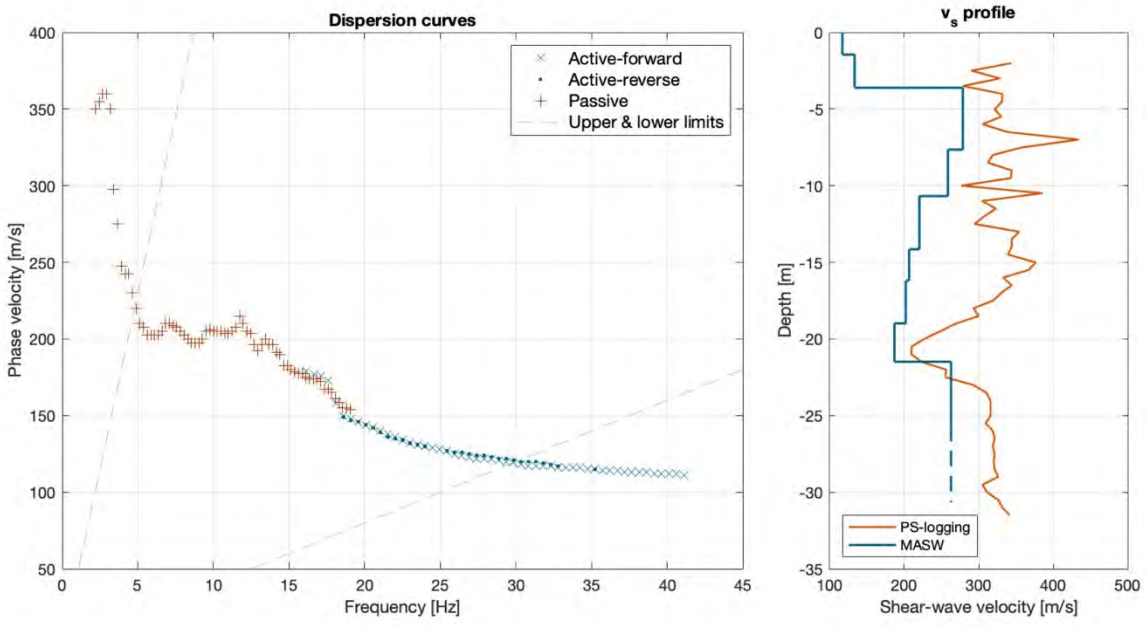

Figure 5.15 Dispersion curves and the final solution of MASW compared with the profile from PS-logging in TAP054, where the profile from MASW has $MAPD = 1.72\%$ and $RMSD = 4.22$ in inversion analysis.

doi:10.6342/NTU202403310

Figure 5.16 The distribution of survey lines and borehole of TCU081.

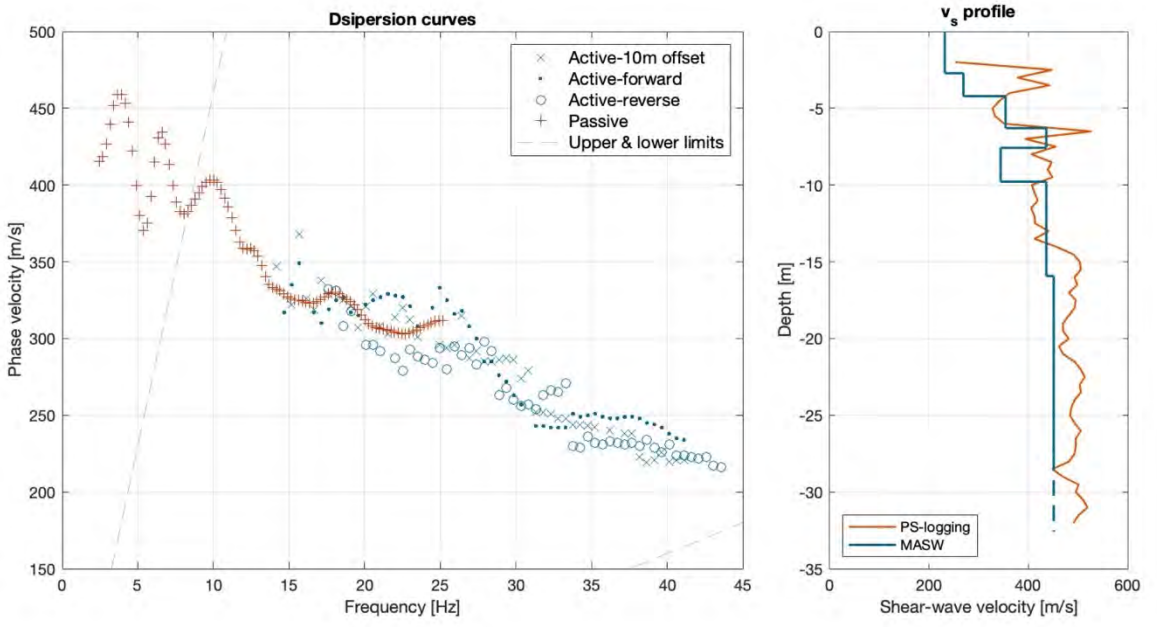

Figure 5.17 Dispersion curves and the final solution of MASW compared with the profile from PS-logging in TCU081, where the profile from MASW has $MAPD = 1.51\%$ and $RMSD = 6.0$ in inversion analysis.

doi:10.6342/NTU202403310

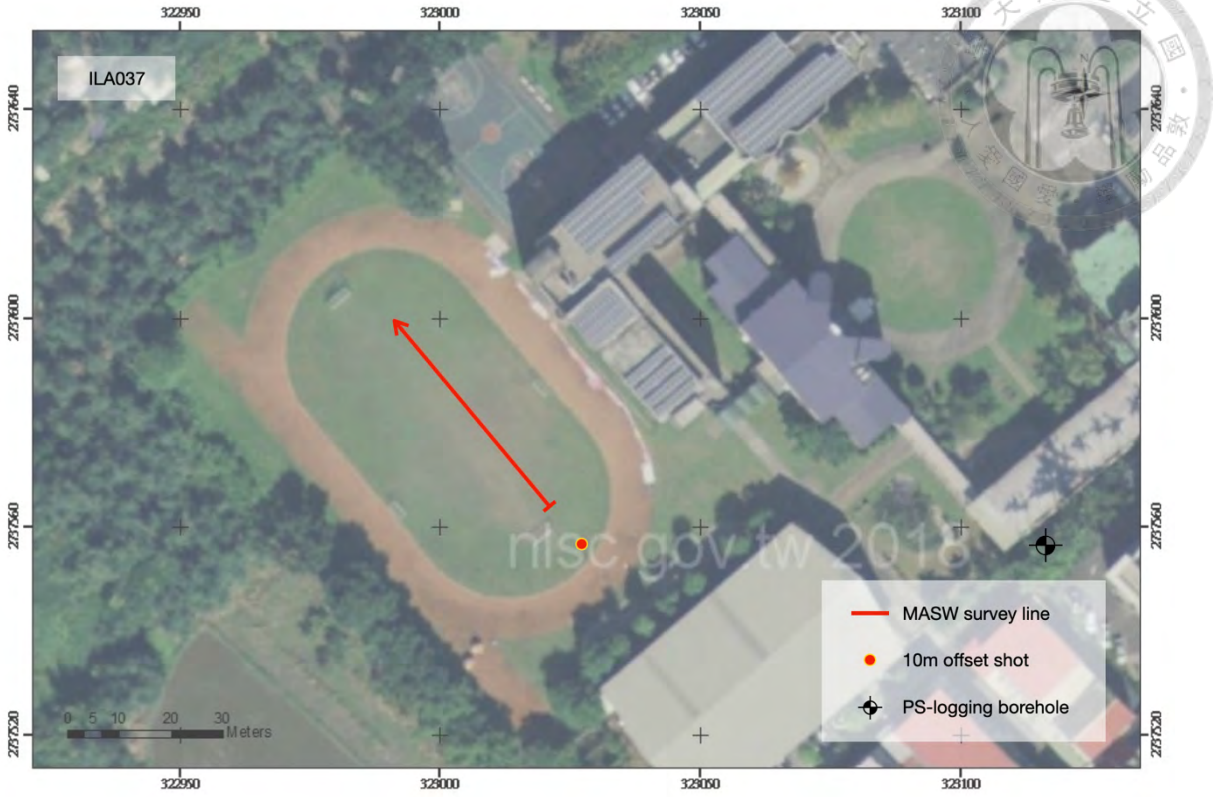

Figure 5.18 The distribution of survey lines and borehole of ILA037.

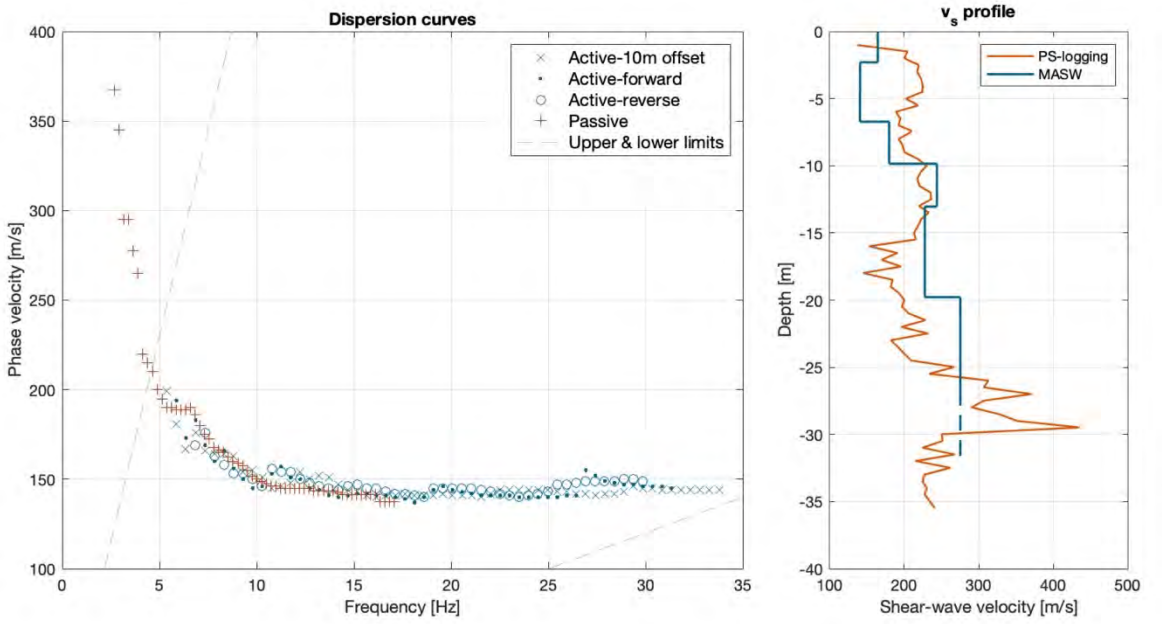

Figure 5.19 Dispersion curves and the final solution of MASW compared with the profile from PS-logging in ILA037, where the profile from MASW has $MAPD = 1.72\%$ and $RMSD = 5.35$ in inversion analysis.

doi:10.6342/NTU202403310

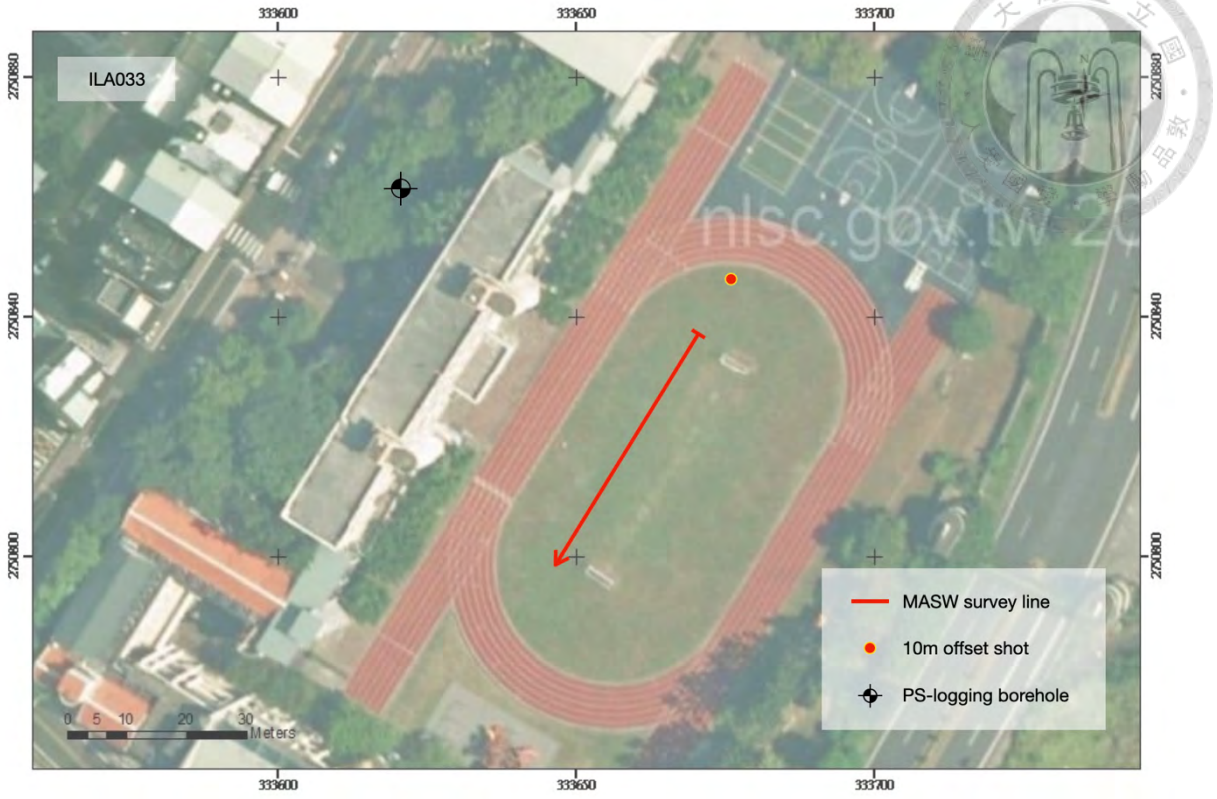

Figure 5.20 The distribution of survey lines and borehole of ILA033.

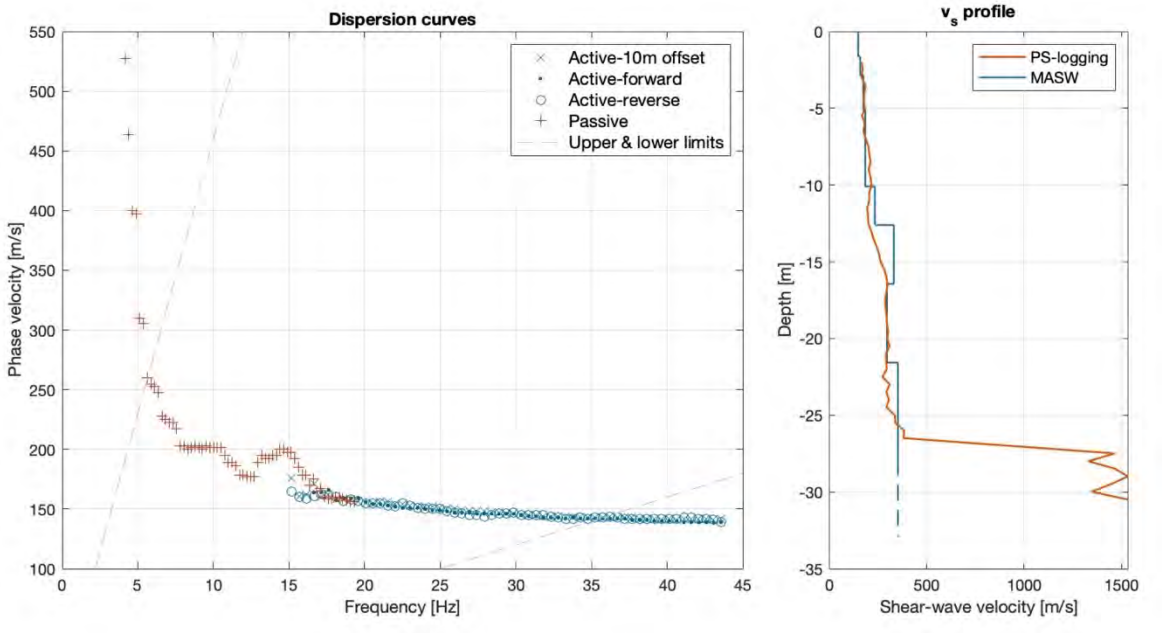

Figure 5.21 Dispersion curves and the final solution of MASW compared with the profile from PS-logging in ILA033, where the profile from MASW has $MAPD = 1.72\%$ and $RMSD = 6.87$ in inversion analysis.

doi:10.6342/NTU202403310

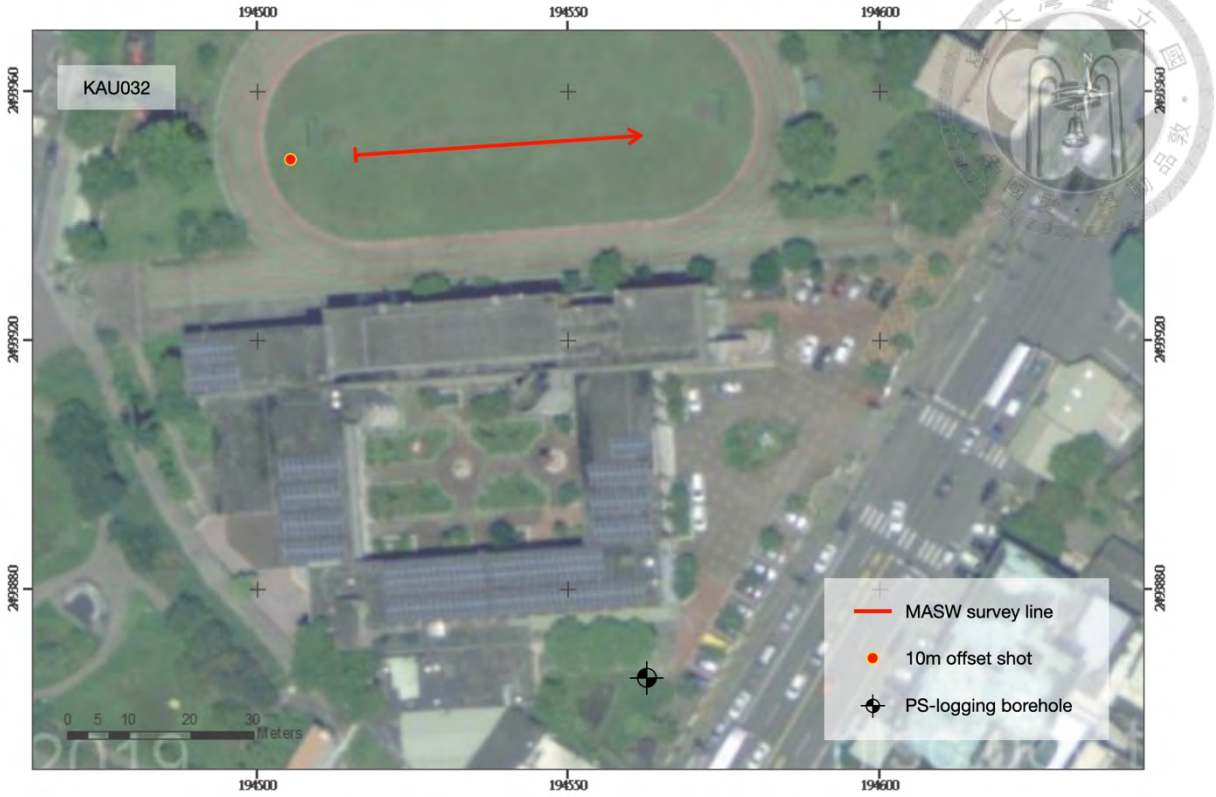

Figure 5.22 The distribution of survey lines and borehole of KAU032.

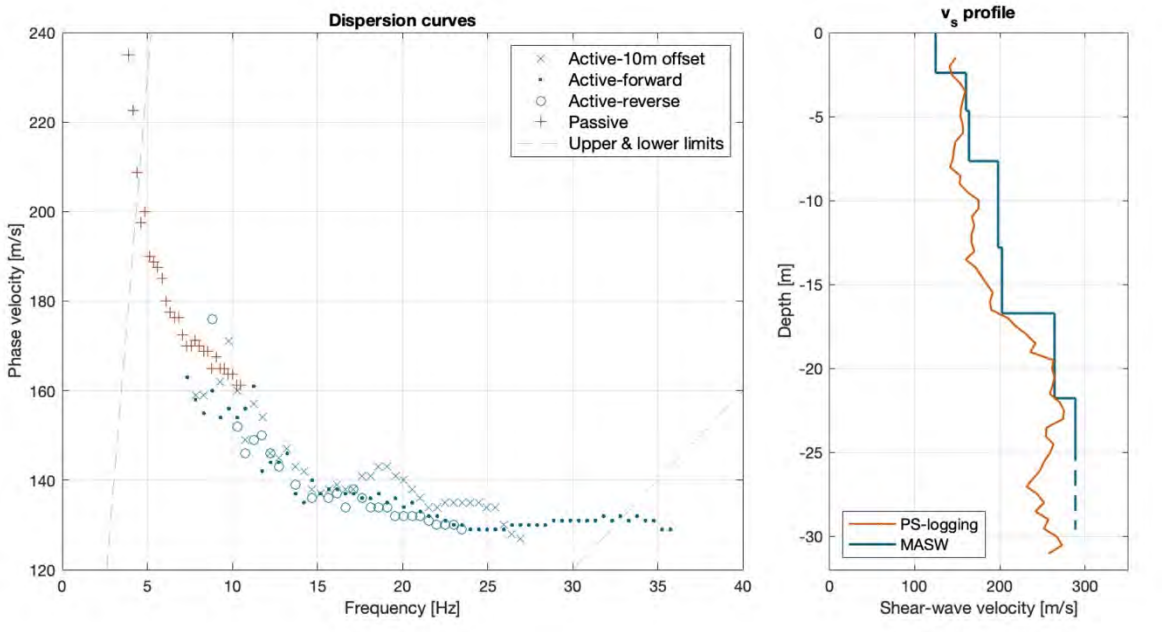

Figure 5.23 Dispersion curves and the final solution of MASW compared with the profile from PS-logging in KAU032, where the profile from MASW has $MAPD = 1.34\%$ and $RMSD = 2.10$ in inversion analysis.

doi:10.6342/NTU202403310

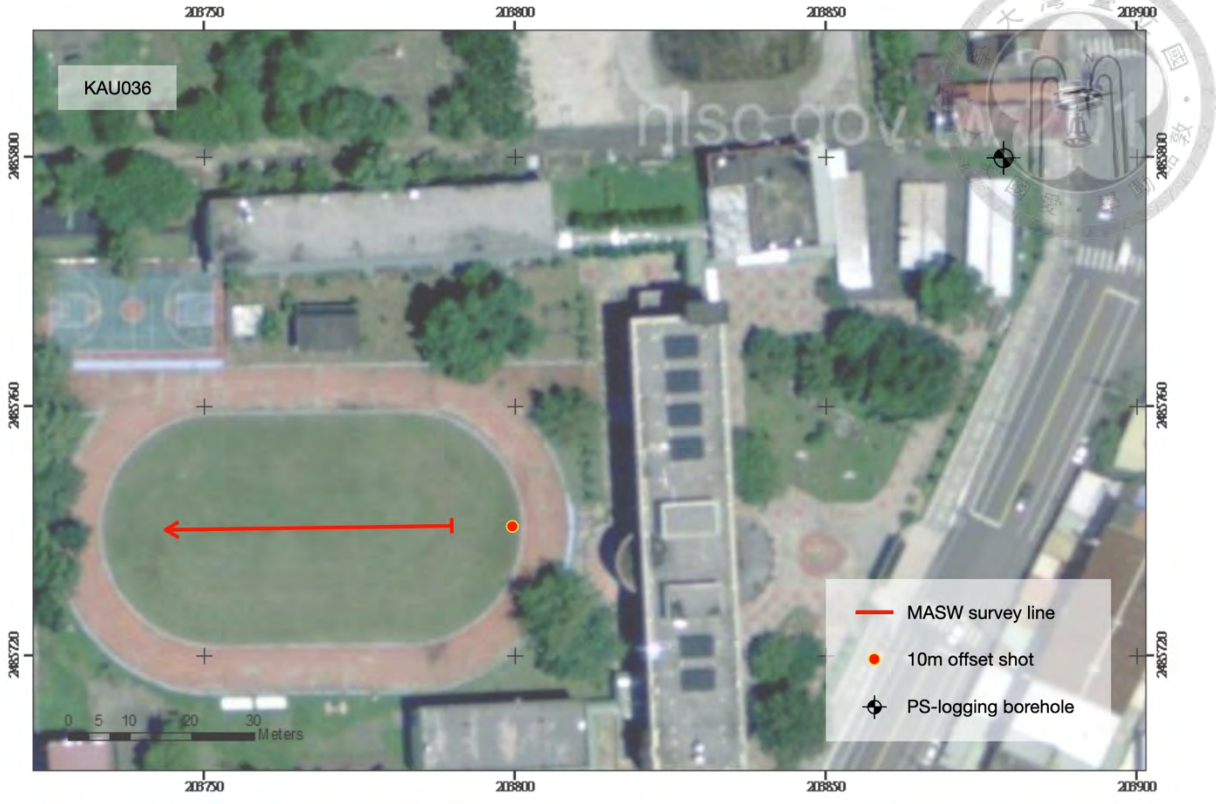

Figure 5.24 The distribution of survey lines and borehole of KAU036.

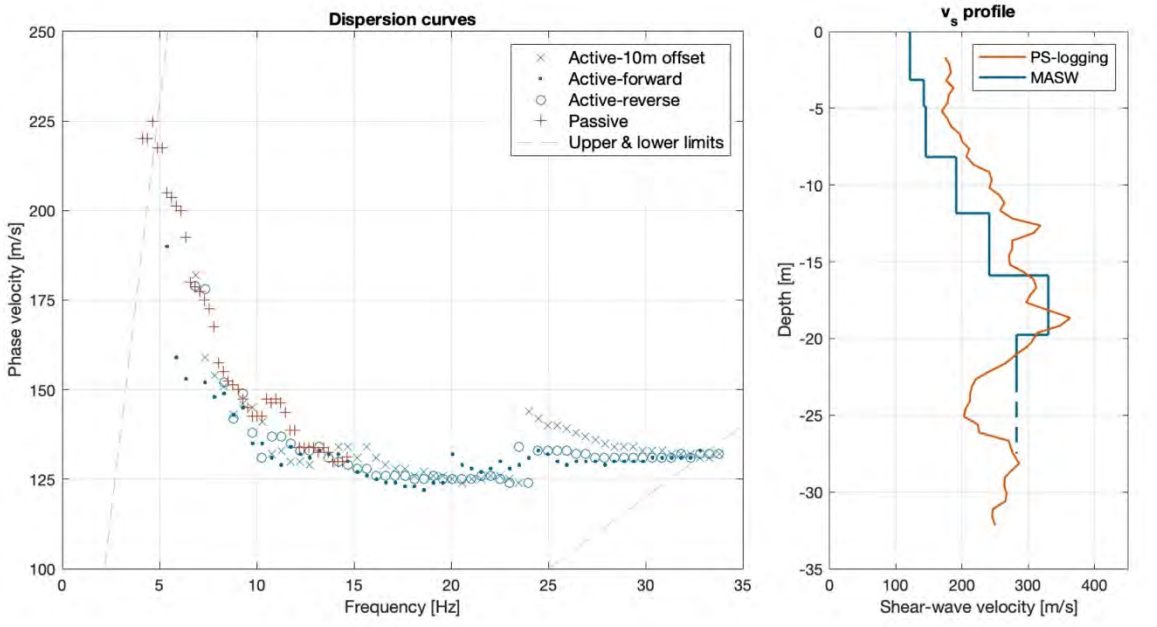

Figure 5.25 Dispersion curves and the final solution of MASW compared with the profile from PS-logging in KAU036, where the profile from MASW has $MAPD = 2.29\%$ and $RMSD = 3.54$ in inversion analysis.

doi:10.6342/NTU202403310

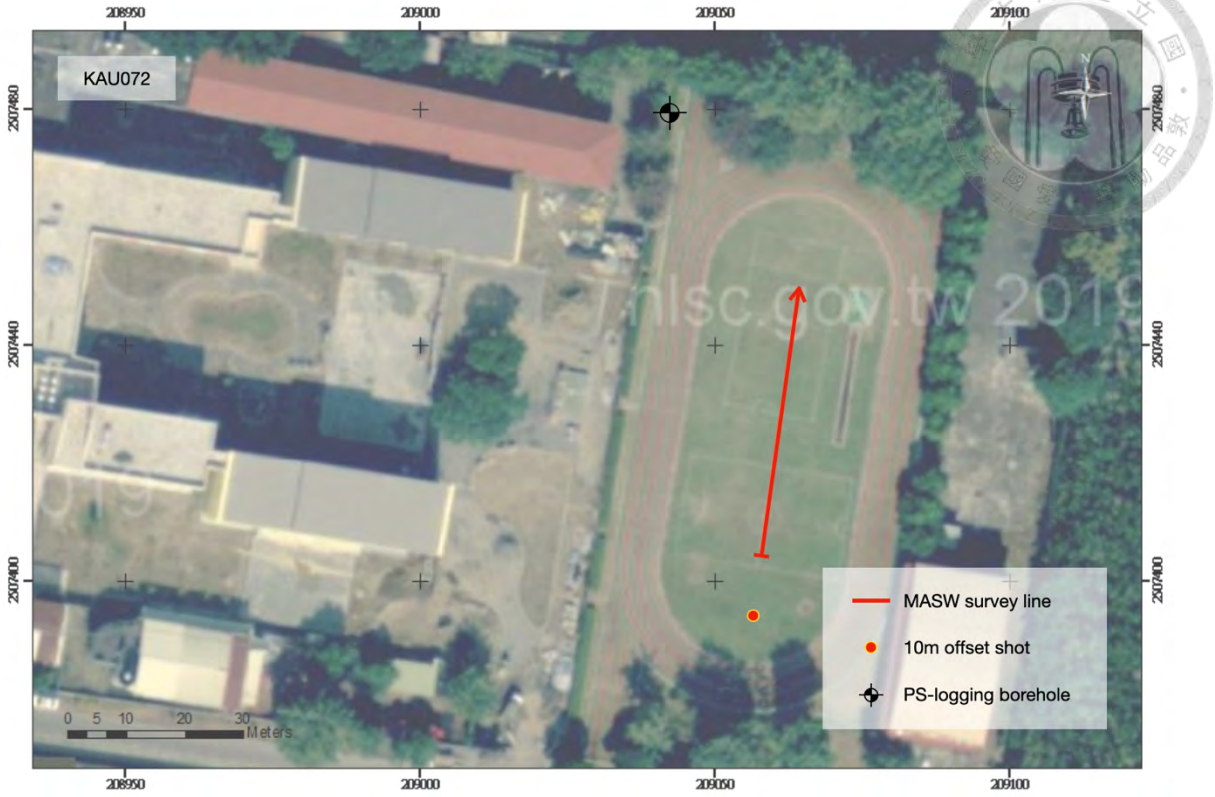

Figure 5.26 The distribution of survey lines and borehole of KAU072.

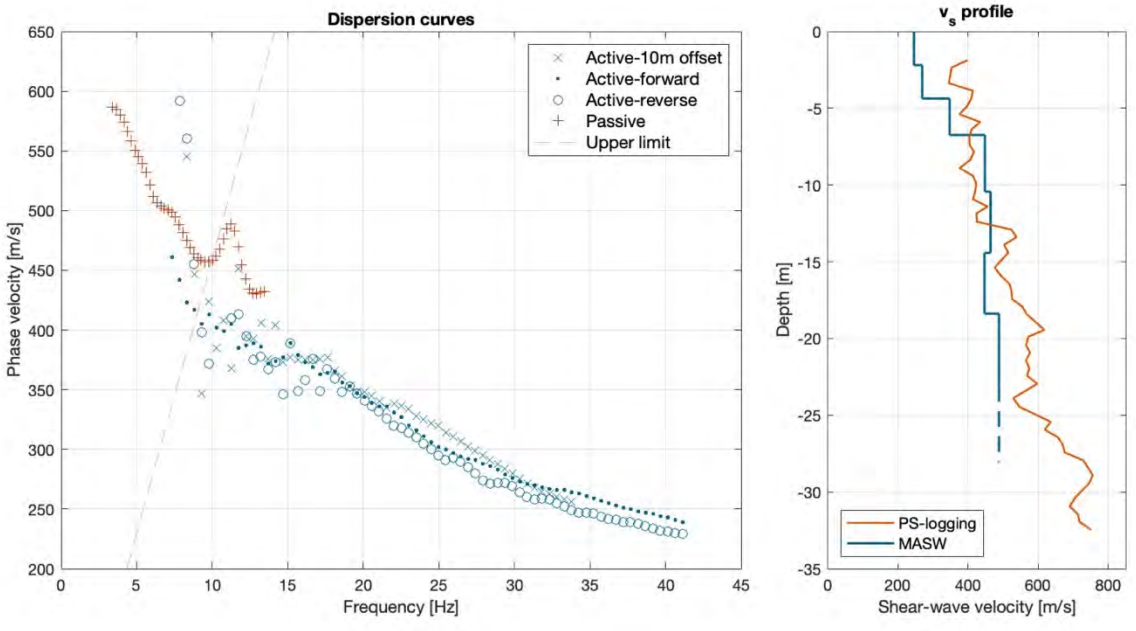

Figure 5.27 Dispersion curves and the final solution of MASW compared with the profile from PS-logging in KAU072, where the profile from MASW has $MAPD = 2.46\%$ and $RMSD = 10.39$ in inversion analysis.

doi:10.6342/NTU202403310

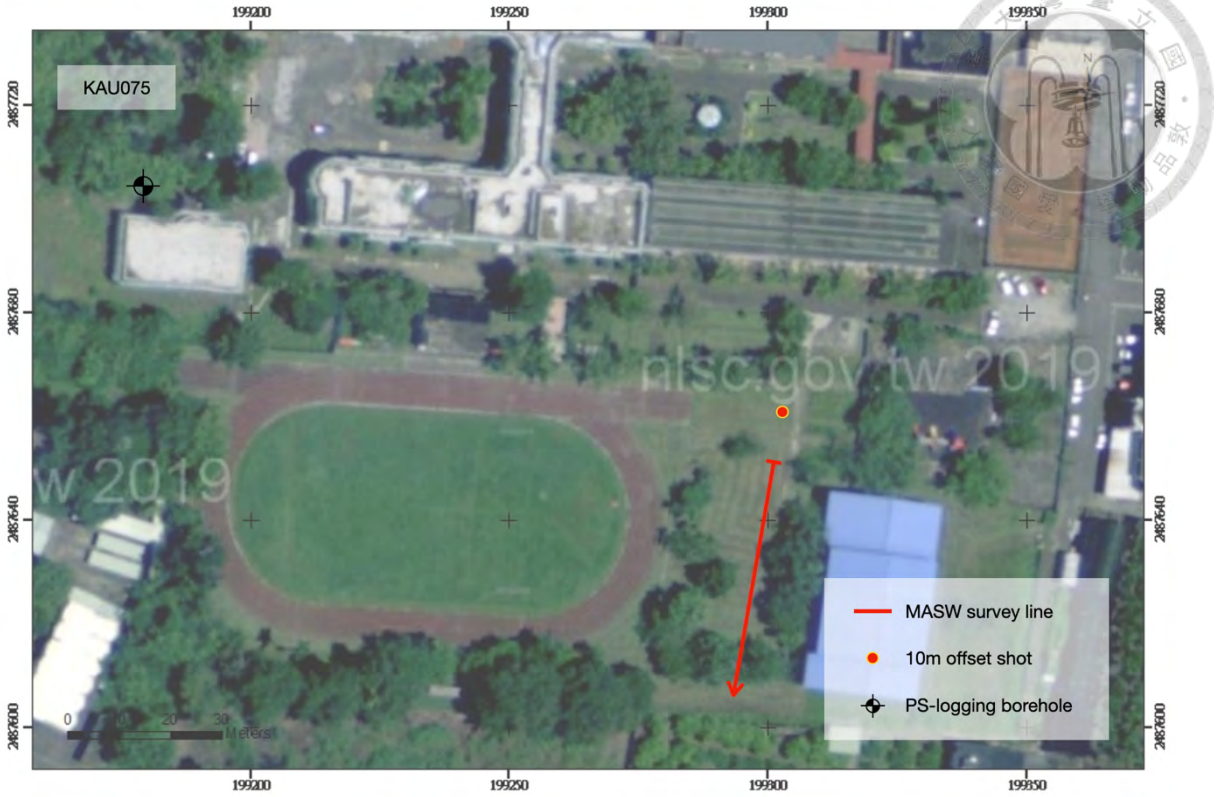

Figure 5.28 The distribution of survey lines and borehole of KAU075.

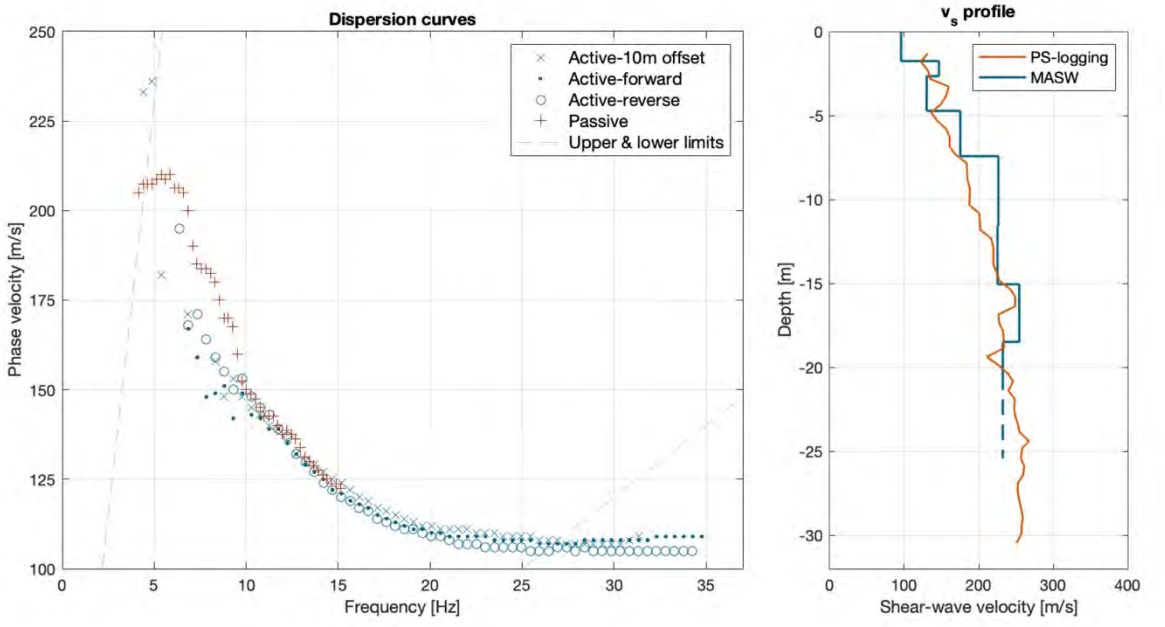

Figure 5.29 Dispersion curves and the final solution of MASW compared with the profile from PS-logging in KAU075, where the profile from MASW has $MAPD = 2.24\%$ and $RMSD = 4.03$ in inversion analysis.

doi:10.6342/NTU202403310

5.3 Comparison in $v_{s,30}$

Ten adequate profiles are selected in each case, and the average of $v_{s,30}$ estimated by each profile is compared with the $v_{s,30}$ estimated by PS-logging. The result is shown in Figure 5.21. It seems that MASW tends to give a lower value of $v_{s,30}$ compared to the value given by PS-logging, but overall, the MASW can give a reasonable result from the perspective of site classification. The underestimation in TAP002 and TAP046 may be due to the loss of accuracy in the deep layer. In contrast, the sites with shear wave velocity increasing gently with deep show a good agreement in estimating $v_{s,30}$ by MASW and PS-logging.

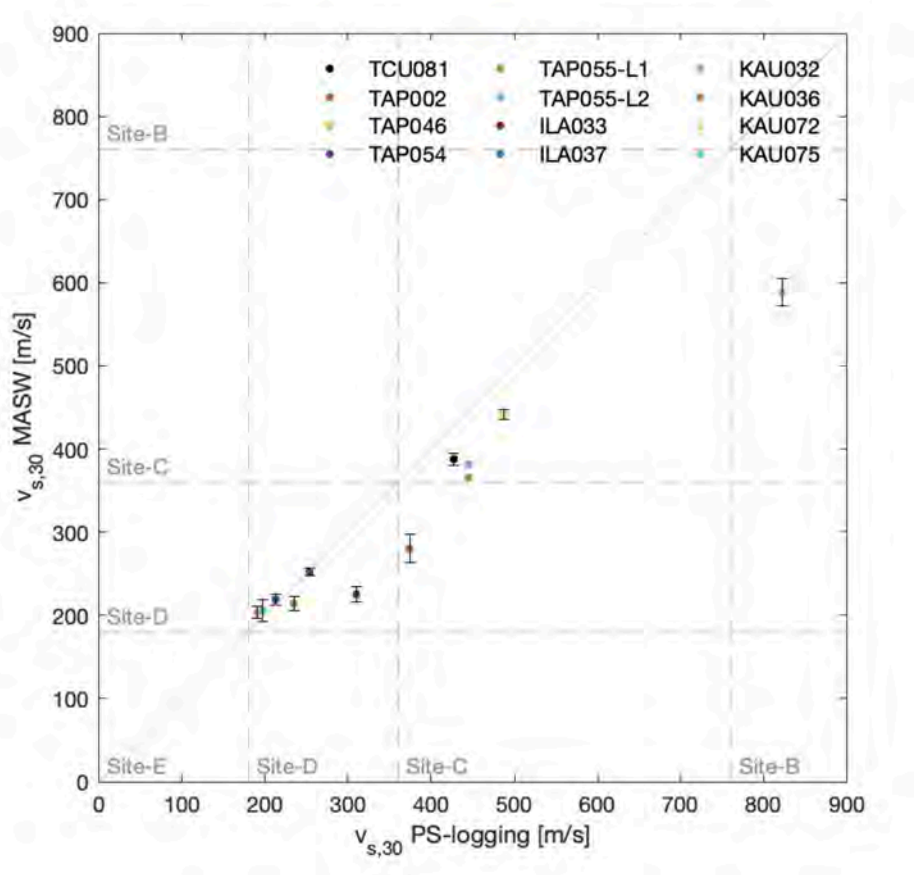

Figure 5.30 Comparison of $v_{s,30}$ estimated by MASW and PS-logging.

doi:10.6342/NTU202403310

5.4 Shear wave velocity profiles for non-investigated sites

The results of the MASW field test conducted in sites without previous investigation data are presented in the following figures. Figure 5.23 illustrates a comparison between the $v_{s,30}$ values estimated by MASW and the predicted values of $v_{s,30}$. It appears that MASW tends to underestimate the $v_{s,30}$ values.

A review was conducted to further assess the results by comparing them with the nearest stations with existing data. The site classifications, according to MASW, align with those of the nearest stations, except TAP125. In the case of TAP125, despite the $v_{s,30}$ value being affected by the shallow layer that reduces its magnitude, MASW still manages to detect the existence of a stiff layer located below 15m from the ground surface. The overall trend observed in TAP125 aligns with the profile of the nearest station, TAP057, as shown in Figure 5.24.

Moreover, there are specific instances that support the reliability of the results obtained from MASW. For example, in the case of ILA022, the closest station with existing data is ILA018. The $v_{s,30}$ value estimated by MASW in ILA022 is $474.17\ m/s$, which closely matches the $v_{s,30}$ value of $497.47\ m/s$ estimated by PS-logging in ILA018. Similar circumstances are observed in ILA060 and ILA007, where the $v_{s,30}$ values estimated by MASW in ILA060 ($413.25\ m/s$) and ILA007 ($432.35\ m/s$), respectively, are in close agreement with the values estimated by PS-logging in the nearest stations. These findings partially support the reliability of the results generated by MASW (Figure 5.24). Besides, it is observed that the MASW performs well in the Lanyang Plain.

doi:10.6342/NTU202403310

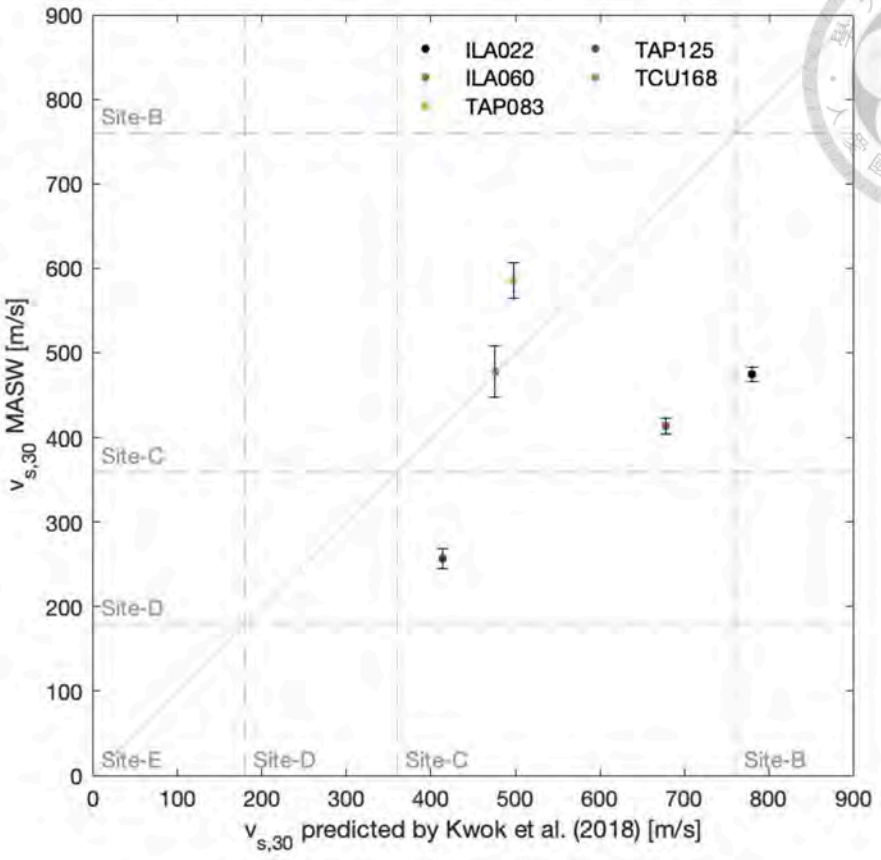

Figure 5.31 Comparison of $v_{s,30}$ estimated by MASW and the value predicted by Kwok et al. (2018).

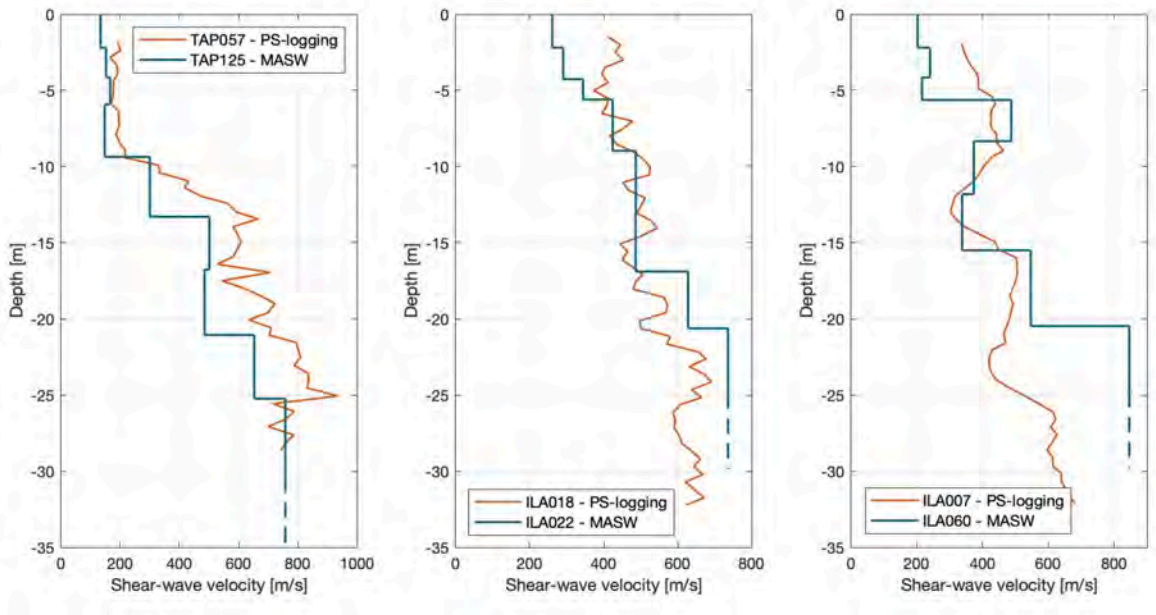

Figure 5.32 Comparison with the profiles in the nearest stations with existing data.

doi:10.6342/NTU202403310

Figure 5.33 The distribution of survey lines in ILA022.

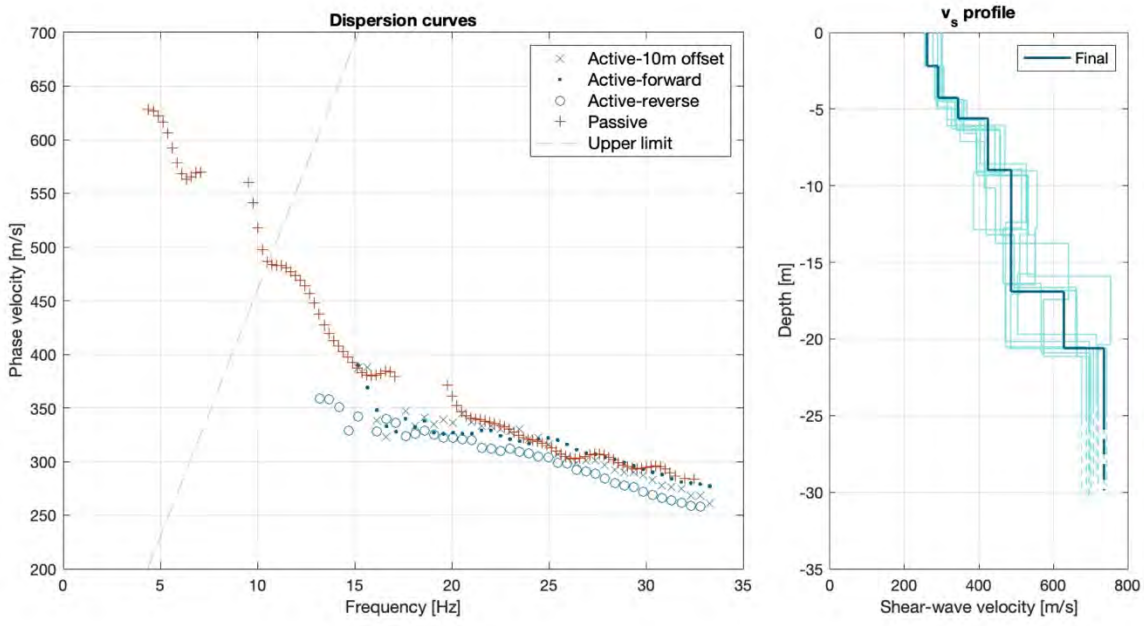

Figure 5.34 Dispersion curves and the final solution of MASW in ILA022, where the final profile from MASW has $MAPD = 2.37\%$ and $RMSD = 13.38$ in inversion analysis.

doi:10.6342/NTU202403310

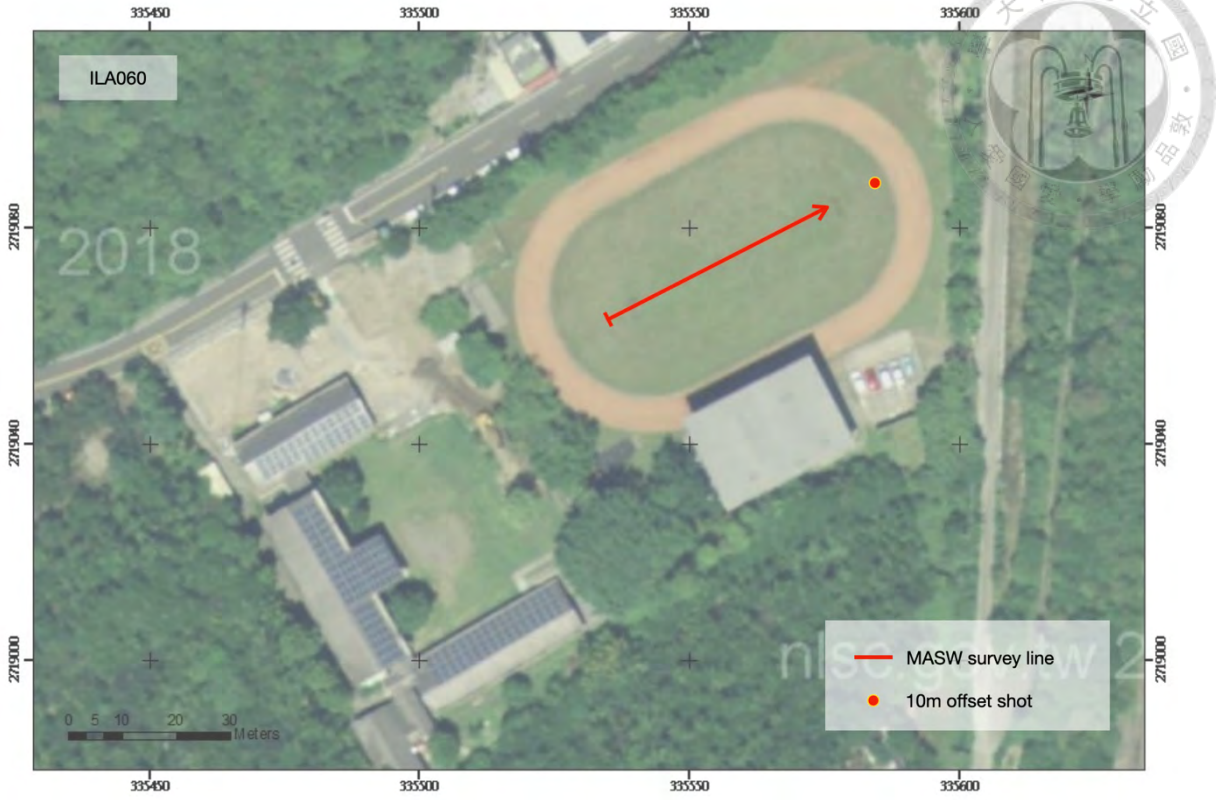

Figure 5.35 The distribution of survey lines in ILA060.

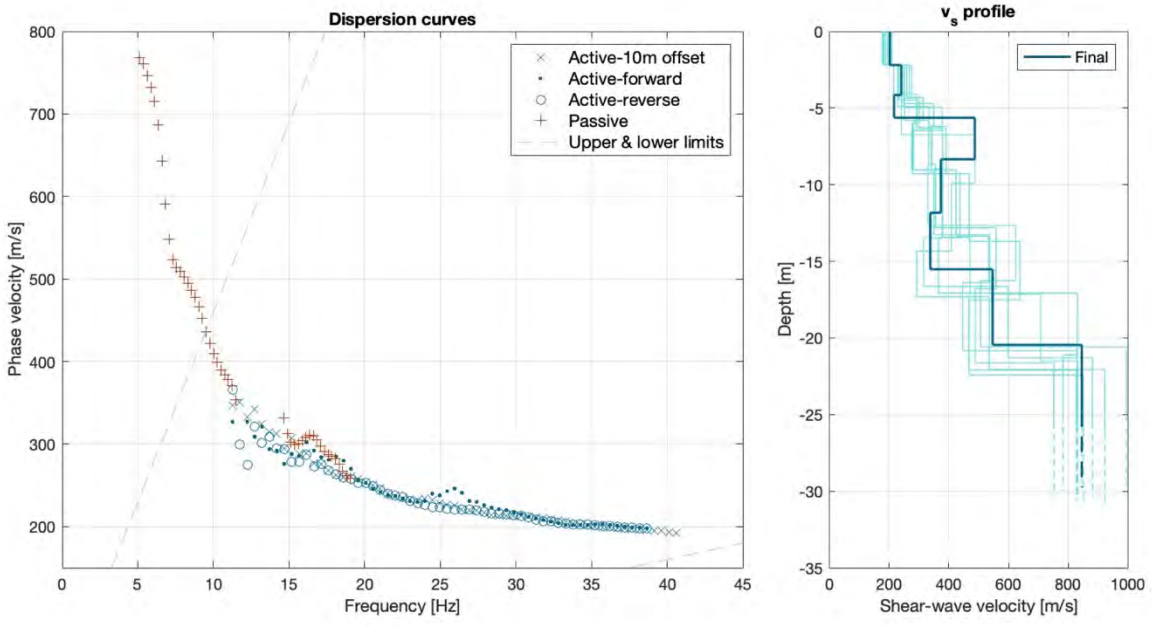

Figure 5.36 Dispersion curves and the final solution of MASW in ILA060, where the final profile from MASW has $MAPD = 2.24\%$ and $RMSD = 12.79$ in inversion analysis.

doi:10.6342/NTU202403310

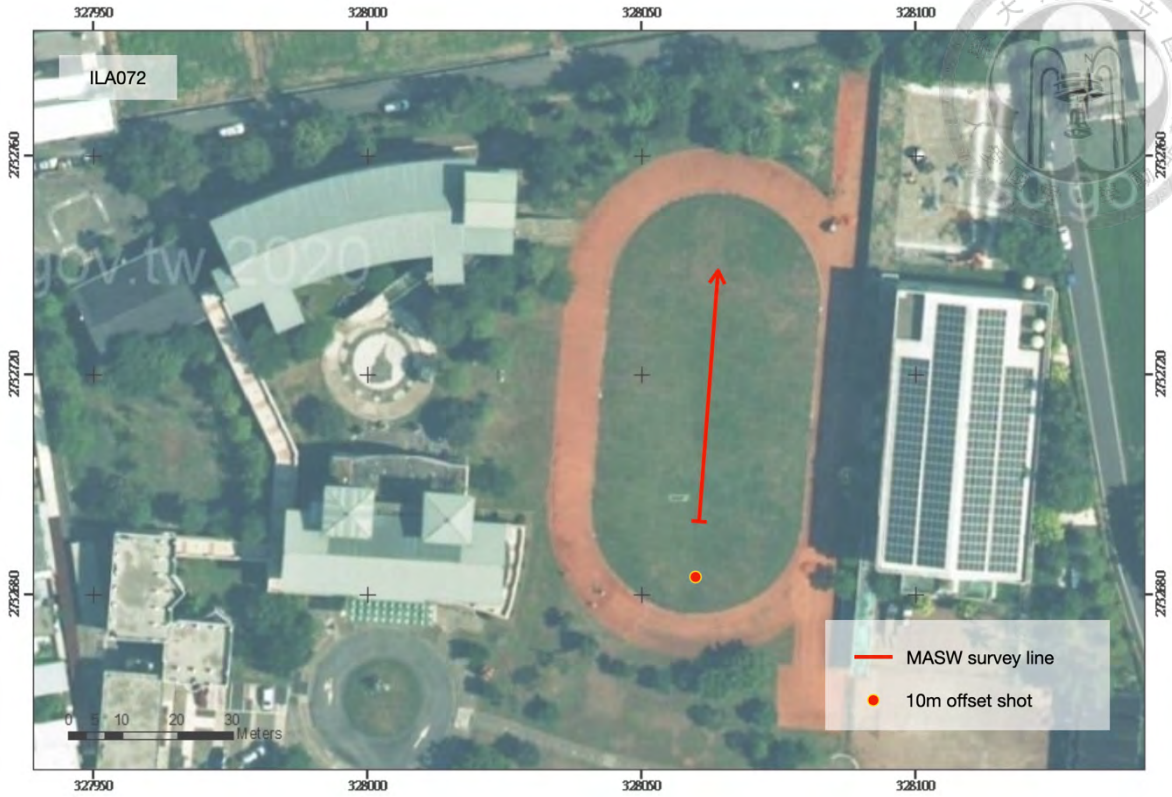

Figure 5.37 The distribution of survey lines in ILA072.

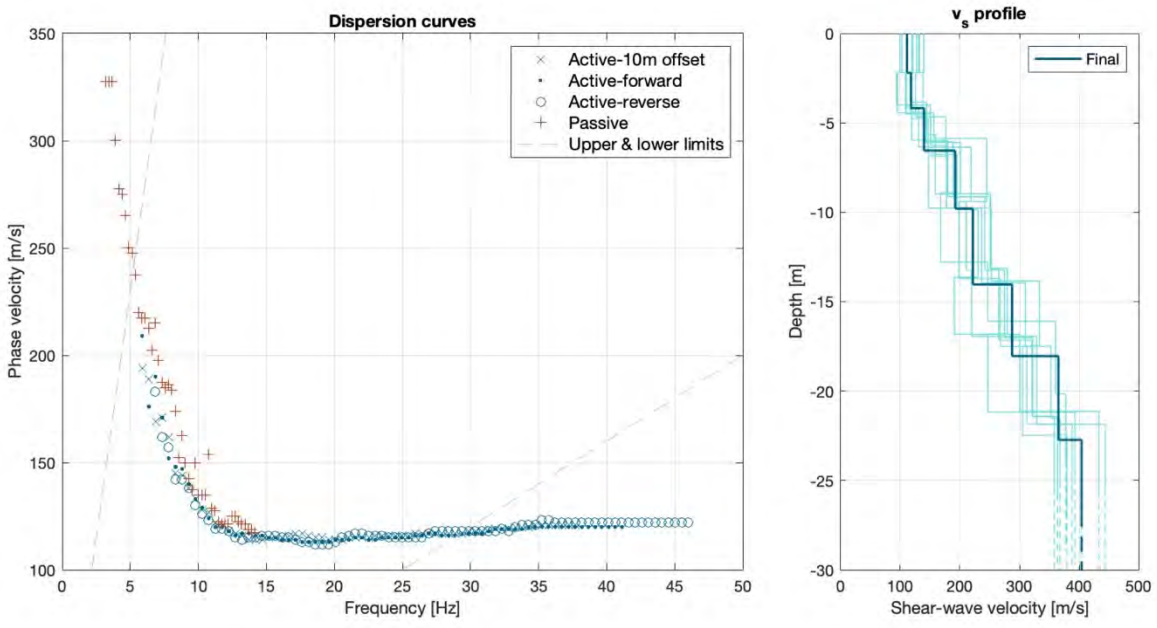

Figure 5.38 Dispersion curves and the final solution of MASW in ILA072, where the final profile from MASW has $MAPD = 2.46\%$ and $RMSD = 7.24$ in inversion analysis.

doi:10.6342/NTU202403310

Figure 5.39 The distribution of survey lines in TAP083.

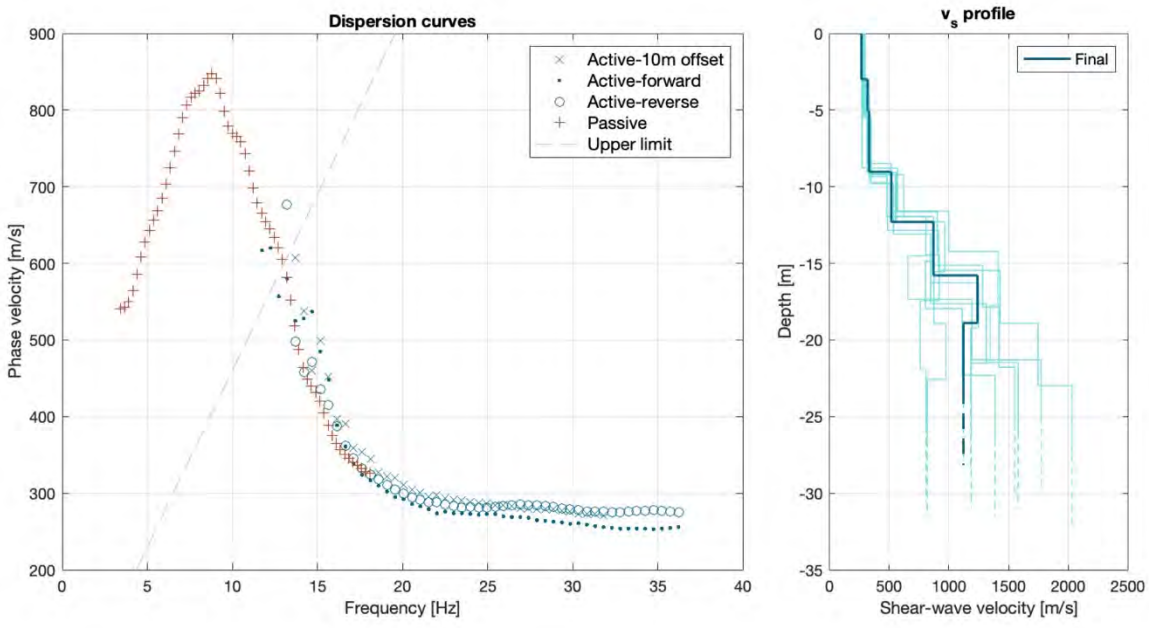

Figure 5.40 Dispersion curves and the final solution of MASW in TAP083, where the final profile from MASW has $MAPD = 2.12\%$ and $RMSD = 9.39$ in inversion analysis.

doi:10.6342/NTU202403310

Figure 5.41 The distribution of survey lines in TAP125.

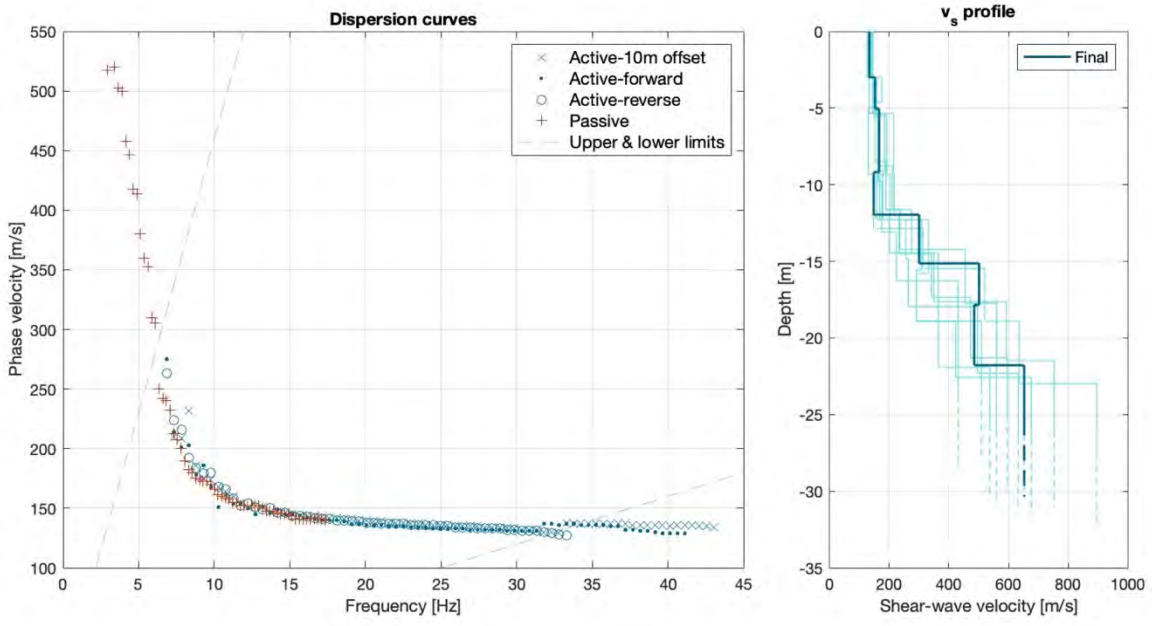

Figure 5.42 Dispersion curves and the final solution of MASW in TAP125, where the final profile from MASW has $MAPD = 2.32\%$ and $RMSD = 9.39$ in inversion analysis.

doi:10.6342/NTU202403310

Figure 5.43 The distribution of survey lines in TCU168.

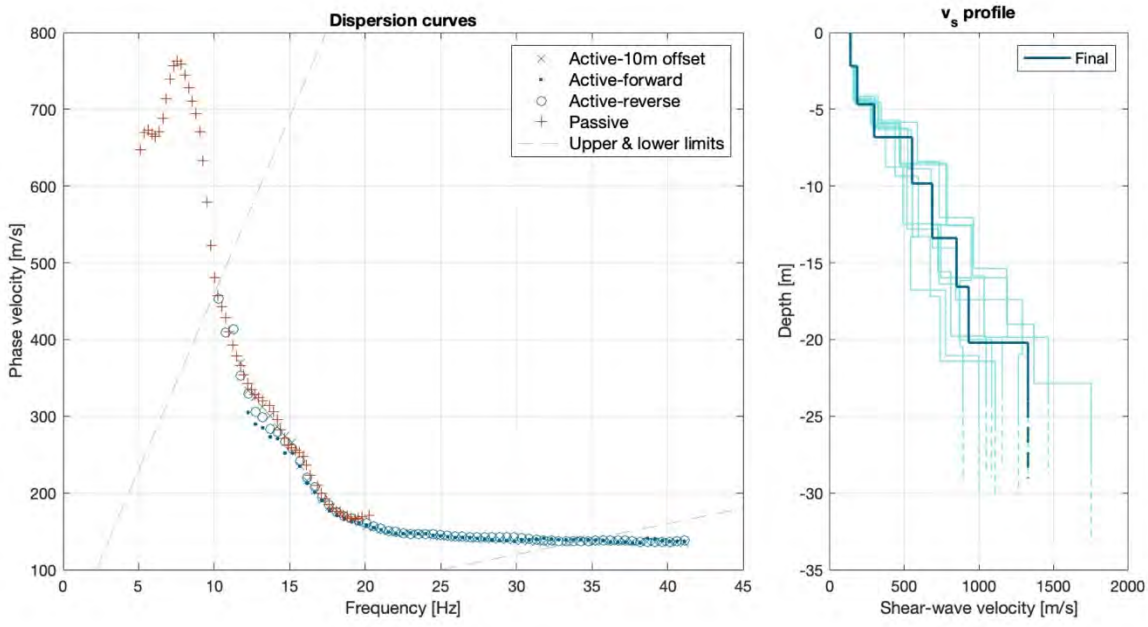

Figure 5.44 Dispersion curves and the final solution of MASW in TCU168, where the final profile from MASW has $MAPD = 2.46\%$ and $RMSD = 21.17$ in inversion analysis.

doi:10.6342/NTU202403310

Chapter 6 Conclusion

1. From the perspective of the behavior of the experimental dispersion curve, three statements can be concluded: firstly, the severe change within the investigation depth may increase the inaccuracy in the deep layer. Secondly, the shear wave velocity decreases with depth in the shallow layer may lead to the higher mode dominating the high-frequency band of the experimental dispersion curve. Lastly, the shear wave velocity decreases with depth in the deep layer may disturb the low-frequency band of the experimental dispersion curve.
2. In the inversion analysis, the accuracy will not increase consistently with increasing the layers in the assumed profile.
3. In the survey line with 46m in length and 2m receiver spacing, the data gathered from 10m offset and 5m offset shows no significant difference in the calculation of the experimental dispersion curve.
4. Considering only the experimental dispersion curves, the MASW active test can generate a stable and consistent result. Consequently, the uncertainty in the shear wave velocity profile may mainly come from the inversion analysis.
5. Compared with the $v_{s,30}$ estimated by PS-logging, MASW appears to underestimate the $v_{s,30}$, but it can still give a reasonable site classification in most cases.
6. From the field test results, the MASW performs well in the area of the alluvial plane compared with the available data. The MASW can certainly be an alternative to the invasive method in the alluvial plane.

doi:10.6342/NTU202403310

Reference

[1] Abo-Zena, A. (1979). Dispersion function computations for unlimited frequency values. *Geophysical Journal International*, *58*(1), 91-105.

[2] Aki, K. (1957). Space and time spectra of stationary stochastic waves, with special reference to microtremors. *Bulletin of the Earthquake Research Institute*, *35*, 415-456.

[3] Beaty, K. S., Schmitt, D. R., & Sacchi, M. (2002). Simulated annealing inversion of multimode Rayleigh wave dispersion curves for geological structure. *Geophysical Journal International*, *151*(2), 622-631.

[4] Bolt, B. A. (1993). *Earthquakes and geological discovery.* Scientific American Library.

[5] Bullen, K. E., Bullen, K. A., & Bolt, B. A. (1985). *An introduction to the theory of seismology*. Cambridge university press.

[6] Comina, C., Foti, S., Boiero, D., & Socco, L. (2011). Reliability of Vs,30 evaluation from surface-wave tests. *Journal of Geotechnical and Geoenvironmental engineering*, *137*(6), 579-586.

[7] EPRI. (1993). *Guidelines for Determining Design Basis Ground Motions Volume 1: Method and Guidelines for Estimating Earthquake Ground Motion in Eastern North America* (TR-102293).

[8] Foti, S., Comina, C., Boiero, D., & Socco, L. (2009). Non-uniqueness in surface-wave inversion and consequences on seismic site response analyses. *Soil Dynamics and Earthquake Engineering*, *29*(6), 982-993.

[9] Foti, S., Hollender, F., Garofalo, F., Albarello, D., Asten, M., Bard, P.-Y., Comina, C., Cornou, C., Cox, B., & Di Giulio, G. (2018). Guidelines for the good practice of surface wave analysis: a product of the InterPACIFIC project. *Bulletin of Earthquake*

doi:10.6342/NTU202403310

Engineering, *16*, 2367-2420.

[10] Geometrics, I. (2006). *SeisImager/SW Manual Windows Software for Analysis of Surface Waves*. Geometrics, Inc.

[11] Haskell, N. A. (1953). The dispersion of surface waves on multilayered media. *Bulletin of the seismological Society of America*, *43*(1), 17-34.

[12] Hayashi, K., & Suzuki, H. (2004). CMP cross-correlation analysis of multi-channel surface-wave data. *Exploration Geophysics*, *35*(1), 7-13.

[13] Heisey, J., Stokoe, K., & Meyer, A. (1982). Moduli of pavement systems from spectral analysis of surface waves. *Transportation research record*, *852*(22-31), 147.

[14] Itasca. (2011). *FLAC — Fast Lagrangian Analysis of Continua, Ver. 7.00. User's Manual*. Itasca Consulting Group, Inc.

[15] Kausel, E., & Roësset, J. M. (1981). Stiffness matrices for layered soils. *Bulletin of the seismological Society of America*, *71*(6), 1743-1761.

[16] Kramer, S. L. (1996). *Geotechnical earthquake engineering*. Prentice Hall.

[17] Kuhlemeyer, R. L., & Lysmer, J. (1973). Finite element method accuracy for wave propagation problems. *Journal of the Soil Mechanics and Foundations Division*, *99*(5), 421-427.

[18] Kwok, O. L. A., Stewart, J. P., Kwak, D. Y., & Sun, P.-L. (2018). Taiwan-specific model for V s30 prediction considering between-proxy correlations. *Earthquake Spectra*, *34*(4), 1973-1993.

[19] Lin, C.-P., Putri, A. S., Wu, T.-J., & Pan, E. (2021). Behavior of apparent dispersion curve and its implications to MASW testing. *J. GeoEng.*, *16*, 121-131.

[20] Lysmer, J., & Kuhlemeyer, R. L. (1969). Finite dynamic model for infinite media.

doi:10.6342/NTU202403310

Journal of the engineering mechanics division, *95*(4), 859-877.

[21] Menke, W. (1979). Comment on 'Dispersion function computations for unlimited frequency values' by Anas Abo-Zena. *Geophysical Journal International*, *59*(2), 315-323.

[22] Miller, C. A., Costantino, C. J., Pires, I. A., & Higgins, C. J. (2001). *Evaluation of the Hualien Quarter Scale Model Seismic Experiment: Geotechnical Site Characterization Review (NUREG/CR-6584, Volume 2)*.

[23] NCREE. (2009). *Engineering Geological Database for TSMIP (EGDT)* https://egdt.ncree.org.tw/overview_eng.htm

[24] Okada, H., & Suto, K. (2003). *The microtremor survey method*. Society of Exploration Geophysicists.

[25] Olafsdottir, E. (2014). Multichannel analysis of surface waves methods for dispersion analysis of surface wave data. *University of Iceland, Reykjavik, Iceland*.

[26] Olafsdottir, E. A., Erlingsson, S., & Bessason, B. (2018). Tool for analysis of multichannel analysis of surface waves (MASW) field data and evaluation of shear wave velocity profiles of soils. *Canadian Geotechnical Journal*, *55*(2), 217-233.

[27] OYO, C. (2016). *Operation Manual MODEL-1109 McSEIS-SW*. OYO corporation.

[28] Park, C. B., Miller, R. D., & Xia, J. (1998). Imaging dispersion curves of surface waves on multi-channel record. In *SEG technical program expanded abstracts 1998* (pp. 1377-1380). Society of Exploration Geophysicists.

[29] Park, C. B., Miller, R. D., & Xia, J. (1999). Multichannel analysis of surface waves. *Geophysics*, *64*(3), 800-808.

[30] Park, C. B., Miller, R. D., Xia, J., & Ivanov, J. (2007). Multichannel analysis of surface

doi:10.6342/NTU202403310

waves (MASW)—active and passive methods. *The Leading Edge*, *26*(1), 60-64.

[31] Pelekis, P., & Athanasopoulos, G. (2012). Application of a simplified inversion technique to published surface wave dispersion data–comparisons with advanced methods of inversion. In *GeoCongress 2012: State of the Art and Practice in Geotechnical Engineering* (pp. 2716-2725).

[32] Richart, F. E., Hall, J. R., & Woods, R. D. (1970). *Vibrations of soils and foundations* Prentice-Hall.

[33] Rix, G. J. (1995). *Accuracy and resolutions of surface wave inversion*.

[34] Tang, H. T., Graves, H. L., & Yeh, Y. S. (1990). *Large-Scale Seismic Test Program at Hualien, Taiwan*.

[35] Tang, H. T., Stepp, J. C., Cheng, Y. H., Yeh, Y. S., Nishi, K., Morishita, H., Shirasaka, Y., Gantenbein, F., Touret, J. P., & Sollogou, P. (1991). The Hualien large-scale seismic test for soil-structure interaction research.

[36] Thomson, W. T. (1950). Transmission of elastic waves through a stratified solid medium. *Journal of applied Physics*, *21*(2), 89-93.

[37] Wang, J.-S., Hwang, J.-H., Lu, C.-C., & Deng, Y.-C. (2022). Measurement uncertainty of shear wave velocity: A case study of thirteen alluvium test sites in Taipei Basin. *Soil Dynamics and Earthquake Engineering*, *155*, 107195.

[38] Xia, J., Miller, R. D., Park, C. B., Hunter, J. A., Harris, J. B., & Ivanov, J. (2002). Comparing shear-wave velocity profiles inverted from multichannel surface wave with borehole measurements. *Soil Dynamics and Earthquake Engineering*, *22*(3), 181-190.

doi:10.6342/NTU202403310

Appendix

The 2D shear wave velocity profiles displayed in the appendix are generated by the software SeisImager/SW, and the deviation is also given by it. The manual does not explain the iterative inversion process for developing the 2D profiles. Still, anyway, the process is terminated if the $MAPD$ is lower than 5% or the deviation cannot be decreased. Calculating the 1D and 2D profiles are two processes operated independently; therefore, the 1D profiles shown in previous section may not necessarily match or correspond to the 2D profiles shown in this section.

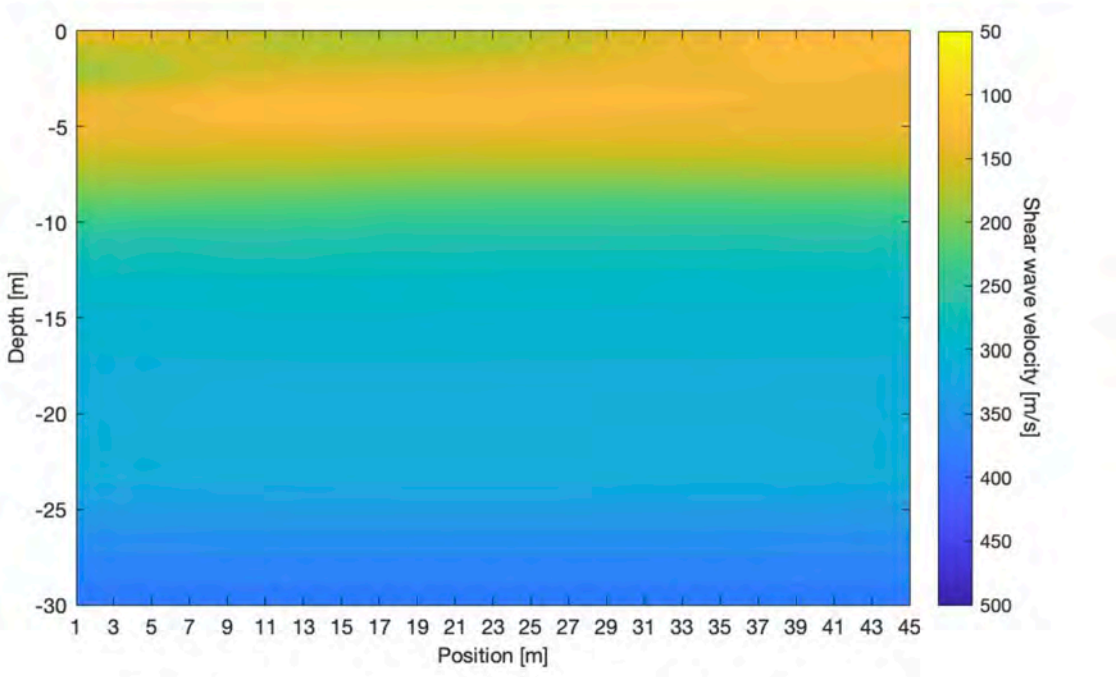

Figure A.1 2D shear wave velocity profile of TAP002. ($RMSD = 12.01$, $MAPD = 4.91\%$)

doi:10.6342/NTU202403310

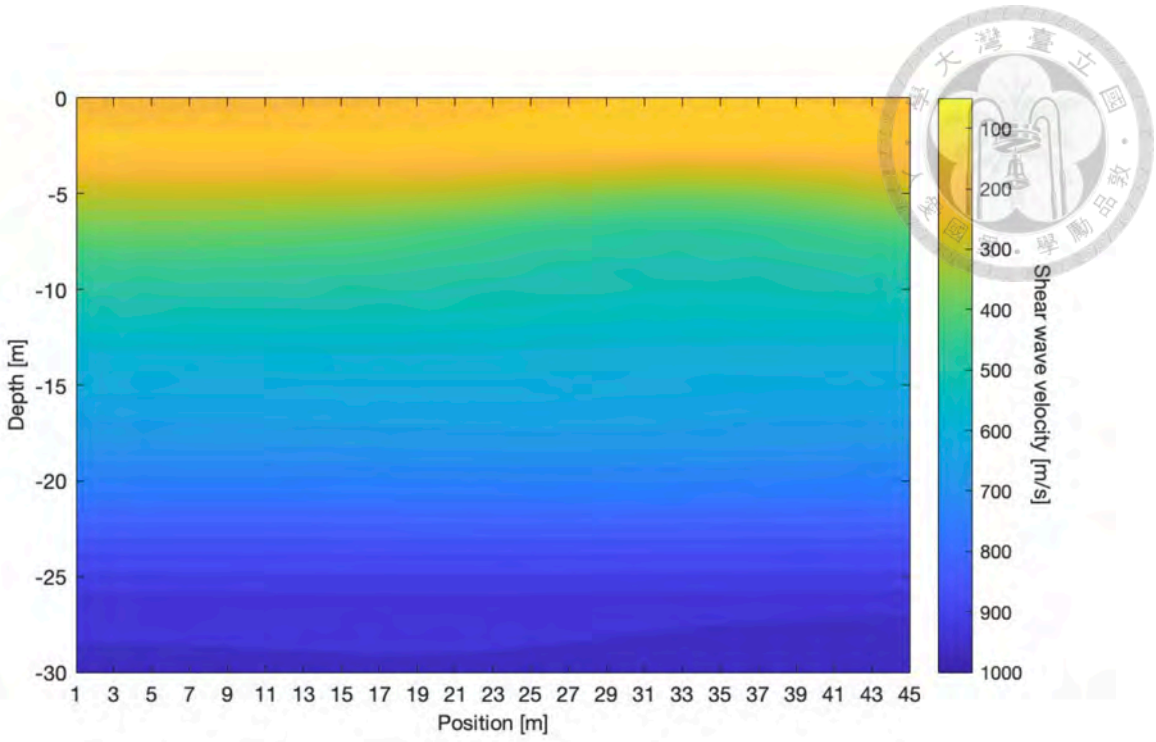

Figure A.2 2D shear wave velocity profile of TAP046. ($RMSD = 61.58,\ MAPD = 9.83\%$)

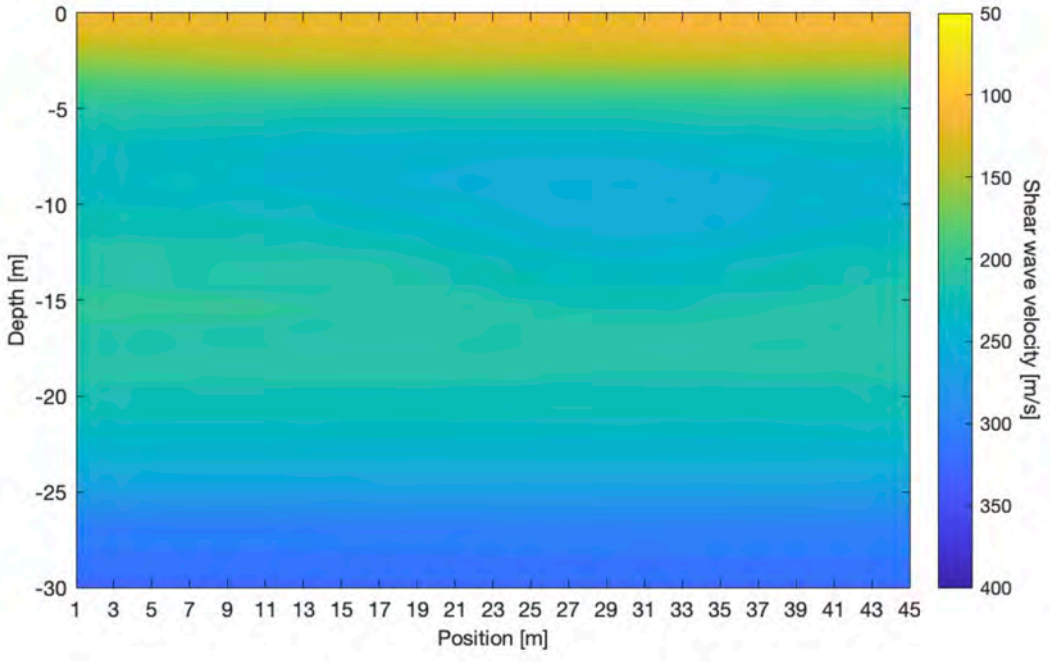

Figure A.3 2D shear wave velocity profile of TAP054. ($RMSD = 9.33,\ MAPD = 3.72\%$)

doi:10.6342/NTU202403310

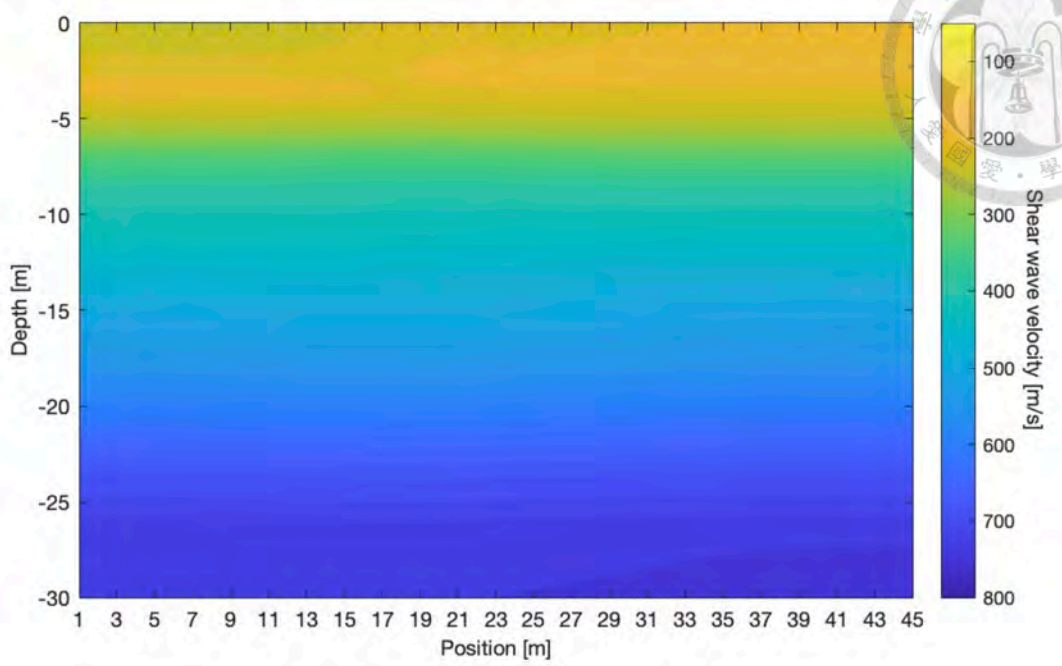

Figure A.4 2D shear wave velocity profile of TAP055. ($RMSD = 18.44,\ MAPD = 4.90\%$)

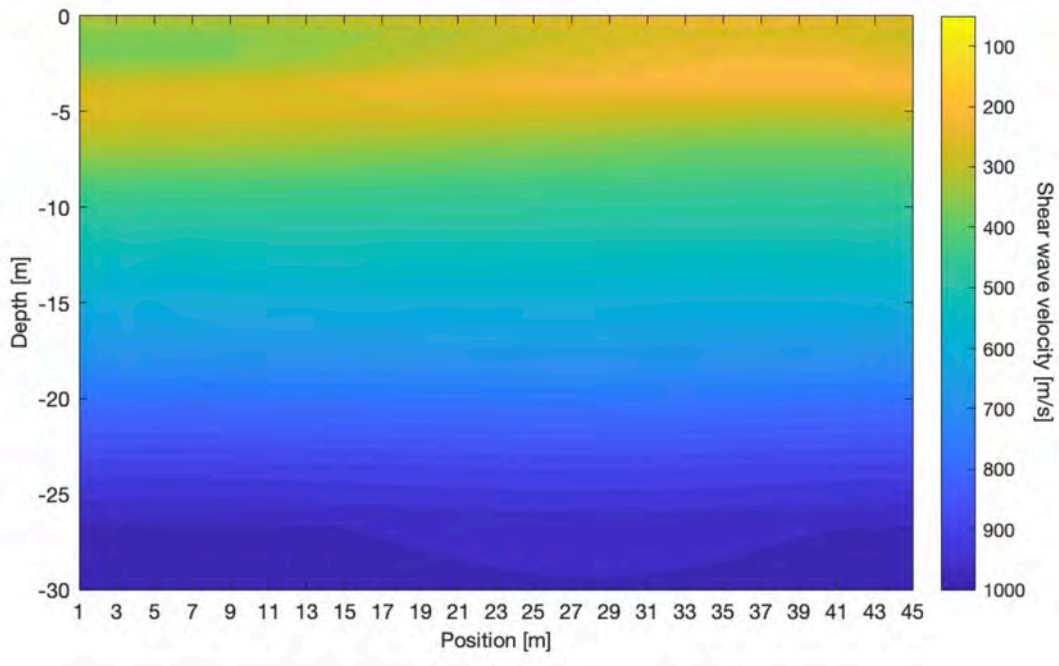

Figure A.5 2D shear wave velocity profile of TAP083. ($RMSD = 94.41,\ MAPD = 8.73\%$)

doi:10.6342/NTU202403310

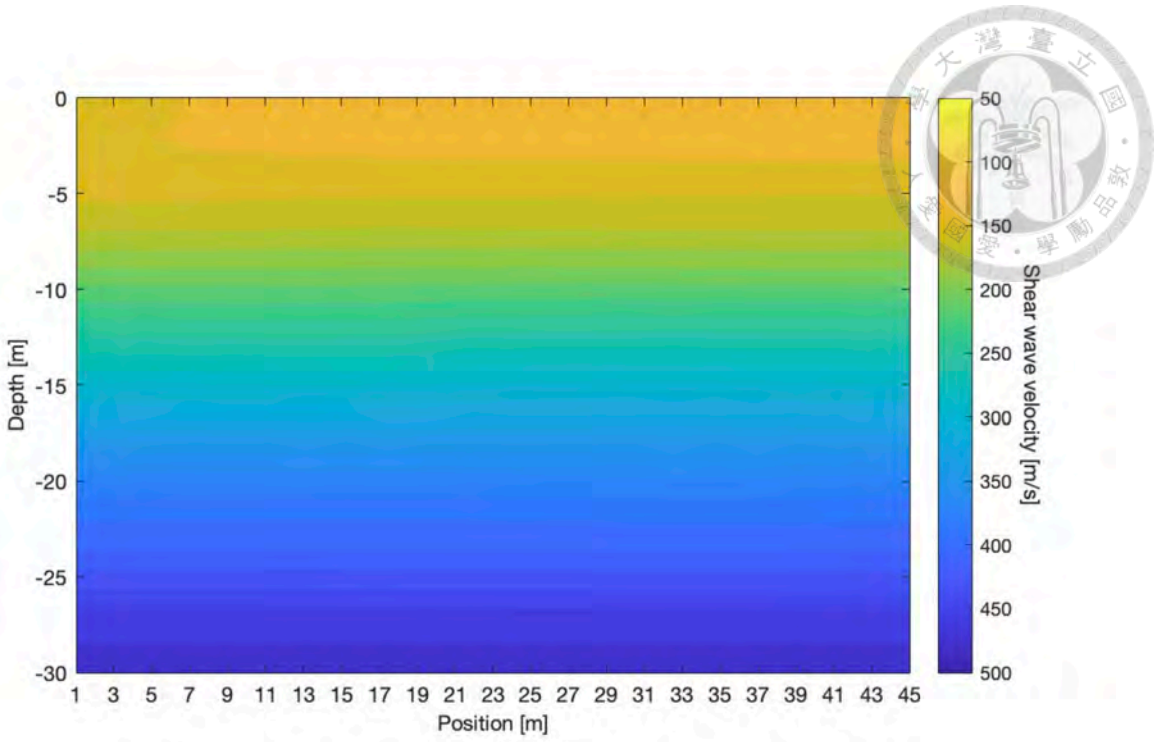

Figure A.6 2D shear wave velocity profile of TAP125. ($RMSD = 9.70,\ MAPD = 4.13\%$)

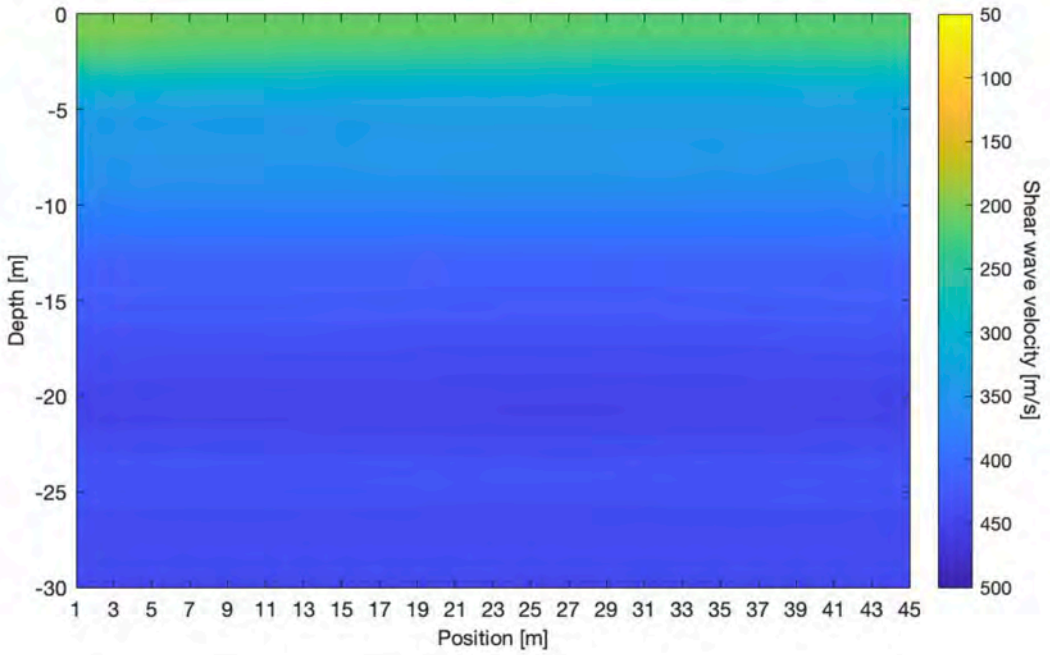

Figure A.7 2D shear wave velocity profile of TCU081. ($RMSD = 15.89,\ MAPD = 4.20\%$)

doi:10.6342/NTU202403310

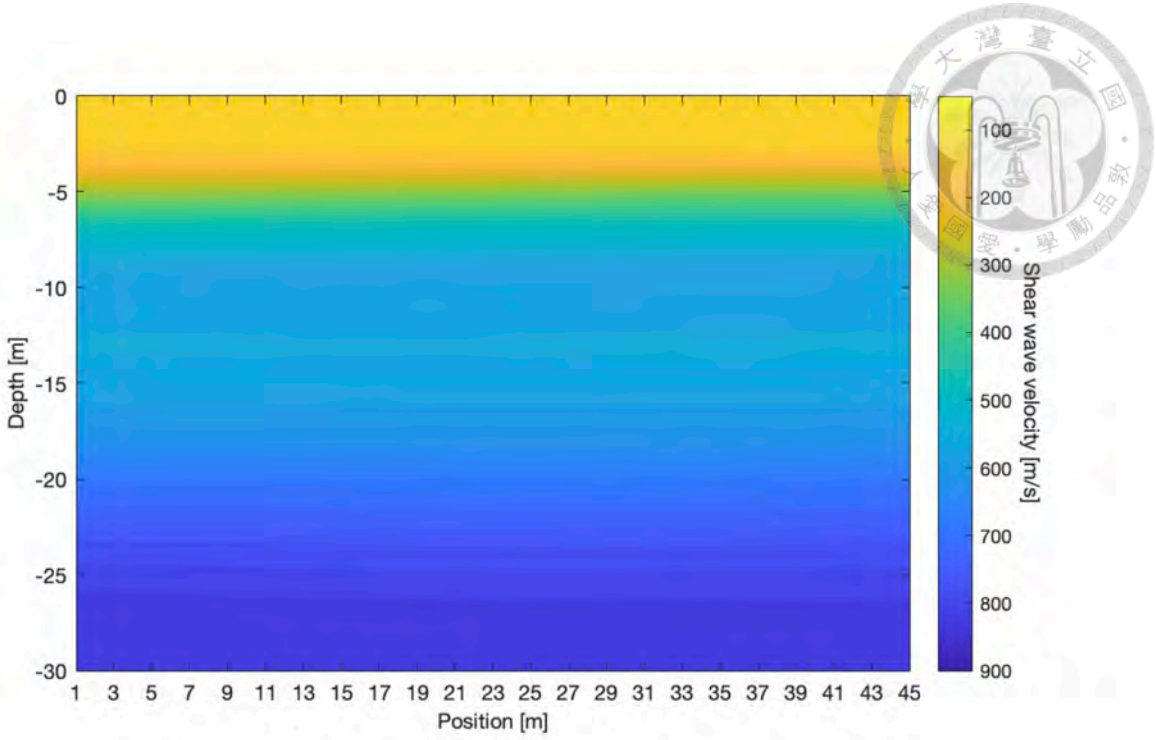

Figure A.8 2D shear wave velocity profile of TCU168. ($RMSD = 100.97$, $MAPD = 12.53\%$)

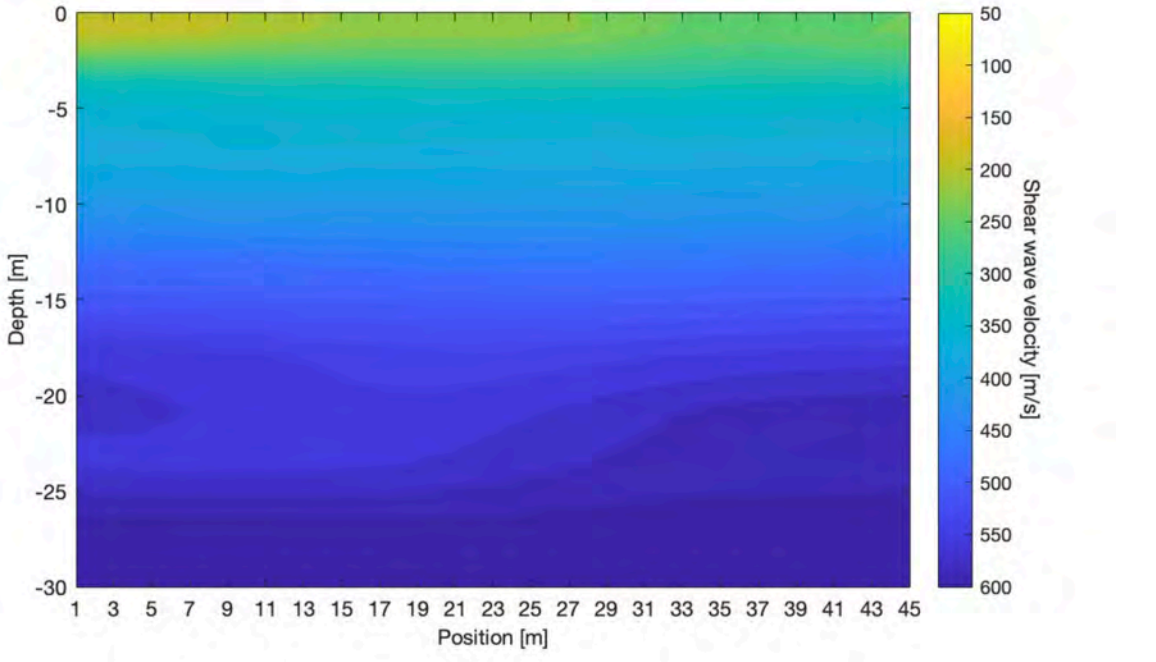

Figure A.9 2D shear wave velocity profile of ILA022. ($RMSD = 19.59$, $MAPD = 4.75\%$)

doi:10.6342/NTU202403310

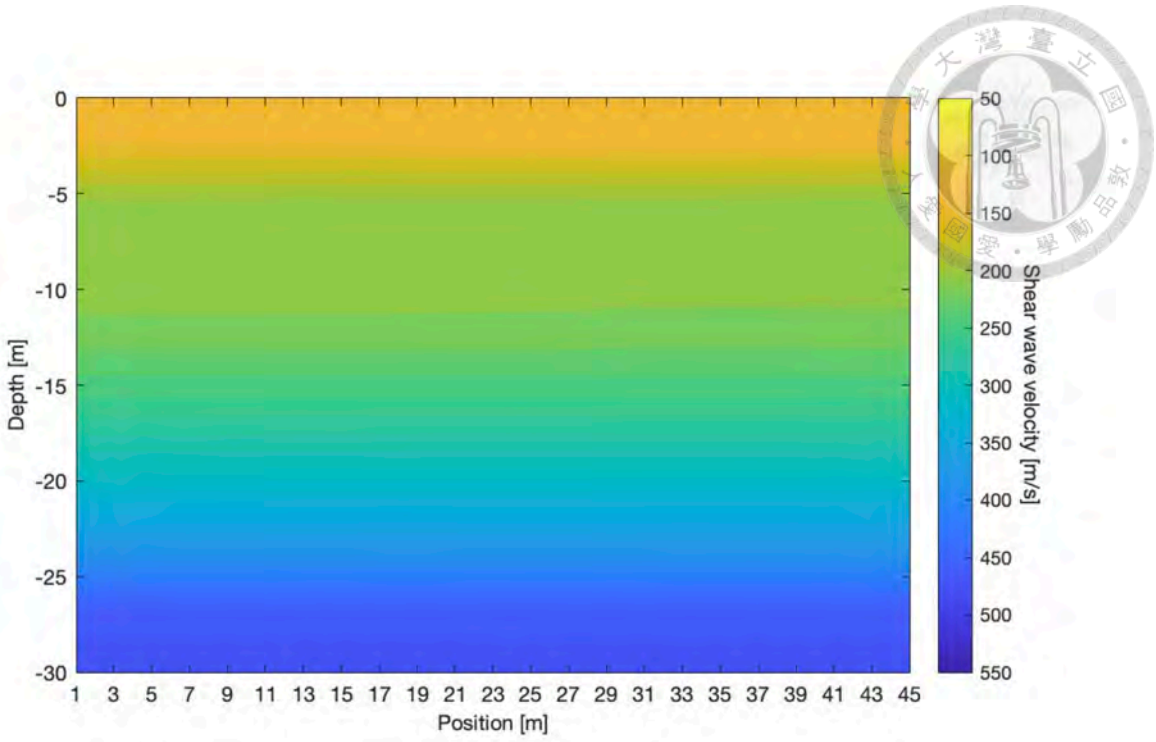

Figure A.10 2D shear wave velocity profile of ILA033. ($RMSD = 9.44,\ MAPD = 4.31\%$)

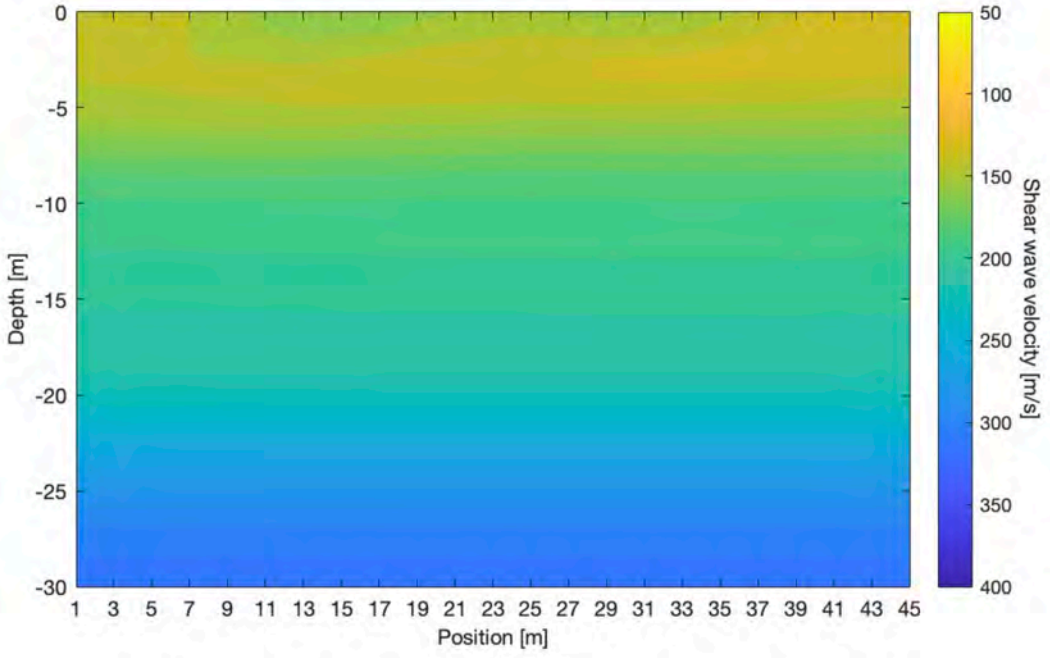

Figure A.11 2D shear wave velocity profile of ILA037. ($RMSD = 7.28,\ MAPD = 3.48\%$)

doi:10.6342/NTU202403310

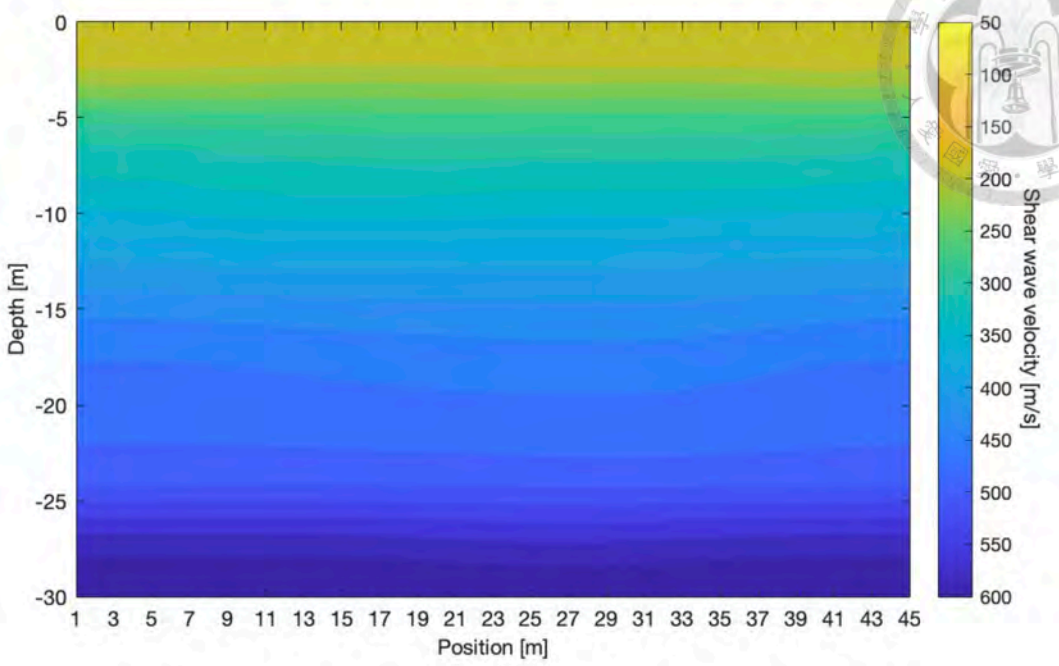

Figure A.12 2D shear wave velocity profile of ILA060. ($RMSD = 16.23,\ MAPD = 3.98\%$)

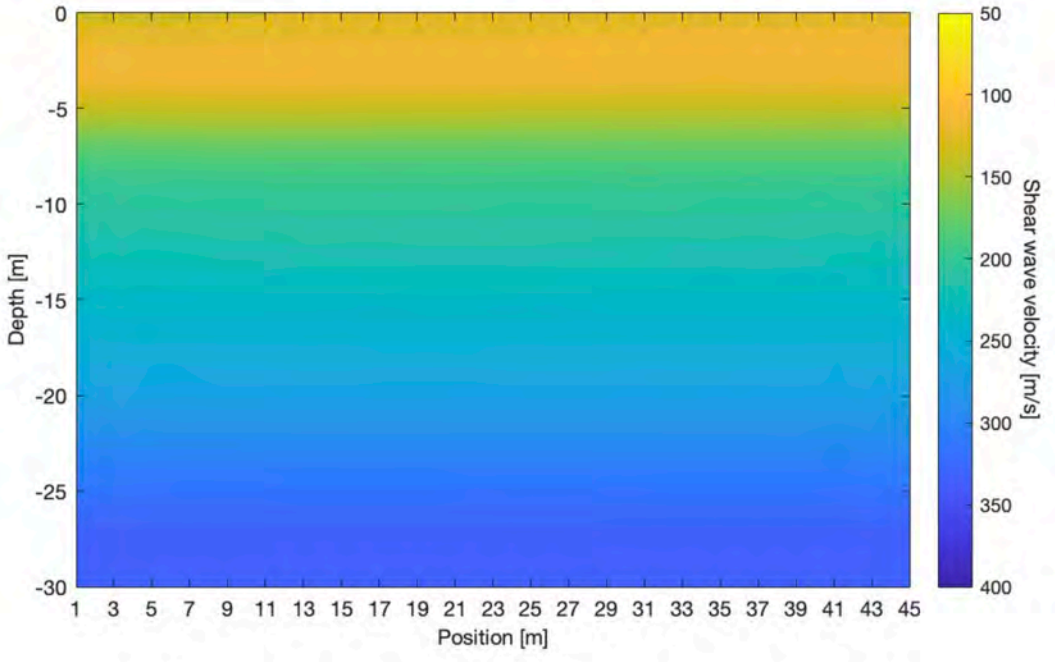

Figure A.13 2D shear wave velocity profile of ILA072. ($RMSD = 6.31,\ MAPD = 3.47\%$)

doi:10.6342/NTU202403310

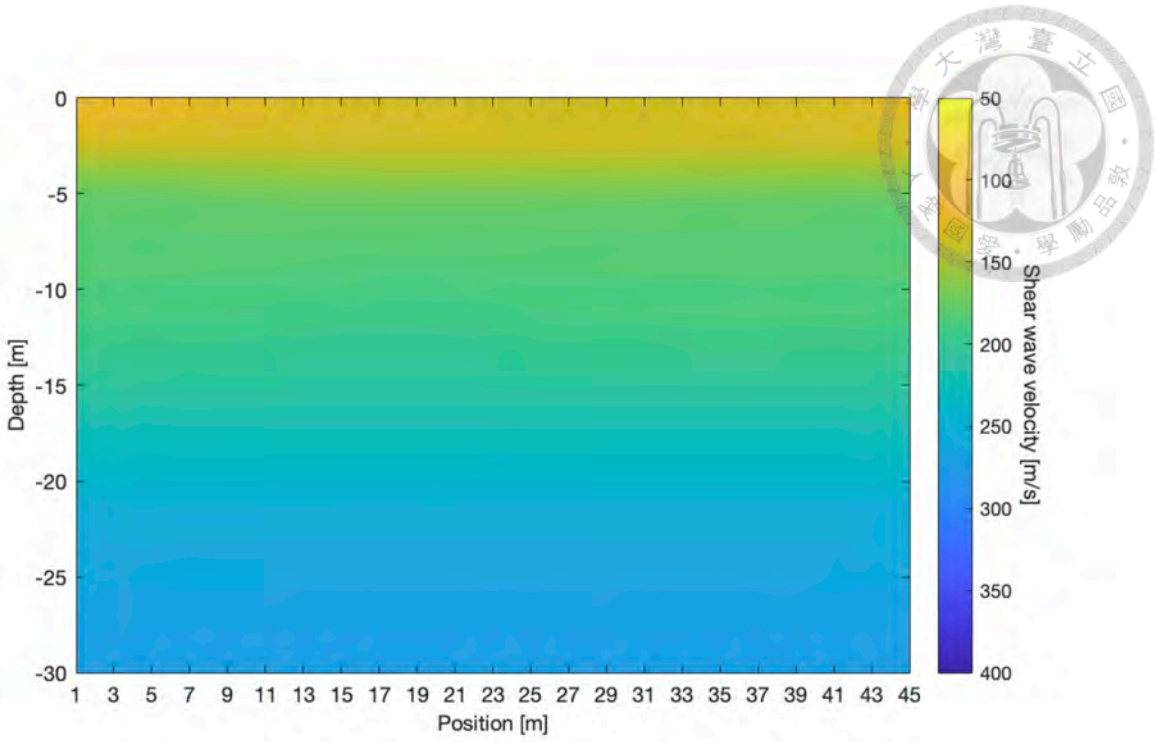

Figure A.14 2D shear wave velocity profile of KAU032. ($RMSD = 8.24,\ MAPD = 4.41\%$)

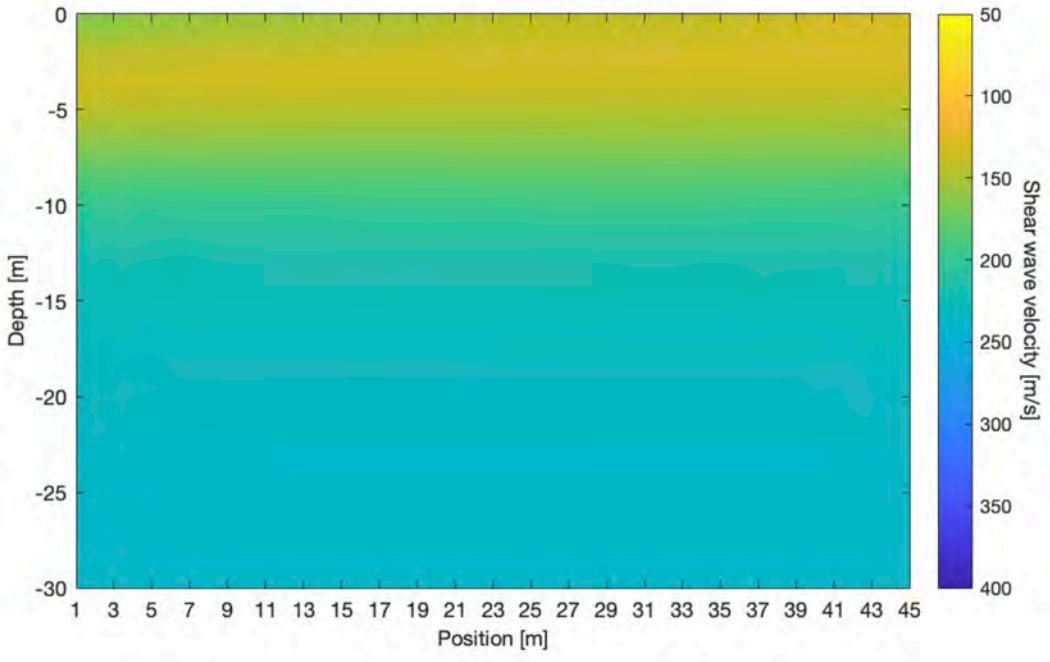

Figure A.15 2D shear wave velocity profile of KAU036. ($RMSD = 7.66,\ MAPD = 4.99\%$)

doi:10.6342/NTU202403310

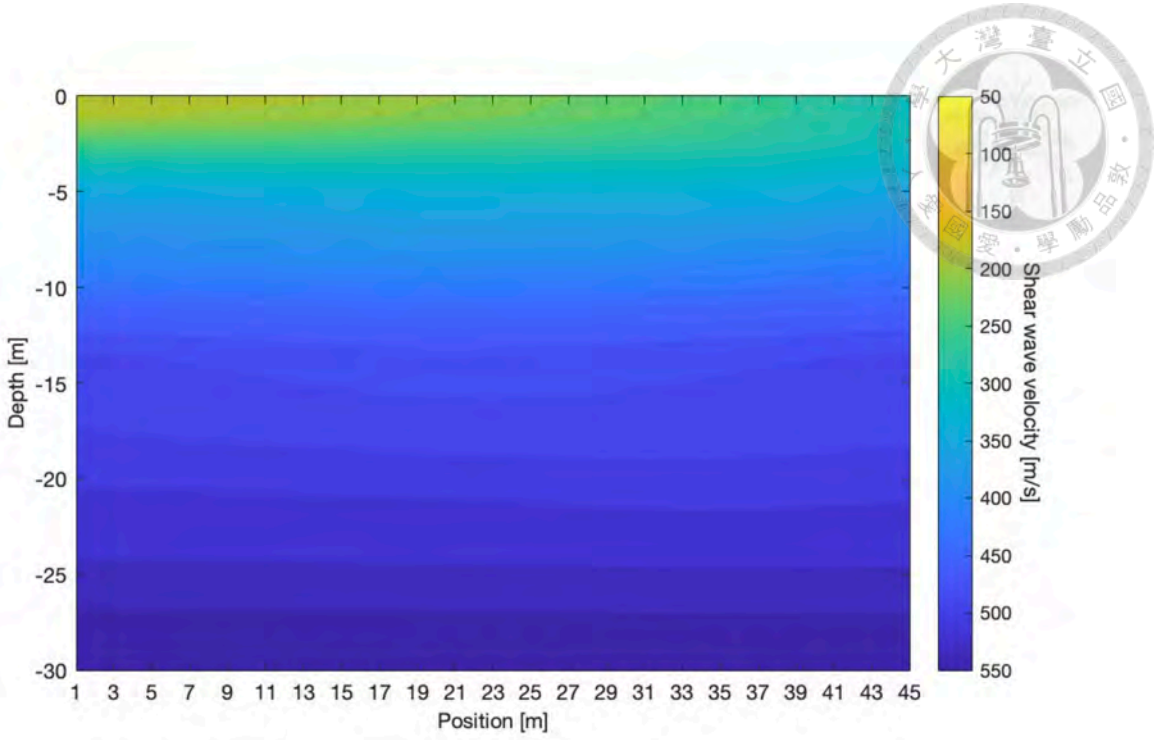

Figure A.16 2D shear wave velocity profile of KAU072. ($RMSD = 17.14,\ MAPD = 4.69\%$)

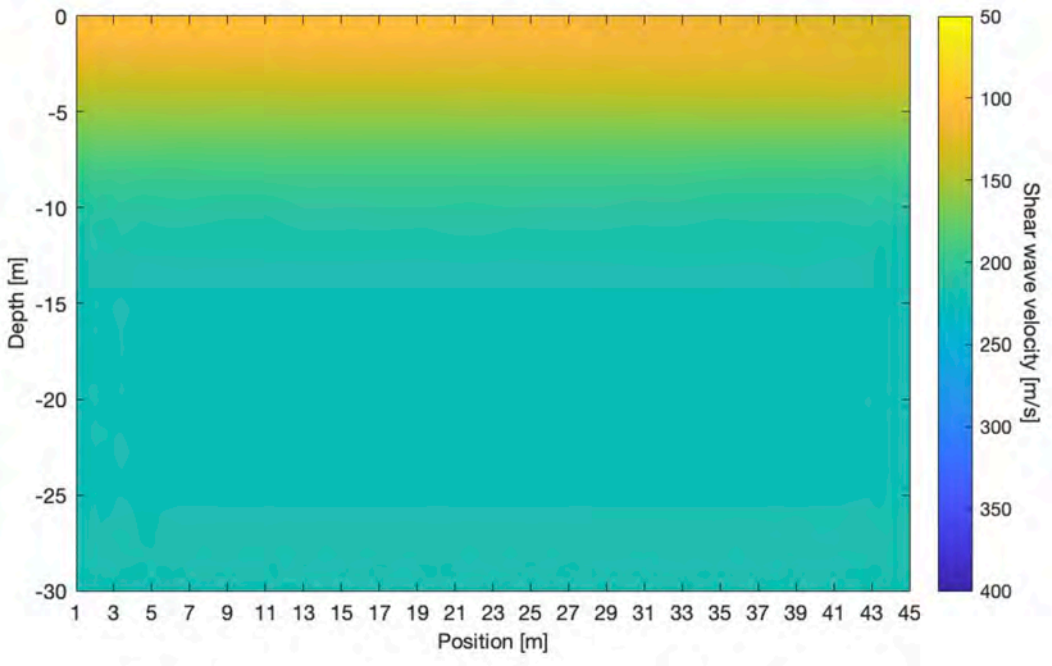

Figure A.17 2D shear wave velocity profile of KAU072. ($RMSD = 6.30,\ MAPD = 4.14\%$)

doi:10.6342/NTU202403310